The Hong Kong Polytechnic University

Department of Electronic and Information Engineering

Development and Design

of

Light-emitting-diode (LED) Lighting

Power Supplies

Xiaohui QU

A thesis submitted in partial fulfillment of the requirements for

the degree of Doctor of Philosophy

November 2009

CERTIFICATE OF ORIGINALITY

I hereby declare that this thesis is my own work and that, to the best of my knowledge and belief, it reproduces no material previously published or written, nor material that has been accepted for the award of any other degree or diploma, except where due acknowledgement has been made in the text.

_____ (Signed)

Xiaohui QU (Name of Student)

To my family

Abstract

Light-emitting-diode (LED) light sources, which are more compact, capable to change color in real time, less dissipative and more durable, are finding more applications than conventional light bulbs in domestic, commercial and industrial environments. However, LEDs have nonlinear optical, thermal and electrical characteristics, which are major hurdles for widespread lighting applications. Specifically, stabilizing colors of LED lights is a challenging task, which includes color light intensity control using switching mode power converters, color point maintenance against LED junction temperature change, and limiting LED device temperature to prolong LED lifetime. Also, requirements such as high power factor, long lifetime, accurate current control and high efficiency pose challenges to the design of LED ballast circuits.

This thesis is devoted to the study and design of effective LED lighting systems to overcome the inherent deficiencies and provide solutions for modern lighting applications. The main contributions of this thesis are summarized as follows:

1. To stabilize the colors of LED lights, we present an LED junction temperature measurement technique for a pulse-width-modulation (PWM) diode forward current controlled red, green and blue (RGB) LED lighting system. The technique has been automated and can stabilize the color effectively without the need for using expensive feedback systems involving light sensors. Performance in terms of chromaticity and luminance stability for a

temperature compensated RGB LED system will be presented.

2. LED light sources have a long life expectancy. The lifetime of LED luminaires are thus determined by their electronic ballasts. It is found that the lifetime of power converters is limited by the high-voltage electrolytic capacitors which normally have the shortest lifetime compared to other components in the system. A first-stage isolated power-factor-correction (PFC) pre-regulator is proposed, which allows the storage capacitor to be located in the secondary side of the isolation transformer. Low-voltage large capacitors of longer lifetime can therefore be used to extend the overall lifetime of the LED luminaires. Steady-state state-space averaging analysis is performed for designing the converter in discontinuous conduction mode (DCM). A prototype converter is built to verify performance of the proposed PFC LED pre-regulator.

3. The concept of secondary capacitors is extended to operate the same PFC pre-regulator in continuous conduction mode (CCM) for high-power applications ($>$ 300 W). The arrangement of power delivery is identified as the first non-cascading structure. Two secondary transformer windings and a post LED current driver are arranged to form a second non-cascading structure to improve efficiency. Additional buck current drivers can be connected in parallel to drive more LEDs independently. Since the energy from one output winding can directly be used to drive the LED without going through another power stage, a higher efficiency can be guaranteed.

4. In applications with power lower than 25 W, the current harmonics requirements are less stringent as stated in some international standards. A high-step-down-ratio and high-efficiency resonant assisted buck converter for LED light sources is proposed, which also has the lifetime of capacitor extended. The circuit is simple and efficient, without using isolation transformers. Analysis and experimental verification are presented.

Publications

Journal Papers

1. Xiaohui Qu, S. C. Wong, and Chi K. Tse, "Resonant assisted buck converter for offline driving of high brightness LED replacement lamps," submitted to *IEEE Transactions on Power Electronics*.

2. Xiaohui Qu, S. C. Wong, and Chi K. Tse, "Current-fed isolated PFC preregulator for multiple LED lamps with extended lifetime," submitted to *IEEE Transactions on Power Electronics*.

3. Xiaohui Qu, S. C. Wong, and Chi K. Tse, "Non-cascading structure for electronic ballast design for multiple LED lamps with independent brightness control," *IEEE Transactions on Power Electronics*, vol. 25, no. 2, pp. 331-340, Feb. 2010.

4. Xiaohui Qu, S. C. Wong, and Chi K. Tse, "Temperature measurement technique for stabilizing light output of RGB LED lamps," *IEEE Transactions on Instrumentation and Measurement*, vol. 59, no. 3, pp. 661-670, Mar. 2010.

Conference Papers

1. Xiaohui Qu, S. C. Wong, and Chi K. Tse, "Resonant assisted buck converter for offline driving of high brightness LED replacement lamps," submitted to *IEEE Energy Conversion Congress and Exposition (ECCE)*, 2010.

2. Xiaohui Qu, S. C. Wong, and Chi K. Tse, "Ballast for independent brightness control of multiple LED lamps," in *Proceedings of IEEE Energy Conversion Congress and Exposition (ECCE)*, pp. 2821-2826, Sep. 2009, San Jose, USA.

3. Xiaohui Qu, S. C. Wong, and Chi K. Tse, "Electronic ballast for multiple LED lamps with independent brightness control," in *Proceedings of IEEE International Symposium on Circuits and Systems (ISCAS)*, pp. 2878-2881, May 2009, Taipei, Taiwan.

4. Xiaohui Qu, S. C. Wong, and Chi K. Tse, "Isolated PFC pre-regulator for LED lamps," in *Proceedings of IEEE Industrial Electronics Society (IECON)*, pp. 1980-1987, Nov. 2008, Orlando, USA.

5. Xiaohui Qu, S. C. Wong, and Chi K. Tse, "Color control system for RGB LED light sources using junction temperature measurement," in *Proceedings of IEEE Industrial Electronics Society Conference (IECON)*, pp. 1363-1368, Nov. 2007, Taipei, Taiwan.

Acknowledgements

It is my pleasure and honor to have pursued my Ph.D. degree program at the Hong Kong Polytechnic University. Time flies fast and it now comes to the end of my Ph.D. period. In the past three years, it has been full of challenges, happiness and achievements in both my study and life. This has been a special, valuable and memorable experience for me.

First of all, I would like to thank Dr. Siu-Chung Wong and Prof. Michael Tse, my supervisors, for their patient guidance, valuable advices and sustained encouragement throughout the course of my candidature. Without their endless support, I can not finish my Ph.D. study and submit the thesis successfully. Their profound knowledge and immense enthusiasm on research impress me deeply. It is wonderful to work with them and discussion with them always benefits me.

I would also like to thank Dr. Martin Chow, Dr. Y. M. Lai, Dr. S. C. Tan, Prof. X. Ruan, Dr. Q. Chen, Dr. Herbert Iu for their kind suggestions on my research. At the same time, I wish to thank all the colleagues in the Applied Nonlinear Circuits and Systems Research Group and the friends I met in Hong Kong. They include Xi Chen, Zhen Li, Yuehui Huang, Sufen Chen, Ming Li, Jie Zhang, Ruoxi Xiang, Junfeng Sun, Xiumin Li, Xiujuan Zheng, Ada Zheng, Grace Chu, Alan Lun, Song Xiong, Guorong Zhu, Xiaofan Liu, Qingfeng Zhou, Ben Cheng, Martin Cheung, Kam-cheung Tam and Anson Lo. The time with you will never be forgotten.

I gratefully acknowledge my host supervisor Prof. Fred. C. Lee for his guidance during my study at the Virginia Polytechnic and State University. I would like to thank Prof. D. Boroyevich and Dr. S. Wang for significant discussions. Thanks also go to the members at the Center for Power Electronics Systems for their help and friendship.

I sincerely thank The Hong Kong Polytechnic University for the financial support of my study.

Last, but far from the least, special thanks go to my parents, my sister, and my cute nephew, Ming Xin. I am deeply grateful for their persistent love and constant care over the years.

Thank you!

Contents

List of Figures

List of Tables

Abbreviations

ACM average-current-mode

AM amplitude modulation

CCM continuous conduction mode

CCT correlated color temperature

CIE international commission on illumination

CRI color rendering index

DCM discontinuous conduction mode

DOE department of energy

DSP digital signal processor

HID high intensity discharge

IEC international electrotechnical commission

LCD liquid-crystal-display

LED light-emitting-diode

OIDA optoelectronics industry development association

PF power factor

PFC power-factor-correction

PWM pulse-width modulation

RGB red, green and blue

SPD spectral power distribution

SSL solid state lightings

ZVS zero-voltage-switching

Nomenclature List

Unless otherwise specified, some commonly-used symbols in the thesis are defined as follows.

Symbol	Description
v_{in}, V_m	Input line voltage, peak of the input line voltage
i_{in}, V_m	Input line current, peak of the input line current
f_s, T_s	Switching frequency, switching period
f_l, T_l	Input line frequency, switching period
V_O	Output DC voltage
I_O	Output DC current
v_{rec}	Rectified line voltage
d, d_{of}	Duty cycle of turn-on, duty cycle of turn-off
L	Inductance
C	Capacitance
i_L, I_L	Inductance current, peak of the inductance current
i_{ref}, I_{ref}	Reference current, peak of the reference current
i_C	Capacitor current
i_D	Diode current
R	Resistive load
R_S	Sensing resistor
P_{in}, P_o	Input power, output power

Chapter 1

Introduction

1.1 Motivation

The first electrical light source, the incandescent bulb, was invented by Swan and Edison in 1879 [5–7]. The hot source filament is heated up to a high temperature to emit light up to the human visible light spectrum. Approximately 90 % of the power consumed by an incandescent bulb is emitted as heat, rather than visible light.

Gas discharge lamps date back to the beginning of the 20th Century [8,9]. In 1938, General Electric (GE) Company in Great Britain introduced low-pressure mercury discharge lamps for commercial applications. The inside of the tube is coated with a phosphor powder. Such lamps are called fluorescent lamps [10–12]. Mercury atoms and ions are excited through acceleration of electrons to emit UV radiation which is converted to visible light using phosphor. Thus, the overall luminous efficacy of gas discharge lamps is the product of radiation efficiency and conversion efficiency. There is approximately 23 % of power converted to visible light. Later, different types of gas discharge lamps, such as low-pressure sodium

lamps, high-pressure discharge lamps [13, 14], high-intensity discharge (HID) lamps [15], appeared with higher luminous efficiency. However, there has been little efficacy improvement for the last ten years and very limited improvement is expected for the future.

An alternative light source, semiconductor solid state light-emitting-diode (LED) [16, 17], employs the effect of injection electroluminescence, which is a process of generation of light utilizing a direct conversion of electrical energy to potential energy of electrons. An LED is a direct band-gap semiconductor p-n junction diode. When electric current flows through the junction, holes and electrons are injected into the depletion region and go into the respective neutral region. These diffused excess electrons and holes acquire potential energy equal to the band gap energy and may recombine causing light emission. LEDs [18–21] use charge injection to replace the energy-dissipative acceleration of charge carriers in the light generation process, having theoretical radiative efficiency of up to 100 %. Compared with other light sources, LEDs have luminous efficacy grown exponentially as shown in Fig. 1.1.

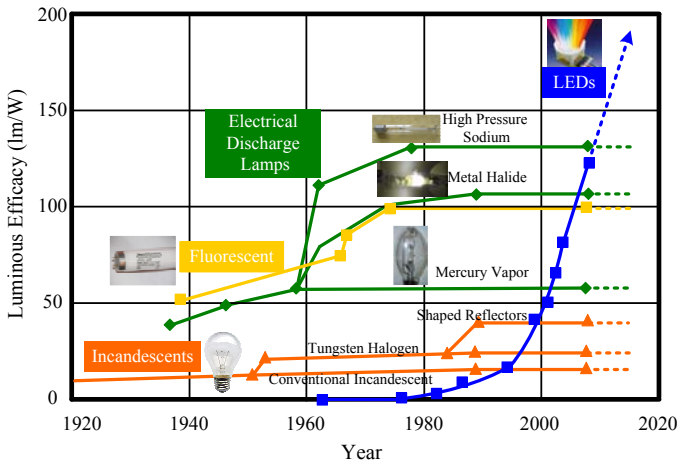

Figure 1.1: Comparison of luminous efficacy among different types of lighting devices.

In 2008, lighting accounts for 22 % of the total electricity energy used in the U.S. as reported by the Department of Energy (DOE) of the U.S. [22], as

depicted in Fig. 1.2, and the demands for energy are increasing. To promote more energy saving, there is a popular and prospective trend to employ more energy efficient lighting alternatives and to gradually reduce energy inefficiecnt incandescent bulbs. Some governments have introduced measures to phase out incandescent lamps [23]. Brazil and Venezuela started to phase them out in 2005 [24], and other nations are scheduling phase-outs of incandescent lamps: Australia, Ireland and Switzerland [25] in 2009, Argentina [26], Italy, Russia and the United Kingdom [27] by 2011, Canada in 2012 [28], and the U.S. between 2012 and 2014. The Optoelectronics Industry Development Association (OIDA) have forecast that solid stage lighting will exceed 25 % by 2015. During this period, fluorescent lighting will tend to saturate at about 40 % of all lighting revenues, while incandescent lighting will decline to 30 % share in 2015 as shown in Fig. 1.3 [29].

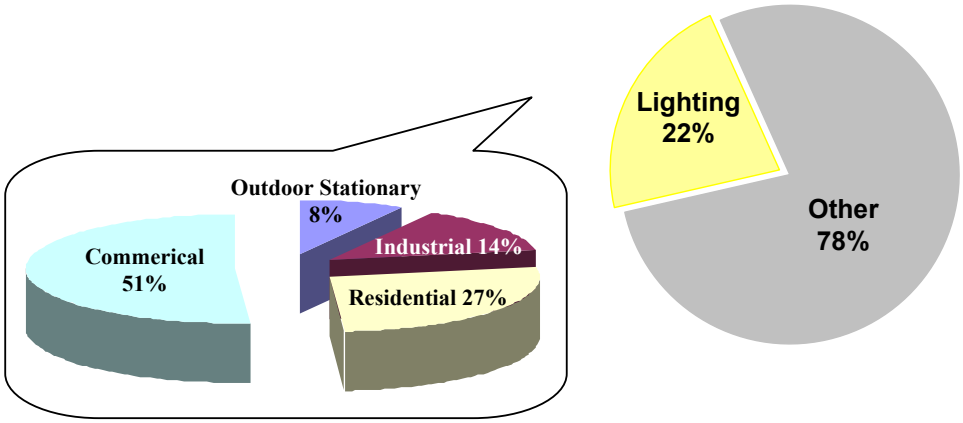

Figure 1.2: Distribution of electricity energy utilization in the U.S. in 2008

With the rigid growth of technology in semiconductors [30–34], it is believed that LEDs will become a major lighting device in the coming years [35–39]. Fig. 1.4 and Fig. 1.5 exhibit a variety of LED lamps and fixtures from different dominant manufacturers, such as Cree, Lumileds, Nichia, Osram, Lamina, Soeul semi, etc. Table 1.1 gives typical LED lamps' characteristics from these manufactures recently, where the lumen per watt is catching up with florescent lamps. Improvement in the light output of high flux LEDs are rapidly giving rise to many new applications and products, particularly in the general illumina-

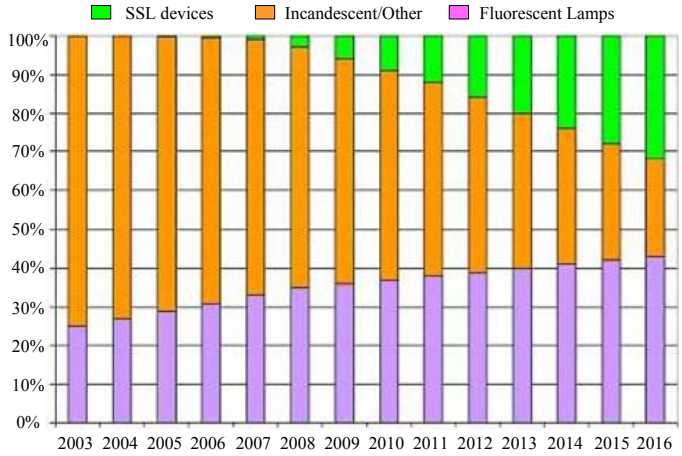

Figure 1.3: Global market share 10 year forecast for lighting

tion area [40]. Besides, LED luminaires offer several desirable advantages over the traditional lamps including compactness, lacking of UV and IR radiation, longevity, mechanical ruggedness, fast response, reliability, mercury free, wide color range, ease of control and instant color changing capacity. Consequently, LEDs have great potential in numerous applications from traffic signal, signaling, liquid-crystal-display (LCD) back lighting [41–43], detector system [44], biomedical apparatus [45], general decorative illumination, etc. Therefore, more and more investigations have focused on the new opportunities in lighting design, control of the intensity and the color itself, and spatial distribution of light, along with practical implementation of LED luminaires.

Figure 1.4: Various LED lamps from different manufacturers.

Despite considerable advantages, LEDs have inherent nonlinear character-

Figure 1.5: Examples of commercial luminaires

Table 1.1: Typical LED lamp characteristic from some manufacturers.

White LED		Viewing Angle Degrees	Typical Lumens (lm) 350 mA	500 mA	700 mA	1 A	1.4 A	1.5 A	2.8 A	5 A	Typical Current mA	Typical Voltage V_f (V)	Typical Power W	Therm. Resist. °C/W	Max. Junct. °C	CRI
Osram	LW W5SM Cool	120	52-97		104.3						350	3.2	1.1	6.5	125	80
Lumileds	LXLW-PWC1-0100 Cool	120	100								350	3	1.1	10	150	70
	LXML-PWC1-0100 Cool	140	100			180					350	3.15	1.1	10	150	70
	LXK2-PWC4-0220 Cool	120	105			185	220		300		1000	3.65	3.7	5.5	150	70
	LXK2-PWW4-0180 Warm	120	85			150	180		250		1000	3.65	3.7	5.5	150	75
Cree	XR E Series Cool	90	107								350	3.3	1.2	8	150	75
	XR E Series Warm	90	80.6								350	3.3	1.2	8	150	80
	MC E Series Cool	110	107.5								350	3.2	1.1	3	150	75
	MC E Series Warm	110	80								350	3.2	1.1	3	150	80
	XP E Series Cool	115	114								350	3.2	1.1	9	150	75
	XP E Series Warm	115	87.4								350	3.2	1.1	9	150	80
Nichia	NS9W153MT Cool	120	350								350	10.5	3.7	10	150	
	NS3W183T Cool	120	120								350	3.5	1.2	15	135	
	NS3L183T-H3 Warm	120	95								350	3.5	1.2	15	135	85
	NS6W083BT Cool	120	100								300	3.3	1.0	10	120	
Seoul Semi	W42180 Cool	127	100								350	3.25	1.1	7.2	145	75

istics varying with time, current, temperature and from device to device. As a consequence, there are still some remaining issues involving optical, thermal, electrical, and temporal behaviors to be solved in LEDs applications, before they can be a dominant force in general illumination applications [46, 47].

First of all, the accurate adjustment of desired color chromaticity and brightness as well as good maintenance of the selected chromaticity and brightness during operation is required in both display backlighting and general lighting. In general, the desired color is a mixture of three primary colors, each with fixed chromaticity, but with adjustable brightness. So red, green and blue (RGB) LEDs can be used to mix color by calculating their respective required intensities and then adjusting corresponding driving currents [48–51]. However, the output intensity of LEDs is not an absolute and linear function of the driving current.

Chromaticity of three color LEDs will shift at different currents [52]. Therefore, the required brightness is not easy to calculate and fixed chromaticity may not persist. To make things worse, the supplied electric power will heat up the LEDs that results in junction temperature rise of several tens of degree Celsius, depending on the thermal resistance of the device and its enclosure. The junction temperature rise will lead to RGB primary chromaticity further shifting and their emission intensity decreasing. The nonlinear relationships of light output intensity and RGB chromaticity varying with driving current and junction temperature make it complex to control the system because the impact is hard to be quantified. Also, the severe problem of overheating may destroy the LEDs, or reduce their lifetime [53, 54]. White light from RGB LEDs is not ideal for general lighting which requires a spectrum of light that resembles the black body radiation for better color rendering. An alternative simpler and cheaper method of generating white light is to use a monochrome emitter such as a blue LED with phosphor conversion.

LEDs need drivers to regulate the driving current [55]. Although it does not demand high voltage for ignition like fluorescent [56–58] and other electrical discharge lamps [59–63], in terms of device variation, driving a single or multiple LED lamps from an offline power source to relatively low-voltage LED loads, where the typical forward voltages of red, green, blue and white LEDs are 2.4 V, 3.55 V, 3.75 V, and 3.75 V, poses challenges to the spower converter design with desired performance, such as high power factor, low input current harmonics, high electrical efficiency, accurate driving current, fast dynamic response, as well as sufficient lifetime matching with that of LEDs in order to compete with existing light sources. The highly temperature sensitive LED necessitates thermal management and precision control methods for color maintenance.

Motivated by these challenges of using LEDs in practical implementations, this project will investigate the characteristics and the decoupling of the influence among electrical, thermal, and optical domains, with the ultimate aim to design

an effective LED lighting system suitable for modern applications.

1.2 Literature Review

The first commercially usable LEDs were developed in the 1960's. In fact, due to their low luminous intensity and relative high cost, LEDs have been used for low-brightness applications for decades. It is only recently that the widespread application of LEDs becomes possible after the introduction of high-flux LEDs. With the advancement of technology of new materials and manufacturing processes, the high-flux LEDs are attracting more and more attention from both academia and industry. In this section, a literature review will be given based on the research in the recent decade. Two categories will be divided according to color control methods and power converters for LEDs.

1.2.1 LED Color Control and Dimming Methods

The concept of color can be divided into two parts: chromaticity and brightness (or luminance). In the RGB mixed-color system, all color can be acquired by adjusting the different brightness of RGB LEDs, each of which should have fixed chromaticity. Dimming methods are important to generate various colors with corresponding brightness. Generally speaking, there are two approaches for dimming an LED.

One can be accomplished by modulating the amplitude of the DC biasing current for LED driving. This amplitude modulation (AM) can be easily implemented by linear power supplies or the current feedback control loop in a power converter. Sauerländer *et al.* [64] observed and showed that diving an LED with AM current has a better performance in luminous efficacy than other modulation methods including pulse width modulation (PWM). However, AM is not suitable

for applications where an accurate control of color chromaticity and brightness is needed, e.g., for LCD displays, because the output lumen is not linearly proportional to the driving current. Moreover, Muller-Mach *et al.* [65] showed that the spectrum of InGaN-based blue LEDs shifts toward shorter wavelengths with increasing the driving current. Similarly, the other color LEDs also have this phenomenon. Dyble *et al.* [52] did experiments to systematically quantify the chromaticity shifts based on white LEDs when dimming using AM and PWM. It was reported that the RGB mixed-color white LED system showed very large chromaticity shifts, resulting from changes in spectral power distribution (SPD) including amplitude, peak wavelength, and the shape of the spectrum. It is readily understood that even small amplitude and peak wavelength position changes of certain color LEDs can cause perceivable color changes [66, 67].

The PWM method is another dimming scheme. During the turn-on duration, the current is constant and it assures a constant color chromaticity in the International Commission on Illumination (CIE) gamut, without consideration of temperature effects caused by heat during operation. PWM has the ability to achieve lower current ranges and the linear control of light intensities compared to AM. Usually, a modulation frequency higher than 100 Hz is used to prevent the perception of individual light pulses, causing a flickering effect. Dyble *et al.* [52] also observed the chromaticity shift using PWM experimentally. But the chromaticity shift is not caused by the driving current but the junction temperature of the LED. Nakamura *et al.* [68], Kish and Fletcher [69], and Tamura *et al.* [70] had found that heat at junction of the LED would cause the spectrum to change amplitude, peak wavelength position and shape. Hong [71] investigated that RGB LEDs had different sensitivities to heat: the light output of red LEDs changes the most with heat, followed by green and blue. Therefore, for the mixed-color RGB LED system, some active feedback system controls must be incorporated to obtain the non-perceivable chromaticity shift. Currently, the chromaticity shift caused by the PWM method is easier to correct than that by AM method. Thus, PWM is commonly used for LED dimming [72–75].

Although the nonlinearity of the forward driving current to the LED color output can be reduced using PWM control of the fixed forward current drive, the nonlinearity of the junction temperature to the LED output is still a remaining hurdle for precise dimming. Thus, much research goes to search methods for acquiring the junction temperature of LEDs so as to utilize a junction temperature-dependent luminous flux characteristic normally provided by manufacturer's datasheet for the further control. Gu and Narendran *et al.* [76, 77] proposed a non-contact method for determining the junction temperature of phosphor-converted white LEDs. But the methodology uses a wavelength shift to determine the junction temperature and it is not easy to apply in consumer products. Pinho *et al.* [78] determined the junction temperature using the heatsink temperature, the thermal resistance, and the input power. But it totally depends on the thermal resistance from junction to package of LEDs given in the datasheet and this can cause measurement errors. Mineiro Sá Jr. *et al.* [79] proposed to explore the linear function between the forward voltage and the junction temperature, where the forward voltage is easily measured and then the junction temperature can be determined by a linear function. The method allows discarding the influence of the intrinsic series resistance of the LED in the mathematical model of the I-V characteristic curve avoiding measurement errors. However, no information was given on how to correct the influence of the junction temperature of LEDs especially when several LEDs share a common package and heat sink.

The feedback color control of RGB LED lamps is known to maintain the color and the brightness accurately without information of the junction temperature. Heatsink temperature feedforward, flux feedback, their combination, and chromaticity coordinates feedback have been suggested previously as color control concept by Muthu *et al.* [48] and partly validated in [49–51, 80–85]. The feedback controller can be accounted for using an or several optical sensor(s). Detailed operation steps and control schemes are given in these papers, whilst good system performance was also verified under dimming. However, as the feedback control uses a light intensity sensor whose value varies as the LED

dims down, measuring errors can be quite large when the intensity gets small. Furthermore, optical sensors are also semiconductors and need calibration over time, increasing the running cost.

Much prior work has been focused on the LEDs' color control, eliminating the complexity caused by temperature variation. Although the reported works have dealt with their respective methodologies and design procedures, they are all relatively complicated and expensive, preventing them from being widely used in the application of LEDs.

1.2.2 Power Converters for LEDs

LEDs are operated at a voltage higher than their cut-in voltages, above which their currents increase rapidly. Their powers are therefore better controlled with current modulation. Connecting LEDs to the AC power grid, a voltage step-down power converter is needed. This LED power converter must comply with industry standards. The standards consist of current quality, power factor limitation, current harmonics restriction, lifetime matching, conversion efficiency, etc.

European Union has claimed that the input current harmonics of lighting equipment must meet the requirements specified by EN 61000-3-2 Class C standard [86]. Much research has been directed toward power-factor-correction (PFC) topologies [87–91] and control schemes [92,93] in LED applications over the past decades. Ye *et al.* [94] studied and compared several single-stage offline PFC pre-regulators for driving LEDs, including boost converter, SEPIC converter [95], forward converter, flyback converter [87], and half-bridge converter [90, 91]. These topologies are suitable for different power capacities and different customer requirements. In general, these papers were devoted to improve power factor (PF) and efficiency in the pre-regulator stage. Little attention was directed to the LED current and the light control. Besides, these papers did not consider

the lifetime of the converters whilst using high-voltage (up to 450 V) low-lifetime electrolytic capacitors [96], which limited the lifetime of the converter.

Van der Broeckl *et al.* [97] removed the output capacitor from the converter and fed LEDs directly by pulsating currents. Although LEDs show an extreme fast light to current response, the color shift due to the pulsating current especially in some topologies such as flyback converter cannot be neglected. Also, the low input-voltage converter needs a front-end PFC pre-regulator, whose output charge hold-up capacitor cannot be removed easily. Qin and Hui *et al.* [98] proposed a method to decrease charge hold-up capacitance so that high-capacity electrolytic capacitors can be avoided and relative low-capacity long-lifetime polyester or ceramic capacitors can be used. The disadvantage of the method is the increase of inductance of the LC filter. The huge inductor is not acceptable. Gu *et al.* [99] also proposed a method to reduce the storage capacitor in the PFC power supply, sacrificing the performance of the input current. In this paper, a third harmonic current was injected into the input current flow under the prerequisite of ensuring the power factor and input current harmonics satisfying some current limitations. As a result, the output voltage ripple could be broadened so that the output capacitor could be reduced. A serious shortcoming is that the current ripple flowing into the LEDs is too large, reducing luminous efficacy of the LEDs.

The above work generally uses LED strings connected in series so that the output voltage can be as high as 40-50 V. This will facilitate the post-PFC DC/DC converter design with higher efficiency and wider topology selection. Nevertheless, LED characteristics can vary from device to device. Thus, one driver per LED chip would be preferable in terms of high color accuracy for sophisticated lighting applications, like LCD display and general illumination. Driving such LEDs from an offline power system to low-voltage loads will introduce many challenges in the converter design. For instance, high voltage-conversion ratio would be implemented by isolation transformer with high turns ratio, thus bringing relatively large leakage inductance which needs passive snubber circuits in

reducing either voltage or current stress [100]. In addition, snubber circuits will decrease the efficiency and increase the cost of LED drivers.

Current control can be easily realized by using a current feedback control loop in the power converter. Traditional control schemes including average-current-mode control, peak-current-mode control, hysteresis-current-mode control and so on, are available in LED applications.

As a result, a durable LED driver system with high efficiency and independent color or brightness control is still needed for modern and sophisticated applications.

1.3 Objective of the Thesis

The main objective of our work is to investigate the implementation issues of high-brightness LEDs and develop effective LED lighting systems with the motivation of improving the performance catering to different modern applications. Due to inherent nonlinear characteristics of LEDs, new methodologies and concepts will be investigated to alleviate or eliminate the negative effects in the accurate color and brightness realization. Likewise, device variation makes a combination of LEDs connected in series or parallel working as a single load driven by one LED driver not practical. On the contrary, one driver per LED increases the size and the cost of the driver system in addition to the considerations of electrical issues such as lifetime, efficiency, reliability, etc.

This thesis aims to provide design solutions for effective and simple LED driver systems via decoupling and solving the above issues. Analytical studies will be reported and experimental measurements will be provided to verify the effectiveness and performance of the proposed systems.

1.4 Outline of the Thesis

This thesis is organized as follows.

Chapter 1 introduces the recent development of high-power LEDs for solid state lighting. A literature review on the illumination technology of LEDs in the recent decade is provided. The potential improvement of LED lighting systems is discussed. The research motivation and objectives, as well as an outline of this thesis are presented.

Chapter 2 describes the fundamental aspects of high-brightness LEDs, including physical, electrical, thermal and optical characteristics and their comparison with other kinds of light sources. Some basic colorimetry principles are given to evaluate light generated uniquely by LEDs. The demands for LED applications are detailed and the construction of an effective LED system is identified as the research subject.

Chapter 3 proposes a simple and practical temperature measurement technique for color control to overcome the thermal drifts of color and brightness of LEDs. The operation principle and implementation technique are outlined. The effectiveness of the technique is experimentally verified.

Chapter 4 analyzes the challenges in the design of power converters for LED lighting applications. A new low-power isolated PFC pre-regulator is proposed. The pre-regulator allows longer-lifetime, lower-voltage charge storage capacitor to be used in the transformer secondary extending the system lifetime. Voltage and current stresses for power devices have been estimated and experimentally verified.

Chapter 5 extends the power level of the circuit described in Chapter 4. Details on the development of the non-cascading construction to achieve high running efficiency of the whole LED ballast without additional cost are given.

Chapter 6 proposes a high-step-down-ratio and high-efficiency resonant assisted buck converter for offline driving of high-brightness LED light sources. The transformerless design allows efficiency gain in non-isolated applications. The elimination of high ripple currents on the storage capacitor can extend the capacitor lifetime to match that of LEDs. The resonance makes sure that the freewheeling current partly flows across the low-voltage Schottky diode to further reduce loss. A prototype converter is built to verify performance of the proposed LED ballast.

Finally, Chapter 7 gives a conclusion to the thesis. The major work and contributions are reiterated. Some suggestions for future research are given.

Chapter 2

Basics of LEDs

In this chapter, the physics of the LED device is introduced. A detailed discussion focusing on thermal, optical and electrical characteristics of LEDs is given. The methodology of using RGB tricolor LEDs to generate color lights, along with some technical specifications for LED applications is described. Finally, the goals in constructing an illustrative LED system is identified.

2.1 Physical Principle of LEDs

LEDs are electroluminescence light sources in contrast to pyroluminescence incandescent lamps and photoluminescence fluorescent lamps. The essence to electroluminescence is the charge carrier injection across a p-n junction into a zone where the injected carriers can convert their excess energy to light. The process is the principle of light emission in diodes and detailed as follows.

The so-called p-n junction is a junction formed by combining P-type and N-type semiconductors together in very close contact. Due to different doped materials, P-type semiconductor has the majority carriers being holes and the mi-

nority carriers being electrons whilst N-type semiconductor has the contrary ones. In a p-n junction, without an external applied voltage, an equilibrium condition is reached in which a potential difference called *diffusion voltage* V_D is formed across the junction. Electrons near the p-n junction interface tend to diffuse into the P region. As electrons diffuse, they leave positively charged ions (donors) in the N region. Similarly, holes near the p-n interface begin to diffuse into the N region leaving negatively charged ions (acceptors) in the P region. The regions nearby the p-n interfaces lose their neutrality and become charged, forming the *space charge region* or *depletion region*, whereas the left P region and N region are kept neutral.

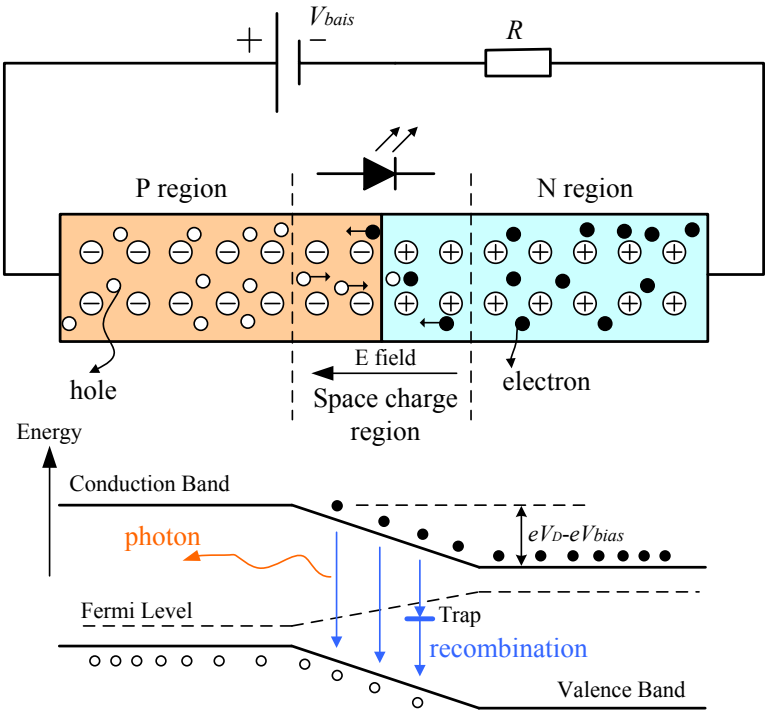

Figure 2.1: Effects of bias at the p-n junction of LED.

If an external bias is applied in forward direction (P region positive, N region negative) as shown in Fig. 2.1, the barrier height in the energy axis will reduce. If the forward bias is comparable with $\frac{E_g}{e}$, where E_g is the minimum band gap energy of the semiconductor material, the barrier height becomes small enough that a large amount of electrons are injected into the P region and holes into the N region. The excess diffusion of majority carriers will reduce the width of space

charge region and lead to weaker inner electric field strength with the increasing forward bias voltage. When a diffusing electron meets a hole in the space charge region, it falls from high occupied conduction band into a lower energy level, valence band, and releases energy in the form of photons. This action is known as *radiative combination*.

Not all electron-hole recombination emits lights. During *non-radiative recombination*, the electron energy is converted to heat, not lights. Usually, defects in the crystal are the most common cause for non-radiative recombination. These defects have energy level structures that are different from substitutional semiconductor atoms. Typical non-radiative transitions may take place via such deep levels (traps), as shown in the lower part of Fig. 2.1, or localized shallow state due to an impurity atom [101]. In light-emitting devices, non-radiative recombination events are indubitably unwanted. Some technologies in fabrication of LEDs aim to maximize the radiative process and minimize the non-radiative process.

If a reverse bias is applied, like the other common diodes, the majority carrier diffusion is prohibited due to the negative external electric field which forces the minority carriers to drift to corresponding regions so that the minimal reverse electric current flows across the p-n junction, called saturated current. The strength of the inner electric field increases as the reverse-bias voltage increases. Once the electric field intensity increases beyond a critical level, the p-n junction depletion zone breaks-down and current begins to flow, usually by either the zener or avalanche breakdown processes. Both of these breakdown processes are non-destructive and are reversible and the semiconductor will fail if excessive current is allowed.

2.2 Materials for LEDs

To have radiative emission, the band gap energy of the material must be at least equal to the required photon energy. Denoting λ as the wavelength of the light emitted, the minimum band gap energy E_g is:

$$E_g = \frac{hc}{\lambda} \tag{2.1}$$

where h is Planck's Constant, and c is the speed of light in vacuum. Thus, the wavelength of light emitted, and therefore its color, depend on the band gap energy of material forming the p-n junction. Certainly, the band gap energy depends on the semiconductor materials.

The basic materials for nearly all LEDs belong to the large class of group III–V compounds. LED development began with infrared and red devices made with GaAs. Advances in materials science have made possible the production of devices with ever-shorter wavelengths, producing light in a variety of colors. Current high brightness LEDs rely on three III–V heterostructure material systems, which are AlGaAs, AlGaInP and AlGaInN. AlGaAs LEDs emit red light. Colors of AlGaInP LEDs are mainly red, red-orange, or yellow and AlGaInN LEDs are for green, blue or white colors. They cover all the spectrum of visible lights that human eyes can perceive. The most recent development of the nitride material system yielded blue and near-UV LEDs, which made possible generation of white light.

2.3 Opto-Electrical Properties of LEDs

Because LEDs are direct band-gap semiconductor p-n junction, its energy band gap changes with temperature and current. This results in changes in the optical and electrical characteristics of LEDs. The detailed properties and perfor-

mance of LEDs are introduced as follows.

2.3.1 Current-Voltage Characteristic

The current-voltage (I-V) characteristic of LEDs accords with that of a common p-n junction. Its functional equation can be described as:

$$I = I_S(\exp \frac{eV}{nkT_j} - 1) \tag{2.2}$$

where I_S is the diode's reverse saturation current, k is Boltzmann's constant, n is the ideality factor and T_j is junction temperature in Kelvin scale.

Under reverse-bias conditions, V is negative and diode current saturates. I_S is dependent on many factors such as the active region area, charge carriers concentrations and their lifetimes. Under typical forward-bias conditions, the exponent of the exponential function in Eq. (2.2) illustrates that the current strongly increases as the diode voltage becomes large. It is noted that there is a voltage at which the current begins to increase rapidly, named as threshold voltage, V_{th}. This voltage can be given by $V_{th} \approx V_D \approx \frac{E_g}{e}$, determined by the semiconductor materials. Fig. 2.2 shows three I-V characteristics of RGB LEDs made from different materials. Along with different values of band gap energy, the red, green and blue LEDs have different threshold voltages.

Eq. (2.2) indicates that the I-V curve is affected by *junction temperature* T_j, which is actually the temperature of the active region crystal lattice. Junction temperature is a critical parameter to the LED characteristics. Heat contributed to junction temperature can be generated in the contacts, cladding layers, and the active region. The heat in the LED die can be diffused only by heat sink or external cooling whereas the conventional lamps can emit most heat by radiation. High junction temperature leads to low forward voltage when a constant forward current flows across the semiconductor. Fig. 2.3 demonstrates the characteristic

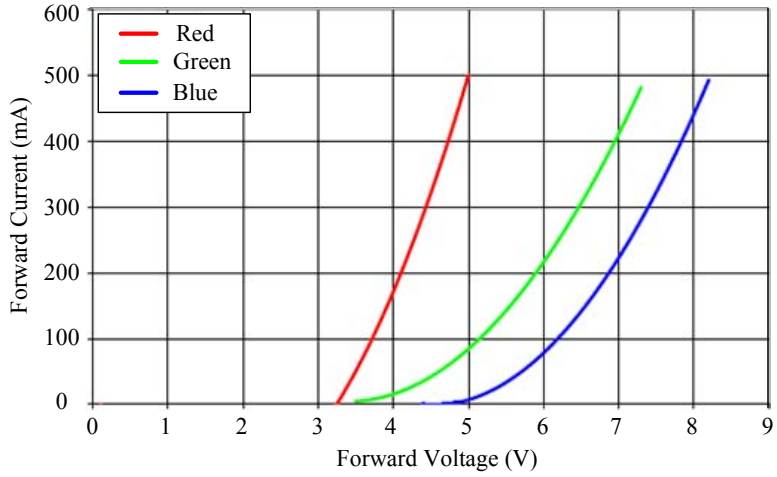

Figure 2.2: Forward current v.s. forward voltage of Lamina BL-4000 RGB LEDs at 25 °C ambient temperature. For each color, LEDs have 2 diodes connected in series [1].

variation on a sample red LED semiconductor due to the junction temperature change via adjusting the heat sink temperature.

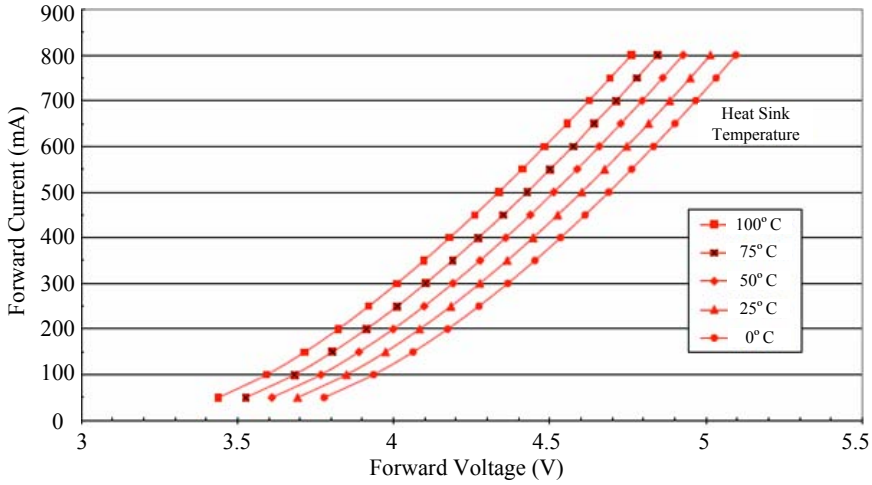

Figure 2.3: Forward current v.s. forward voltage of red Lamp in the package of Lamina NT-43F0-0424 RGB LEDs at different heat sink temperatures [2].

2.3.2 Luminous Flux Emission

From the previous elucidation, the active region of an ideal LED emits one photon for every electron injected. Thus, the ideal active region has an *internal quantum efficiency* of unity. Higher injection current denotes more recombina-

tion of electron-hole pairs and more simultaneous emission of photons. Photons emitted by the active region should escape from the LED die. In an ideal LED, all photons emitted by the active region are also emitted into free space. Such an LED has unity *extraction efficiency*. However, in a real LED, light emitted by the active region may be reabsorbed in the substrate of the LED or reflected back to the substrate, referred to as total internal reflection. Such possible mechanisms reduce the ability of light to escape from the semiconductor into the free space. The optical flux, also called radical flux, is the light power of a source emitted into the free space with the unit of watt (W). It is a radiometric quantity.

The recipient of the light is the human eye. It is observed that sensitivity of the human eye varies with the light wavelength. The luminous efficiency function or eye sensitivity function, $V(\lambda)$, provides the conversion between radiometry and photometry.

Luminous flux is a photometric quantity, representing the light power of a source perceived by the human eye. The unit of luminous flux is the lumen (lm). It is defined as follows: a monochromatic light source emitting an optical power of (1/683) watt at 555 nm has a luminous flux of 1 lumen. Accordingly, luminous flux, Φ, is obtained from the radiometric light power using the equation:

$$\Phi = 683\frac{\text{lm}}{\text{W}}\int_{\lambda} V(\lambda)P(\lambda)d\lambda, \tag{2.3}$$

where $P(\lambda)$ is the spectral power density, i.e., the light power emitted per unit wavelength. Meanwhile, the optical power emitted by a light source is given by

$$P = \int_{\lambda} P(\lambda)d\lambda \tag{2.4}$$

Luminous efficacy is defined as below with the unit of lm/W.

$$\text{luminous efficacy} = \frac{\Phi}{P} = 683\frac{\text{lm}}{\text{W}}\frac{\int_{\lambda} V(\lambda)P(\lambda)d\lambda}{\int_{\lambda} P(\lambda)d\lambda}, \tag{2.5}$$

Larger injection current increases the amount of photons released, therefore luminous flux. But the luminous flux is not linear with the injected current. This is caused by the reduced internal quantum efficiency, where the increased injection electrons increase the chance of non-radiative recombination. Fig. 2.4 shows the trends of luminous flux with the increasing forward current at the junction temperature of 25 °C.

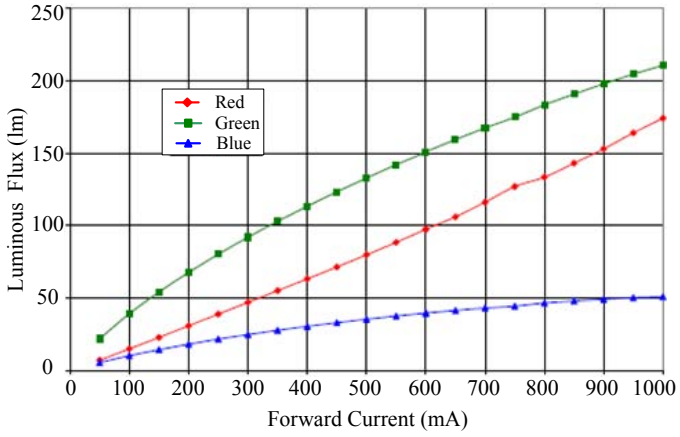

Figure 2.4: Luminous flux v.s. forward current of Lamina NT-43F0-0424 RGB LEDs at junction temperature T_j = 25 °C [2].

Moveover, the internal quantum efficiency also depends on the junction temperature. Fig. 2.5 depicts the luminous flux degradation due to the increasing junction temperature.

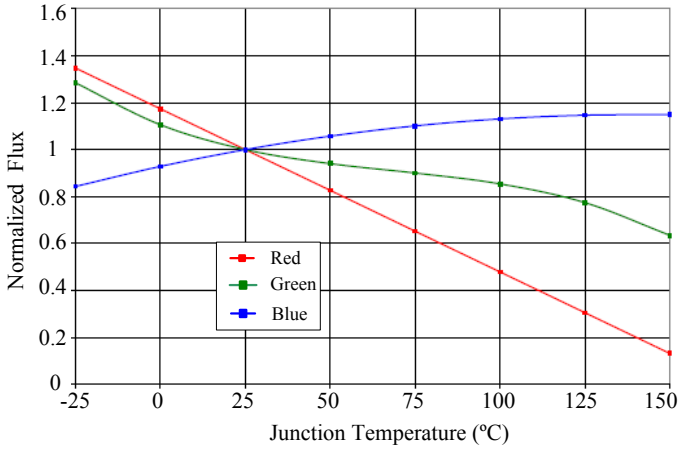

Figure 2.5: Normalized flux v.s. junction temperature of Lamina NT-43F0-0424 RGB LEDs at forward current I_F = 350 mA [2].

2.3.3 Light Spectrum Characteristic

The spectrum of LED emission is relatively narrow compared with the range of the entire visible spectrum (from 370 nm to 830 nm), and therefore LED emission is perceived by the human eye as *monochromatic*. The dominant emission wavelength depends on the band gap energy of an LED semiconductor. Hereby, the dominant wavelength of LED spectra will shift with the junction temperature and the driving current. It is reported that the dominant wavelength will shift toward longer wavelengths with increasing temperature [49]. Fig. 2.6 shows the dominant wavelength shifts with the junction temperature and the forward current. The wavelength shift is large up to ten nanometer that color point variation of the emitted light may be perceived by the human eye.

2.3.4 Lifetime and Failure

LEDs have preponderant long lifetime up to 100,000 hours, competing with other lamps such as incandescent lamps with only 1000 hours, fluorescent lamps with about 20,000 hours, and HID lamps with 30,000 hours.

The most common symptom of LED failure is the gradual lowering of the light output and the efficiency loss. Sudden failure, unlike incandescent and fluorescent lamps, is rare. To quantitatively classify lifetime in a standardized manner it has been suggested to use the terms L75 and L50 which are the times it will take for a given LED to reach 75 % and 50 % light output respectively. With the development of high-power LEDs, the devices are subjected to higher junction temperatures and higher current densities than traditional devices. This will cause stress on the material and may cause early light-output degradation, as shown in Fig. 2.7.

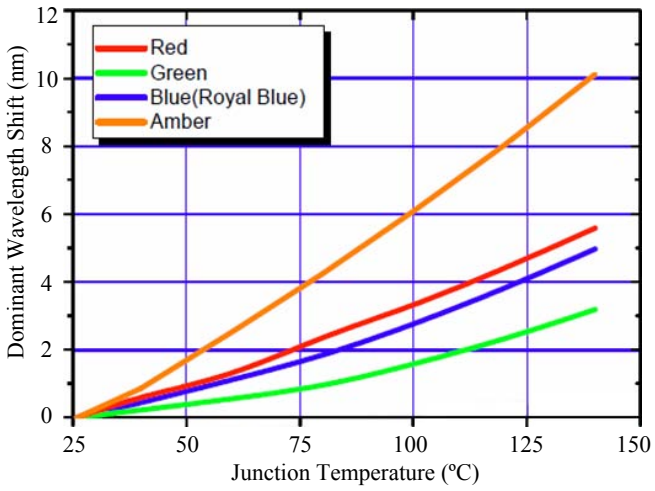

(a)

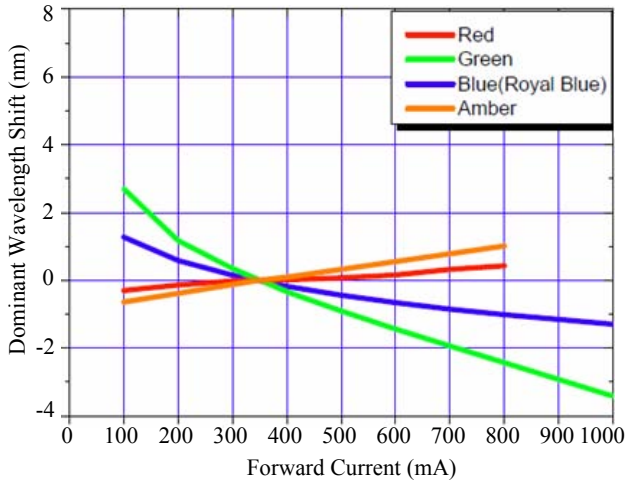

(b)

Figure 2.6: Dominant wavelength shift of Seoul Semi Z-Power LEDs [3]. (a) Dominant wavelength shift v.s. junction temperature at forward current I_F = 350 mA. (b) Dominant wavelength shift v.s. forward current at ambient temperature T_A = 25 °C.

2.4 Color and White Light with LEDs

LEDs are monochromatic light sources. Mixing different monochromatic LEDs can produce color lights, including white light. To quantify the sensation of color, CIE has defined *color spaces* and standardized the measurement of color by means of *color-matching functions* and *chromaticity diagrams*.

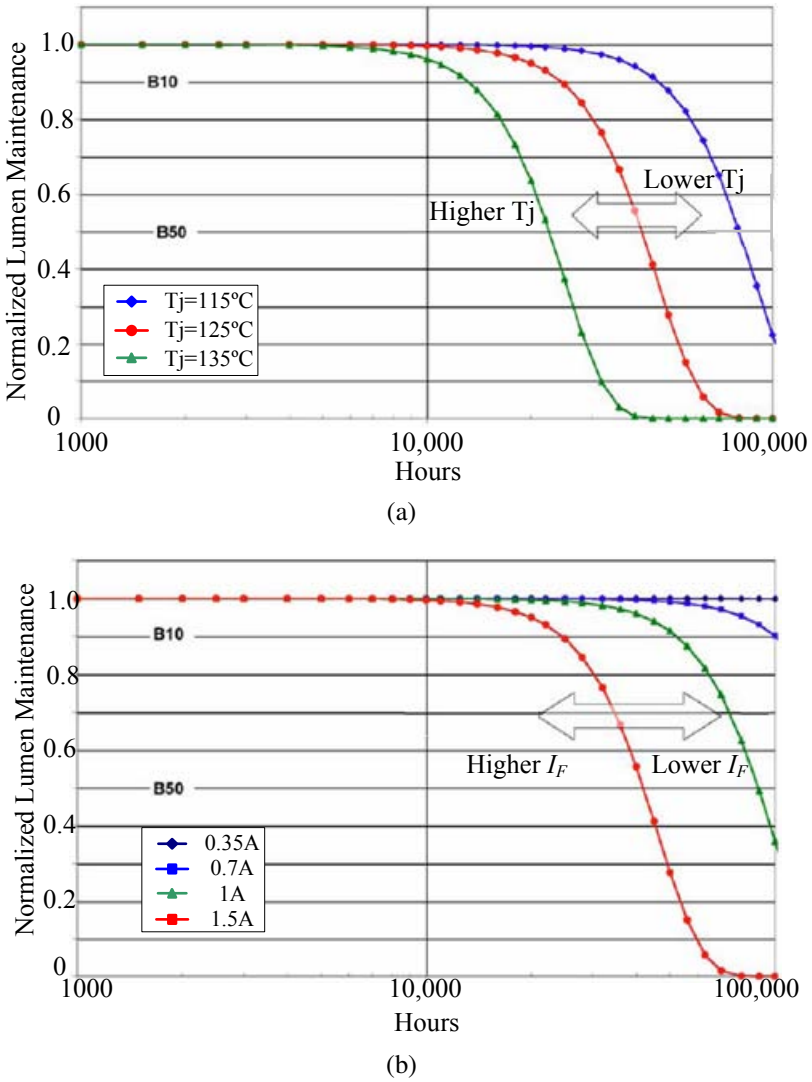

Figure 2.7: Useful lifetime of an Lumileds Luxeon K2 white LED [4]. (a) For different junction temperatures at I_F = 1.5 A. (b) For different forward currents at T_j = 125 °C.

The CIE 1931 XYZ color space is one of color spaces, which uses three tristimulus X, Y, and Z to describe a color sensation. The tristimulus values of a color are the amounts of three RGB primary colors (ideal and not existent in the light spectrum) in a three-component additive color model needed to match that test color. Color-matching functions, called $\overline{x}(\lambda)$, $\overline{y}(\lambda)$, and $\overline{z}(\lambda)$, are the numerical description of the chromatic response of the CIE standard observer. For a given spectral power density, $P(\lambda)$, the degree of stimulation required to

match the color of $P(\lambda)$ is given by

$$\begin{aligned} X &= \int_{\lambda} \overline{x}(\lambda) P(\lambda) d\lambda \\ Y &= \int_{\lambda} \overline{y}(\lambda) P(\lambda) d\lambda \\ Z &= \int_{\lambda} \overline{z}(\lambda) P(\lambda) d\lambda \end{aligned} \tag{2.6}$$

The CIE XYZ color space was deliberately designed so that the Y parameter was a measure of the brightness or luminance of a color. The chromaticity of a color was then specified by the two derived chromaticity coordinates u' and v' in Eq. (2.7).

$$\begin{aligned} u' &= \frac{4X}{X + 15Y + 3Z} \\ v' &= \frac{9Y}{X + 15Y + 3Z} \end{aligned} \tag{2.7}$$

The relative CIE 1976 (u', v') chromaticity diagram can be plotted as shown in Fig. 2.8. Monochromatic or pure colors are found on the perimeter of the chromaticity diagram. White light is found in the middle of the diagram. All visible colors can be characterized in terms of their locations in the chromaticity diagram.

From Eqs. (2.6) and (2.7), the chromaticity coordinate of light is a linear combination of the individual chromaticity coordinates. The principle of color mixing in the chromaticity diagram is shown in Fig. 2.8. The mixing of two colors will produce all colors in the straight line connecting the chromaticity coordinates of the two colors. Likewise, three colors, typical RGB colors, will be mixed to generate all colors in the enclosed triangle, called *color gamut*. The mixing of multi-component light has the same principle. Usually, RGB color mixing is commonly used in practice to produce the color or white light. Adjusting the intensities of RGB LEDs, the color of mixed light can be changed

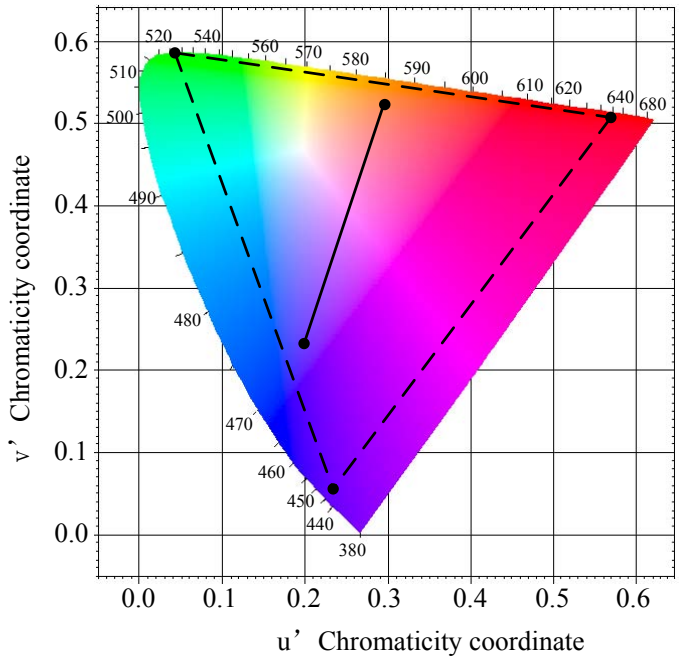

Figure 2.8: CIE 1976 (u', v') chromaticity diagram. The outer curved boundary is the monochromatic locus with wavelengths shown in nanometers.

instantly. Besides using RGB color-mixing, there is another method to make white light, namely phosphor-conversion LEDs. A blue or UV LED is utilized to emit the blue or UV light, which excites the phosphor and emits light with a longer wavelength. The synthetical light is white light.

There are several qualified indexes in colorimetry to define and quantify the light quality. According to these indexes, some international standards guide the manufacturers for qualifying LED luminaires.

Color Difference

Human eyes can detect color changes. The color difference of two light colors in the CIE 1976 chromaticity diagram is the distance between chromaticity coordinates of two colors and can be represented by $\Delta u'v'$ where

$$\Delta u'v' = \sqrt{(u' - u'_o)^2 + (v' - v'_o)^2} \tag{2.8}$$

(u'_o, v'_o) is the acquired chromaticity coordinate and (u', v') is the chromaticity coordinate of the measured light. The CIE (u', v') chromaticity diagram provides the color difference perceived by human eyes, which is approximately proportional to the geometric distance. Usually, a color distance of $\Delta u'v' < 0.0035$ is indistinguishable to human eyes.

Color Rendering Index

The white light used for illumination has to hold the ability to properly render the true color of the objects irradiated by the white light. The ability to render the color of an object is assessed in terms of *color rendering index* (CRI). CRI can be labeled from 0 to 100. A higher CRI denotes a better color rendering ability, which means that the light source is closer to sunlight and suitable for illumination. Incandescent lights are regarded as approximate sunlight with CRI of 100. Nowadays, white LEDs have a relatively high CRI of more than 75, as shown in Table. 1.1.

Correlated Color Temperature

Relying on the color-mixing mechanism, every color point including the white color in the chromaticity diagram will have a number of optical spectra to generate the light at this chromaticity coordinate. To standardize the spectrum of the white light, the Planckian black-body radiation spectrum is used as one standard, which is changing only with the temperature of the body, namely *color temperature*. With increasing temperature, the wavelength of the black-body radiation spectrum becomes shorter. Therefore, a series of points are located in the chromaticity diagram at different temperatures and the trace is called Planckian locus. If the color of white light is not located on the locus, but close to the curve, *correlated color temperature* (CCT) is used to define its color temperature, whose

color coordinate is closest to the color of the evaluated white color.

2.5 Requirements for LED Luminaires

LED luminaire is a complete LED lighting system consisting of a light source and a driver (or ballast) together with parts to distribute light, to position and protect the light source, and to connect the light source to the electrical power grid. To utilize the LED luminaires reasonably, some international commissions have made lighting industry reference standards and require the products to meet the criteria. Typically, there are two well-known standards: Energy Star program requirements for solid state lightings (SSL) specified by Department of Energy, U.S. [102] and International Electrotechnical Commission (IEC) standards [103].

The Energy Star criteria cover the requirements for SSL products used for general illumination, including those with significant decorative functions. It does not apply to the indication applications such as traffic lights and exit signs. The requirements can be divided into two parts focusing on LED light sources and ballasts. For the LED light sources, CCT must accord with one of the 8 nominal CCTs within an accepted tolerance: 2700 K, 3000 K, 3500 K, 4000 K, 4500 K, 5000 K, 5700 K, 6500 K. CRI is no less than 75 for indoor applications. Lifetime, defined as the duration within which the output lumen is kept to 70 % of the initial lumens, must compete with 35,000 hours. Moreover, over the lifetime, the change of chromaticity should be within 0.007 and the variation of chromaticity in different directions should be within 0.004 on the CIE (u', v') chromaticity diagram. Besides, additional requirements for CCT, luminaire efficiency, zonal lumen density, and minimum light output are defined for some special applications, for example, portable desk task lights, outdoor pathway lights and so on.

For the power supply requirements, the power factor must be no less than 0.9 for commercial products and 0.7 for residential products. The operating fre-

quency of LEDs should be above 100 Hz to avoid visible flickers. The minimum operation temperature, noise and transient response are also taken into consideration.

IEC publishes international standards for all electrical, electronic and related technologies. IEC standards are categorized by assessment functions. Therefore, the following reference documents apply to LED luminaires. EN 60598 [104] specifies general requirements for luminaires covering classification, marking, mechanical and electrical constructions, where luminaires can be incandescent, fluorescent, HID, and LED lamps. 25 subsections are grouped by a particular usage, e.g. floodlight and hand-lamps, and additional requirements are added and detailed in each subsection. EN 62031 [105] is a safety standard for LED modules for general lighting applications. The standard presents the technical knowledge from the fields of the semiconductor industry and those of the traditional electrical lamps. Also, EN61347 part 2-13 [106] specifies particular safety requirements for the electronic control gear of LED modules. Moreover, emission of radio-frequency disturbances from all lighting equipment is limited in EN 55015 [107] and electromagnetic compatibility requirements are listed in EN 61000 [86].

In particular, EN 61000 part 3-2 applies to all kinds of electrical and electronic equipment that have an input current of up to 16 A per phase and deals with the limits of harmonic currents injected into the public supply system. Unlike the power factor requirement of Energy Star, it specifies limits of harmonic components of the input current which may be produced by different types of equipment. The standard establishes 4 classes of equipment, each with its own harmonic emission limits. All kinds of lighting equipment including dimmers with input power above 25 W should comply with Class C limits while the equipment with power below 25 W should satisfy Class D limits. The harmonic limit of each order is listed in Table. 2.1.

Although IEC has not proposed rigorous requirements about the LED light

Table 2.1: Current limits for lighting equipment with Class C ($\geq$ 25 W) and Class D ($<$ 25 W).

Harmonic order n	Maximum permissible harmonic current (%) for Class C	Harmonic order n	Maximum permissible harmonic current (mA/W) for Class D
2	2		
3	30 · circuit power factor	3	3.4
5	10	5	1.9
7	7	7	1.0
9	5	9	0.5
$11 \leq n \leq 39$ (odd only)	3	11	0.35
		$13 \leq n \leq 39$ (odd only)	3.85/ n

quality, good quality of input current is imposed in the design of electric ballasts by both commissions. To shape the input current, the PFC pre-regulators become necessary in electric ballasts. The principles of different PFC techniques, such as average current control, current programmed control, critical conduction mode and hysteretic control etc, as well as the basics of the power converters can easily be found in [108, 109]. And for cost and maintenance consideration, the electric ballast must have size saving, longevity matching with that of LED sources and high efficiency for energy saving.

2.6 Summary

In this chapter, we have briefly reviewed the thermal, electrical and optical characteristics of LEDs. The optical to thermal and electrical characteristics are nonlinear. Our focus in this research is to find techniques which can overcome the nonlinearities and construct an effective LED driver system to meet the requirements of different applications. In Chapter 3, an effective color control method using a junction temperature measurement technique is proposed, analyzed, and experimentally verified. Combined with the color control method, LED ballasts are explored with independent brightness control in Chapter 4 and further effi-

ciency improvement in Chapter 5. In Chapter 6, we propose an economical and high-efficiency LED ballast for general applications supporting ordinary incandescent dimming devices.

Chapter 3

Light Color Stabilization Using Temperature Measurement Technique

3.1 Introduction

In Chapter 2, LEDs are introduced as direct band-gap semiconductor p-n junction diodes. The band gap of the semiconductor, controlled by mixing different proportions of III-V elements from the Periodic Table, defines the light color frequency of the diode. The band gap of the LED therefore changes from time to time during operation where the junction temperature changes with the power dissipation and the ambient temperature. The LED junction temperature estimation has been done using linear current drivers [79]. However, in practice, LEDs are often driven by switching power converters for the better efficiency, causing difficulties in measuring signals buried in the noisy switching environment. This also poses engineering challenges in correcting color drifts due to device and temperature variations.

In this chapter, we will focus on the color drift due to the temperature vari-

ation. The nonlinearity of the forward driving current to the LED light and the color output can be reduced dramatically using the PWM control of the fixed forward current drive, resulting in a one-step calibration of the device variation compensation at some chosen light intensity outputs. A simple and practical technique for color control is proposed here by measuring the optical and electrical characteristics of the LED during the turn-on duration of the PWM forward driving current. The forward-voltage-to-junction-temperature variation is roughly linear under the fixed driving current. This property has been widely exploited for sensing the ambient temperature. Thus, the temperature compensation can be achieved by detecting instantly the diode forward voltage with some proper noise reduction techniques.

Section 4.2 gives an overview of the RGB LED color lighting system. The LED diode junction temperature compensation technique is given in Section 3.3. Implementation details of the system are given in Section 3.4. The performance of the proposed compensation technique is evaluated in Section 3.5. Section 3.6 concludes this chapter.

3.2 Overview of RGB LED Color Control

The data points on the CIE 1976 chromaticity diagram shown in Fig. 3.1 give the color coordinates (u', v') of typical red, green and blue LEDs having wavelengths from 380 nm to 700 nm for a step size of 5 nm. The diagram was made in a way to give an even color perceptible difference for the distance of two color points independent of the absolute positions of the color points. A color distance of $\Delta u'v' = \sqrt{(\Delta u')^2 + (\Delta v')^2} < 0.0035$ is indistinguishable to human eyes. Errors within this small distance are considered very acceptable for most applications. Mixing the light intensity of the three LEDs having wavelengths of 624 nm, 525 nm and 465 nm can produce all colors within the triangle whose corners are at the color coordinates of the RGB LEDs. The color accuracy of light

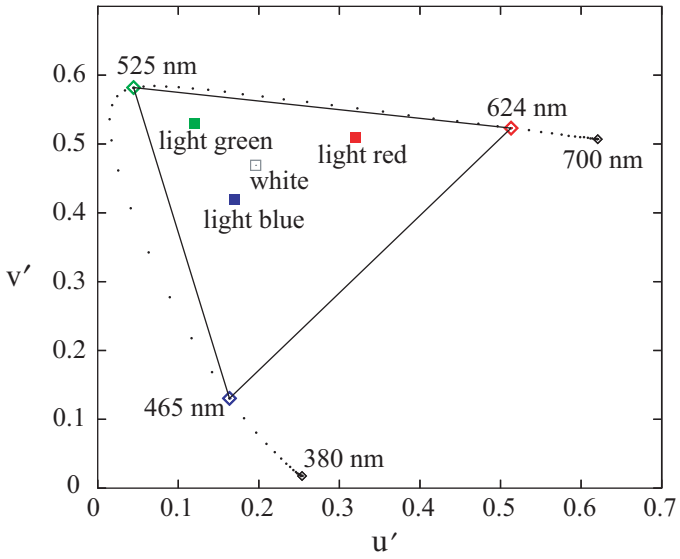

Figure 3.1: Color coordinates of typical LED of center wavelengths ranging from 700 nm to 380 nm. Adjacent dots are separated by 5 nm in center wavelength. LEDs with center wavelengths of 624 nm (red), 525 nm (green) and 465 nm (blue) can generate color points such as white, light red, light green and light blue within the triangle shown in this figure.

mixed by the RGB LEDs is therefore dependent on 1) the stability of the color points of the RGB LEDs; and 2) the accuracy of LED light dimming method.

The color accuracy at color points of white, light red, light green and light blue within the triangle in Fig. 3.1 will be used for the evaluation of the proposed compensation technique in Section 3.5.

We assume that the light stability of color points of LEDs is largely dependent on the junction temperatures T_R, T_G and T_B of the red, green, and blue diodes. Like in other previous studies [19, 42, 46, 49, 50, 90, 110], the effects of component aging are ignored here. Such effects can be compensated using a similar technique here and taking into consideration the thermal history in relation to device aging. Alternatively, the aging speed can be effectively controlled by limiting the LED temperatures below a maximum threshold. The aging process thus is very slow and does not affect the result of our proposed temperature compensation technique. If desired, it can also be compensated by regular calibrations

using additional LED light measurement fixtures for specific applications.

An intended light output is usually expressed in terms of the so called *tristimulus,* denoted by $\boldsymbol{X} = (X\ Y\ Z)^t$, and also the *dimming factor,* denoted by $\boldsymbol{d} = (d_r\ d_g\ d_b)^t$ and given by

$$\boldsymbol{d} = \boldsymbol{f_T}(\boldsymbol{X}), \tag{3.1}$$

where $\boldsymbol{f_T}$ is a column vector function whose parameters change with $\boldsymbol{T}$, which is a column vector of the LED junction temperatures, i.e., $\boldsymbol{T} = (T_R\ T_G\ T_B)^t$. Note that $\boldsymbol{T}$ depends on both $\boldsymbol{d}$ and the ambient temperature.

Without precise information of the temperature change inside the LED diode junction, the control of the light output from Eq. (3.1) can only be achieved by a feedback loop that senses the light outputs from the RGB LEDs and adjusts the control parameter $\boldsymbol{d}$ to compensate for the light output drifts as defined from $\boldsymbol{f_T}$ [49]. Indirect temperature compensation techniques like sensing the temperature of the heat sink on which the LEDs are mounted [50, 111] may suffer from poor response to the change in temperature [110]. Although the method used in [110] measures the LED forward voltage directly, it does not use PWM control for simplicity. The method of two-diode driving voltages [19] may cause excessive errors in estimating the diode junction temperature and increase the system complexity. Thus, light sensing is still important for ensuring high performance.

3.3 Technique of Junction Temperature Compensation and Experimental Measurements

Eq. (3.1) can be highly nonlinear if inappropriate control methods and/or working color ranges are used [110]. It is widely known that dimming using PWM is preferred over the use of amplitude modulation because of the linear

relationship between the duty cycle $\boldsymbol{d}$ and the LED color light output. We have confirmed this by experimental measurement, as shown in Figs. 3.2 (a), (b) and (c). The tristimulus $\boldsymbol{X} = (X\ Y\ Z)^t$ changes linearly with the junction temperature and hence also with the A/D converted values of RGB diode voltages when drivers operate at a stable duty cycle as in Fig. 3.2 (d). Also, the tristimulus $\boldsymbol{X}$ changes linearly with the duty cycle at a stable junction temperature. Measurement errors due to switching noise and digitization can be reduced by the method of boxcar averaging. So, we can simply measure the above linear correspondence at several duty cycle values, such as in Figs. 3.2 (a), (b) and (c) and derive the corresponding tristimulus at the other duty cycle values accordingly. The linearity of the dependence of RGB lights on the RGB diode voltages makes programming very simple. Moreover, the color points of the LEDs with center wavelengths of 624 nm (red), 525 nm (green) and 465 nm (blue) in Fig. 3.1 drifts with the increase in junction temperature caused by heat sink temperature are very significant, as illustrated in Fig. 3.3 where the color variation $\Delta u'v'$ can be as high as 0.026 for a change of heat sink temperature from 30 °C to 82 °C for the blue LED.

We use the Lamina BL-4000 RGB LED light engine [1] to illustrate how essential parameters contained in $\boldsymbol{f_T}$ of Eq. (3.1) can be found. Each color channel of the RGB LED consists of a series connection of two corresponding color LEDs. The LEDs behave essentially as diodes with a higher cut-in voltage. At a typical driving current of 350 mA to each color channel, the LED produces forward diode voltages of 4.5 V, 6.7 V and 7.6 V for red, green and blue channel LEDs respectively. At this driving current, they consume a total electrical power of 6.7 W and provide a total luminous flux of 120 lm. At any forward diode voltage below 3 V, the LEDs consume virtually no electrical power. In our experimental setup, a constant current of 330 mA during the turn-on duration of the PWM cycle is applied to all the red, green and blue LEDs at ambient temperature. We have measured data indicated in Figs. 3.2 (a), (b) and (c) to obtain $\boldsymbol{X}_{or}$, $\boldsymbol{X}_{og}$, and $\boldsymbol{X}_{ob}$ versus diode forward voltages of the LEDs, i.e., V_{dr}, V_{dg} and V_{db},

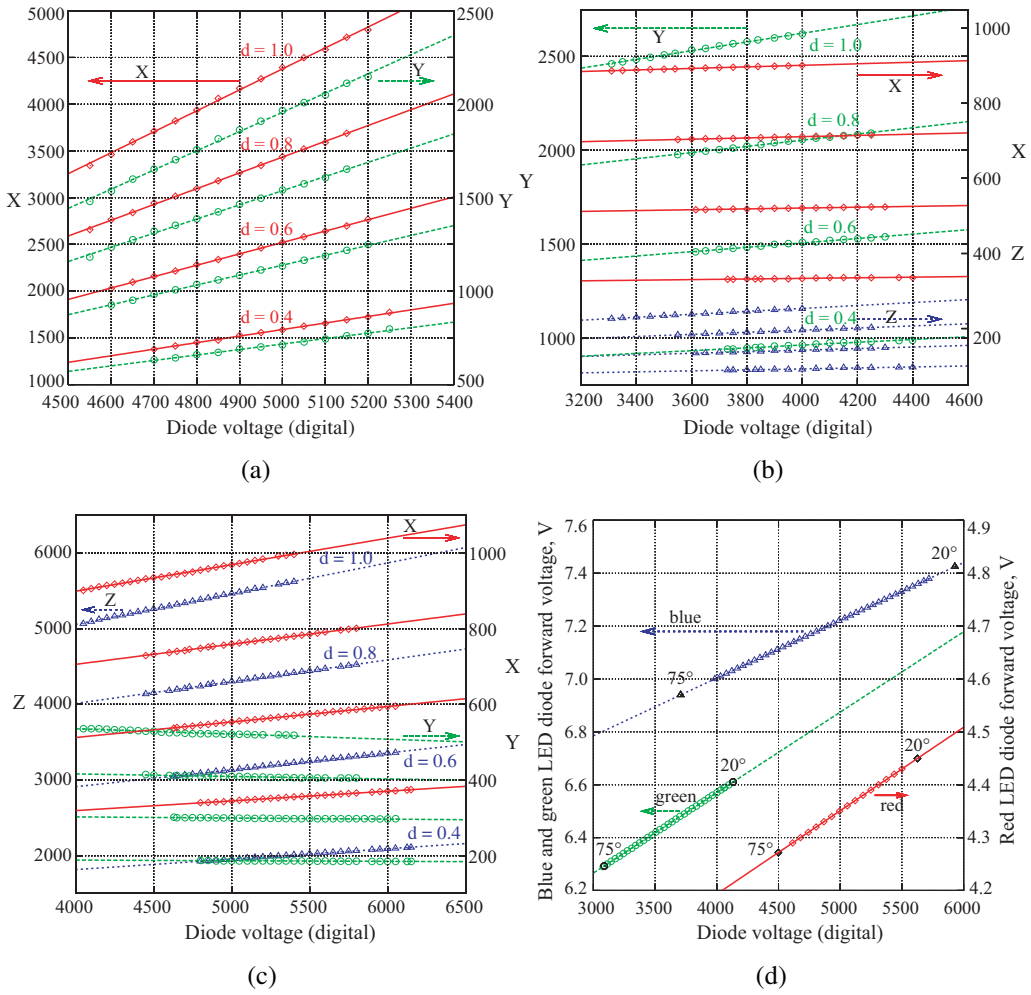

Figure 3.2: Experimental light tristimulus $\boldsymbol{X}$ versus diode voltage (digital) of (a) red LED light, (b) green LED light and (c) blue LED light at different duty cycles. Diamonds, circles and triangles are data points for X, Y and Z respectively and lines are fitted with the data points. Duty cycles are descending from top to bottom with d = 1.0 to d = 0.4 respectively for each component in $\boldsymbol{X}$. Note that Z in $\boldsymbol{X}$ of red light is almost zero and not shown in this figure. (d) gives relationships between actual (two diodes in series connection) diode forward voltage and digital temperature V_{di} for $i = r, g, b$. The data points in (d) are measured using heat sink temperature as variation parameter ranging from 20 °C to 75 °C in obtaining the corresponding diode forward voltages (junction temperatures).

at (d_r, d_g, d_b) = (1, 1, 1), (0.8, 0.8, 0.8), (0.6, 0.6, 0.6), and (0.4, 0.4, 0.4). We use the LED heat sink temperature as the variation parameter. Sufficient time is allowed for the forward diode voltages to settle down before taking measurements. Thus, diode forward voltages (junction temperatures) are measured with one-to-

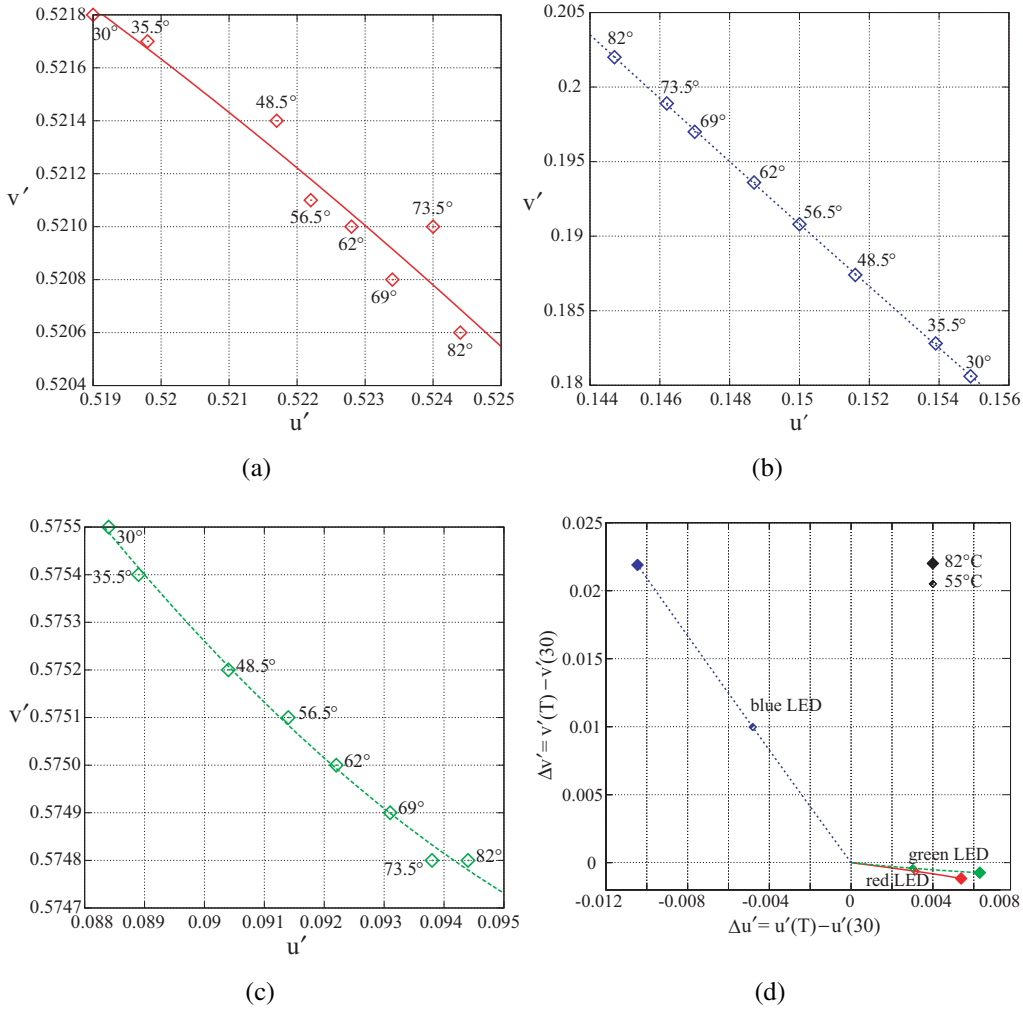

Figure 3.3: Evaluation of color points of the LEDs with center wavelengths of 624 nm (red), 525 nm (green) and 465 nm (blue), marked with small diamonds, changing with different heat sink temperatures for a constant current driven (a) red (b) blue and (c) green LEDs. Lines are least-square-fits of data points using second degree polynomials. Shown in (d) are corresponding drifts of color points relative to the color point at heat sink temperature of 30 °C. Note that the color space of CIE 1976 uniform chromaticity scale is used here to give an even perceptual color difference.

one correspondence to heat sink temperatures. We will show later in Section 3.4 that heat sink temperature and junction temperatures indicated by diode forward voltages can vary differently depending on diode working conditions.

As explained in Section 3.2, the mixed color is therefore given as

$$\begin{pmatrix} X_o \\ Y_o \\ Z_o \end{pmatrix} = d_r \begin{pmatrix} X_{or} \\ Y_{or} \\ Z_{or} \end{pmatrix} + d_g \begin{pmatrix} X_{og} \\ Y_{og} \\ Z_{og} \end{pmatrix} + d_b \begin{pmatrix} X_{ob} \\ Y_{ob} \\ Z_{ob} \end{pmatrix} \tag{3.2}$$

where

$$\begin{pmatrix} X_{oi} \\ Y_{oi} \\ Z_{oi} \end{pmatrix} = \begin{pmatrix} \alpha_{i1} V_{di} + \alpha_{i2} \\ \alpha_{i3} V_{di} + \alpha_{i4} \\ \alpha_{i5} V_{di} + \alpha_{i6} \end{pmatrix} \tag{3.3}$$

with $i = r, g, b$ and α_{ij} being coefficients of least square fits from Figs. 3.2 (a), (b) and (c).

Since $\mathbf{X}_{or}$, $\mathbf{X}_{og}$, and $\mathbf{X}_{ob}$ are linearly independent, it is always possible to determine a unique **d** such that (3.2) is satisfied. If $\mathbf{X}_{or}$, $\mathbf{X}_{og}$, and $\mathbf{X}_{ob}$ are temperature invariant and **d** is well controlled, the light color output will be very stable as given in (3.2). However, the three color bases $\mathbf{X}_{or}$, $\mathbf{X}_{og}$, and $\mathbf{X}_{ob}$ are temperature dependent, as given in (3.3). Using (3.2) and (3.3), the desired color can be achieved. This technique will be implemented in Section 3.4 and evaluated in Section 3.5.

The transformation of (X, Y, Z) to other CIE color space systems is monotonic. For instance, the relation between XYZ (tristimulus) and $u'v'$ (chromaticity) is simply as Eq. (2.7). The whole process can be done automatically with the help of a well calibrated visible light spectrometer.

3.4 Implementation of RGB LED Junction Temperature Measurement Technique in Light Color Stabilization

The Lamina BL-4000 RGB LED light engine is selected for detailed study and illustration. We use switching converters as LED drivers to improve the power efficiency. Each red, green and blue light channel is driven separately by a current-controlled switching converter, as shown in Fig. 3.4. The switching converter behaves essentially as a current source whose magnitude is controlled by a PWM signal. Our converter is modified from a control IC LT1510 designed for battery chargers operating at a switching frequency of 200 kHz [112]. Component values have been optimized for fast transient of the output current under a PWM gate pulse, V_{PWM}, which is applied at a frequency of 200 Hz to the MOS transistor, as shown in Fig. 3.4.

Three identical circuits, each resembling Fig. 3.4, are used for driving the red, green and blue LED channels, the schematic of which is shown in Fig. 3.5.

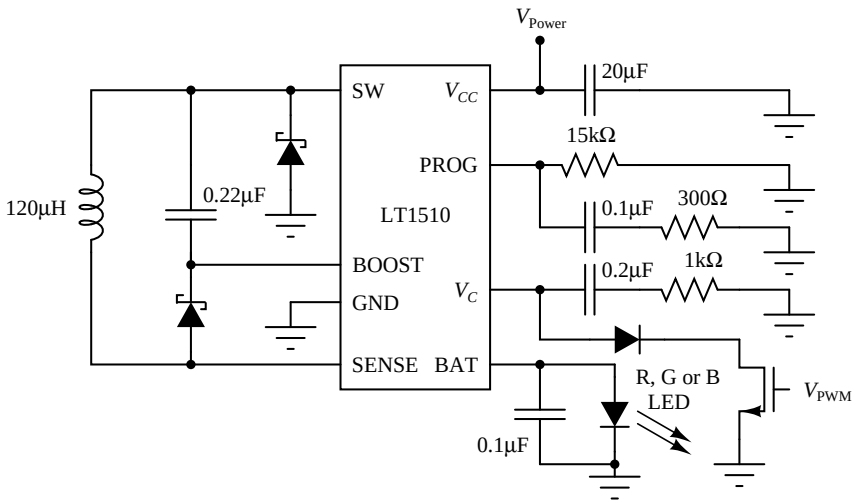

Figure 3.4: Switching converter with PWM control as constant current driver.

The LED drivers are controlled by the microcontroller PIC18F1320. Fig. 3.6 shows a photo of the LED with the microcontroller and power converters. Fig. 3.7 shows typical waveforms of the forward voltage across the red, green and blue diodes under the constant current at 330 mA which is pulse-width modulated for the brightness control. The power flow of the buck switching power converter shown in Fig. 3.4 is unidirectional. When the current source turns on, the diode

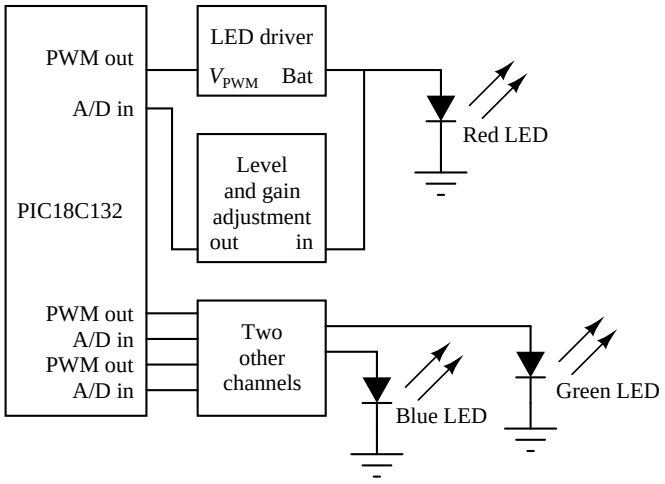

Figure 3.5: Schematic of the RGB LED color control system.

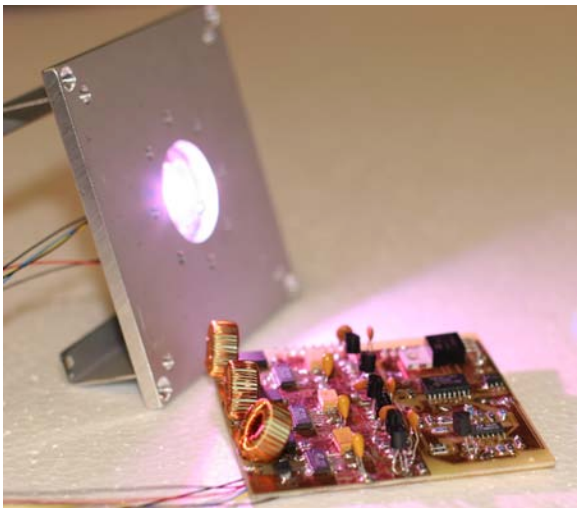

Figure 3.6: LED lamp with LED microcontroller system which is composed of three PWM current drivers and PIC18F1320 control circuitries.

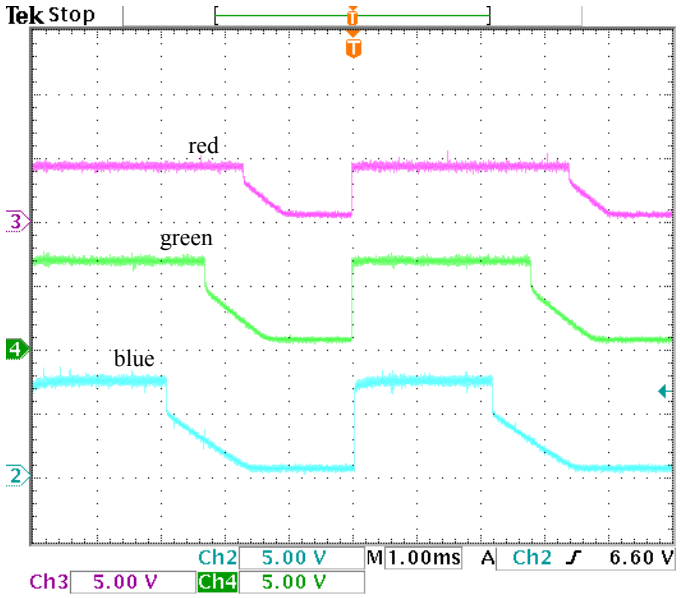

Figure 3.7: LED diode forward voltage waveforms; upper trace for red LED, middle trace for green LED and lower trace for blue LED.

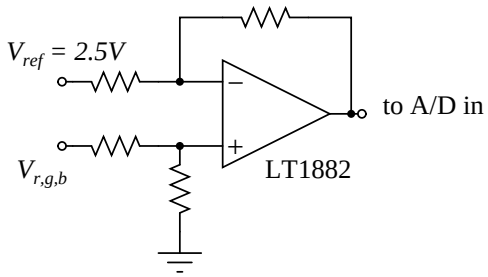

Figure 3.8: Functional block "level and gain adjustment" of Fig. 3.5.

voltage increases abruptly. When the current source turns off, the small ripple filtering capacitor of 0.1 μF discharges its energy to the diode. The diode voltage drops rapidly when it is above the diode cut-in voltage, where the diode current is at its high level. When the diode voltage falls below the diode cut-in voltage, the diode current becomes very small. Thus we observe a slow decay of the diode voltage after the current source turns off. However, as the charge of the 0.1 μF is small, it contributes negligibly to the brightness of the LEDs. Then, the voltage during the turn-on duration is detected and converted to the digital format suitable for the PIC18F1320 programming.

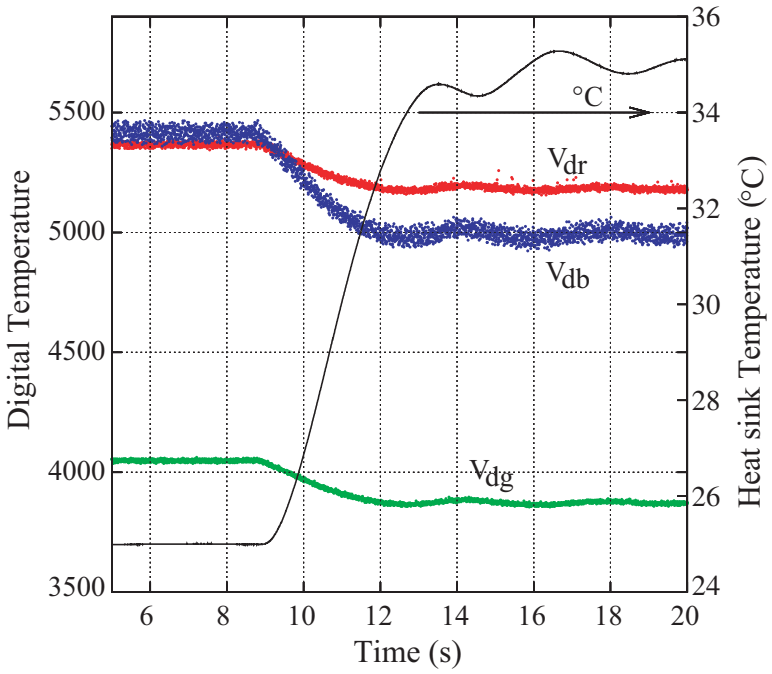

Figure 3.9: Comparison of digital diode forward voltage V_{di} and heat sink temperature. The LEDs are driven by PWM current of 330 mA and duty cycle of d = 0.8. Heat sink temperature is externally controlled for a step change from 25 °C to 35 °C at $t = 9$ s.

During the calibration phase, the digital format of the scaled diode turn-on voltages as in Fig. 3.2 (d) is sent from the PIC18F1320 to a personal computer via the RS232 connection at a rate of 200 samples per second. A voltage scaling circuit shown in Fig. 3.8 is used for the functional block "level and gain adjustment". The scaling relationships are given as

$$V_{dr} = 6328.2V_r - 22533, \tag{3.4}$$

$$V_{dg} = 3286.9V_g - 17968, \tag{3.5}$$

$$V_{db} = 4577.6V_b - 28059, \tag{3.6}$$

where V_i $(i = r, g, b)$ is the actual diode turn-on voltage in volt.

The digital temperature V_{di} $(i = r, g, b)$ being boxcar averaged for the noise

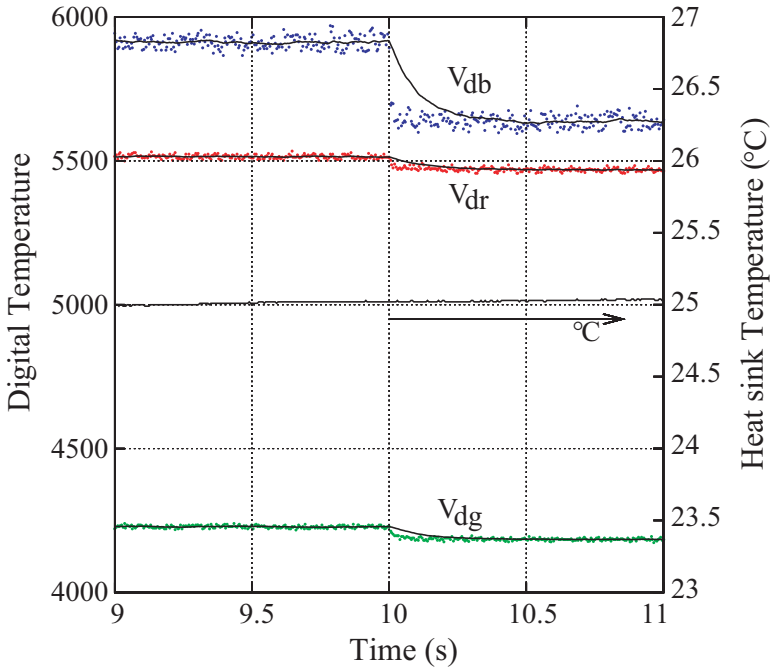

Figure 3.10: Comparison of digital diode forward voltage V_{di} and heat sink temperature. The sampled digital diode forward voltages are shown as dots and the lines superimposed with the dots are calculated using Eq. (3.7). The LEDs are driven by PWM current of 330 mA and duty cycle of $d = 0.5$. Heat sink temperature is kept at 25 °C while a step change from $d = 0.5$ to $d = 0.8$ is applied to the blue channel.

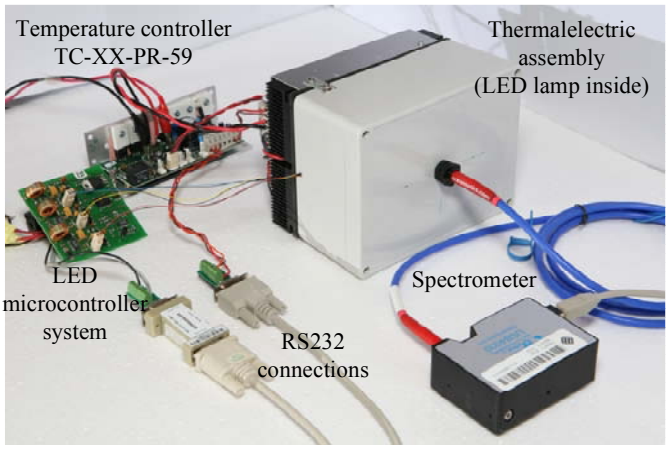

Figure 3.11: Automatic measurement and calibration suite.

reduction is further smoothened using a simple integrator formula, i.e.,

$$V_{di,\text{current}} = \beta V_{di,\text{measured}} + (1 - \beta) V_{di,\text{previous}} \tag{3.7}$$

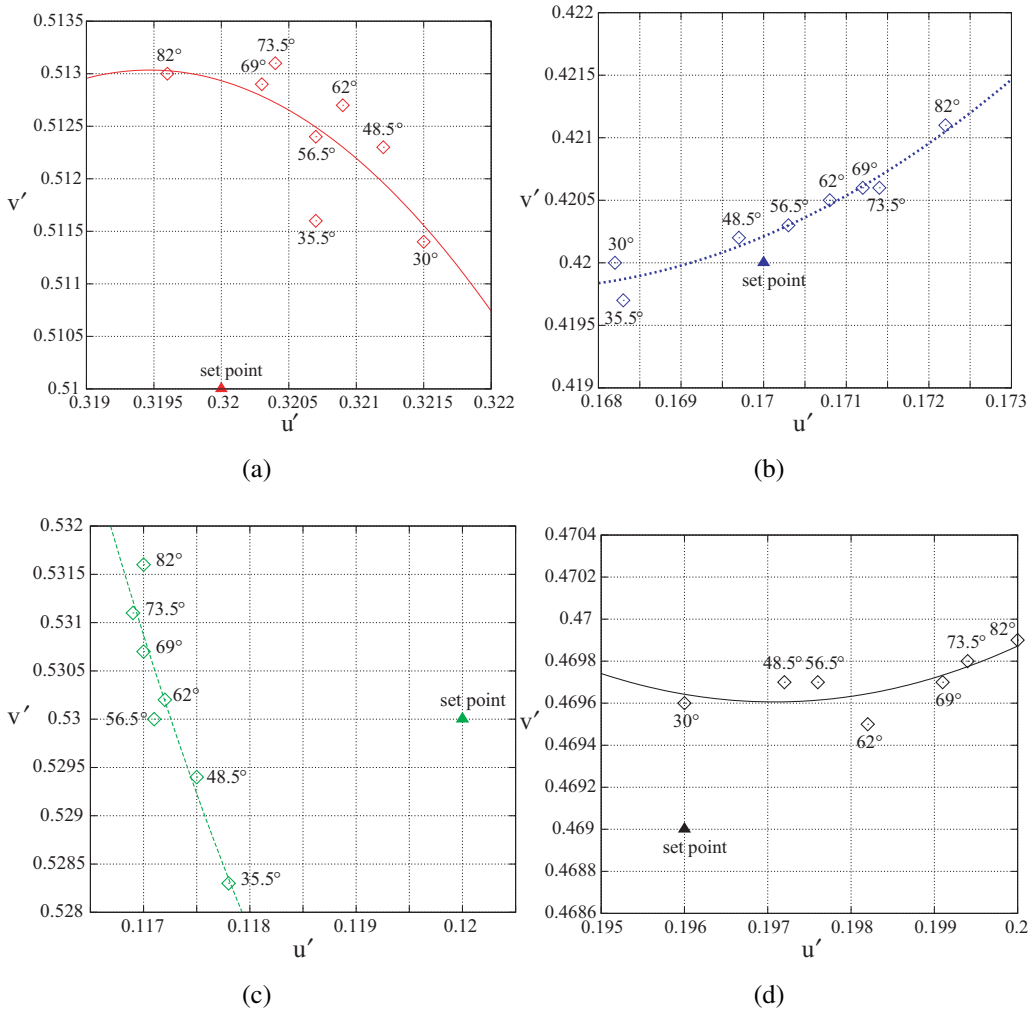

Figure 3.12: Evaluation of output color points, marked as small diamonds, changing with different heat sink temperatures for set-point colors at (a) light red (b) light blue (c) light green and (d) D65 white, marked as small triangles. Lines are least-square-fits of data points using second degree polynomials.

where the current value of the digital temperature $V_{di,\text{current}}$ is taken as the weighted value of the actually measured one $V_{di,\text{measured}}$ and the previously updated one $V_{di,\text{previous}}$, and β is essentially an integration constant which is adjusted to smoothen the averaged waveform. In continuous time, Eq. (3.7) can be written [113] as

$$\frac{dV_{di}(t)}{dt} = \frac{\ln(1-\beta)}{\delta}\left(V_{di}(t) - V_{di,\text{measured}}\right), \tag{3.8}$$

where δ is the time between measurements. Taking expectation of the above

linear equation gives a noise free equation:

$$\frac{d\bar{V}_{di}(t)}{dt} = \frac{\ln(1-\beta)}{\delta}\left(\bar{V}_{di}(t) - \bar{V}_{di,\text{measured}}\right), \tag{3.9}$$

which gives $\bar{V}_{di}(t) - \bar{V}_{di,\text{measured}} = V_o \exp\left(-\frac{t}{\tau}\right)$, where $\tau = -\frac{\delta}{\ln(1-\beta)}$ and V_o is the disturbance amplitude. Here, we use β = 0.05 to give a response time constant of $\tau \approx 0.1$ s as shown in Fig. 3.10.

Then, V_{di} is compared graphically with the measured diode voltages. As illustrated in Fig. 3.9, the waveforms of the heat sink temperature and diode forward voltages, indicates that the temperatures of heat sink, red, blue and green LED junctions are varying differently during transient and converging to different values at steady state depending on the values of duty cycles and the heat sink temperature. Fig. 3.10 shows that the digital temperatures of the red, green and blue LEDs are varying differently even though the heat sink is maintained at a temperature of 25 °C. The digital temperatures shown as points in Fig. 3.10 are sample points taken from the A/D circuitry of the microcontroller. The digital noises are effectively filtered out by Eq. (3.7) giving solid lines in Fig. 3.10 that essentially follow the trends of the noisy points at the expense of a small time delay.

The computer is also connected to a spectroradiometric system from Oceanoptics Inc. to measure the absolute or relative irradiance of LED lights [114] through a USB local bus connection, as shown in Fig. 3.11. Then, SpectraSuite Software calculates tristimulus XYZ, hue $u'v'w'$, and other correlated color parameters from the spectrum distribution. Note that the spectroradiometric system can be easily programmed to automate the measurements. The 18 unknown coefficients in Eq. (3.3) can be calculated from the data obtained from this computer controlled system. The algorithm is as follows. For each duty cycle value equal to 1, 0.8, 0.6 and 0.4, we measure the tristimulus XYZ corresponding to the digital diode forward voltage while the LED heat sink is heated up from room temper-

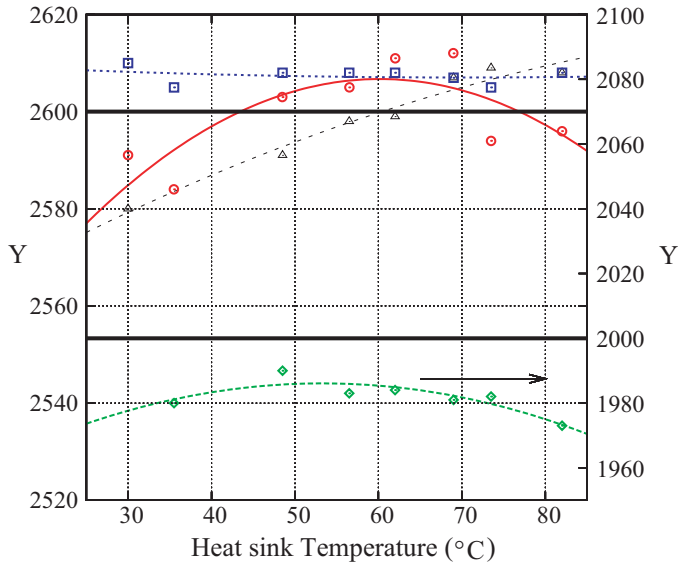

Figure 3.13: Evaluation of output brightness difference in Y value, corresponding to Fig. 3.12. Data points triangles, squares, and circles are for D65 white, light blue and light red respectively with set point at Y = 2600. Data points diamonds are for light green with set point at Y = 2000 and Y-axis at the right. Lines are least-square-fits of data points using second degree polynomials.

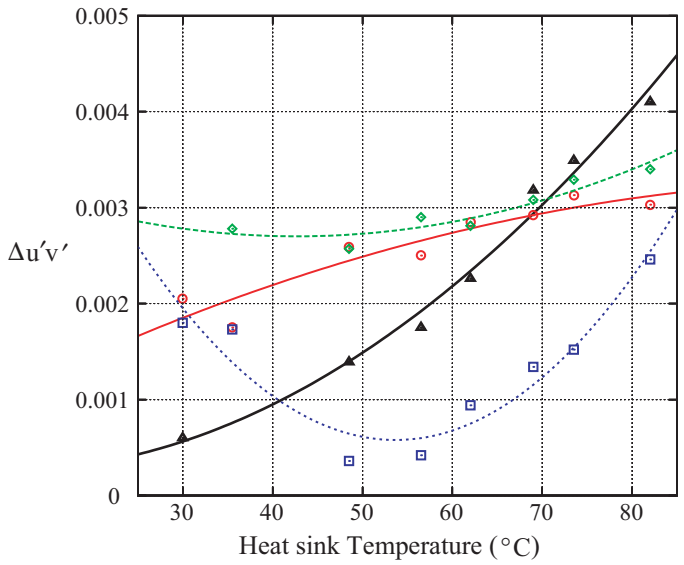

Figure 3.14: Evaluation of output color difference using $\Delta u'v'$, corresponding to Fig. 3.12. Data points triangles, squares, circles, and diamonds are for D65 white, light blue, light red and light green respectively shown in Fig. 3.1. Lines are least-square-fits of data points using second degree polynomials.

ature to about 100 °C. The measurement is done for each of the red, green, blue LEDs. Results are shown earlier in Figs. 3.2(a), (b) and (c).

By curve-fitting in Figs. 3.2(a), (b) and (c), the coefficients can be obtained as

$$\begin{pmatrix} X_{or} \\ Y_{or} \\ Z_{or} \end{pmatrix} = \begin{pmatrix} 2.2421 * V_{dr} - 6832.1 \\ 1.0281 * V_{dr} - 3183.5 \\ 0.0 * V_{dr} - 0.0 \end{pmatrix} \tag{3.10}$$

$$\begin{pmatrix} X_{og} \\ Y_{og} \\ Z_{og} \end{pmatrix} = \begin{pmatrix} 0.020625 * V_{dg} + 818.925 \\ 0.232025 * V_{dg} + 1695.625 \\ 0.039175 * V_{dg} + 96.865 \end{pmatrix} \tag{3.11}$$

$$\begin{pmatrix} X_{ob} \\ Y_{ob} \\ Z_{ob} \end{pmatrix} = \begin{pmatrix} 0.07005 * V_{db} + 618.8 \\ -0.01385 * V_{db} + 590.725 \\ 0.406475 * V_{db} + 3429.75 \end{pmatrix} \tag{3.12}$$

These coefficients are then used for a test run of color accuracy in the computer. If the color accuracy is within tolerance, they will be programmed into the PIC18F1320 for stand-alone real-time control of light colors.

3.5 Evaluation

Four color points are chosen to evaluate the performance of the proposed method. We examine the color and brightness change with temperature at four different points on the color coordinates, namely D65 white, light red, light green and light blue, with corresponding CIE 1976 chromaticity coordinates at (u', v') = (0.196, 0.469), (0.32, 0.51), (0.12, 0.53) and (0.17, 0.42), respectively, as shown in Fig. 3.1. For about 50 °C change in temperature of the heat sink, the position of color point on the CIE 1976 $u'v'$ plane and the brightness in Y value are plotted in Fig. 3.12 and Fig. 3.13 respectively. The maximum color difference is 0.0041 which has been recorded for D65 white, as shown in Fig. 3.14. To show the

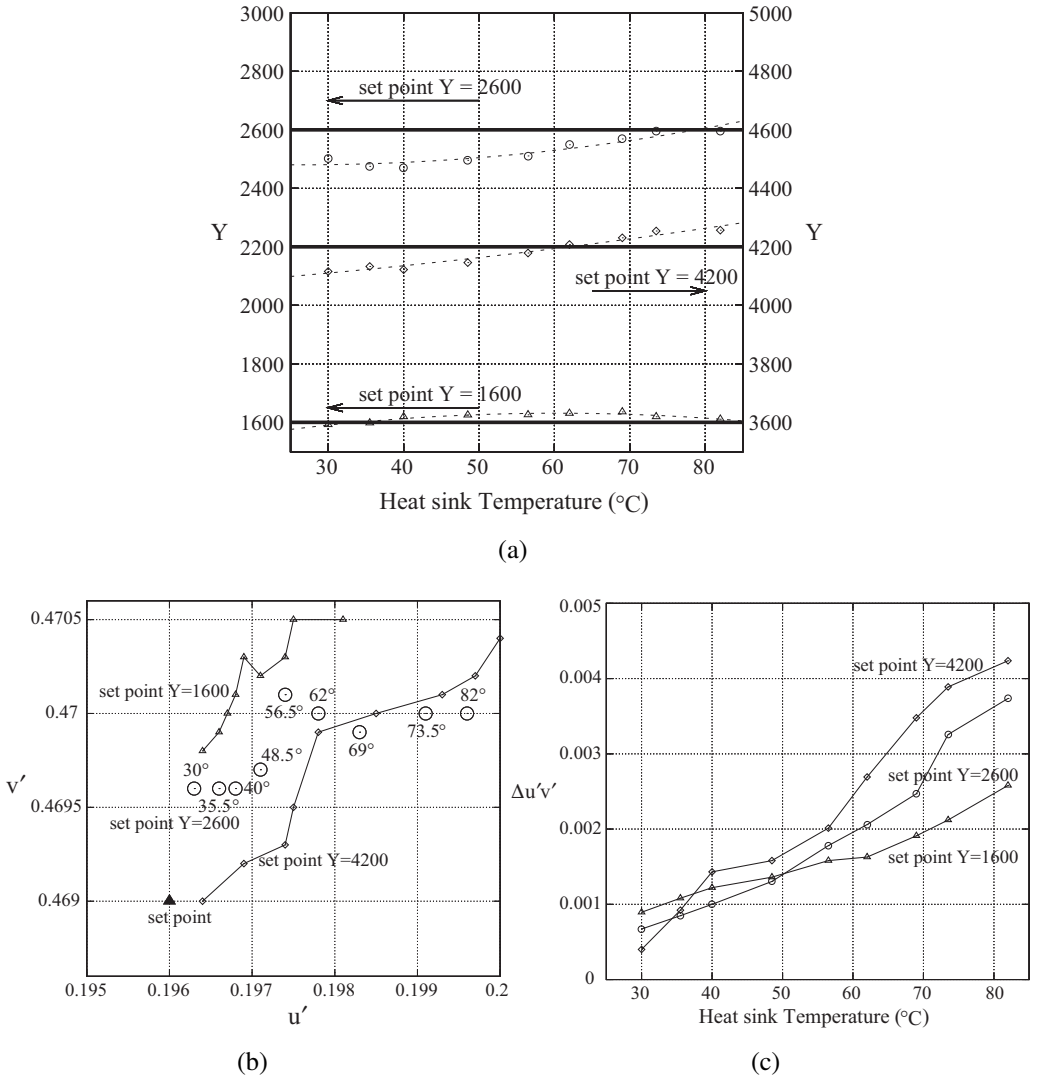

Figure 3.15: Evaluation of (a) output brightness, (b) color coordinate and (c) $\Delta u'v'$ at three set points of D65 white, changing with different heat sink temperatures. Data points shown as triangles, circles and diamonds correspond to set points at Y = 1600, Y = 2600 and Y = 4200, respectively.

effectiveness of the proposed method in dimming operation, the brightness (Y value) and chromaticity coordinates for three brightness values of D65 white have been evaluated and reported in Fig. 3.15 for different heat sink temperatures. The measurement also employs the afore-described spectroradiometric setup under the same condition so that the experimental results are consistent and reliable. The error is mainly due to switching noise and the precision of the duty cycle that can be made very small by using boxcar averaging, digital filtering and a high bit

resolution timer of the micro-controller. Users can simply input the desired color tristimulus values and then the microcontroller system can automatically adjust the duty cycles of RGB LED drivers for stable color light intensity output without the use of any other devices such as sensors.

3.6 Summary

Color control is an important issue in the design and manufacture of LED lighting systems. Due to device variation, aging and sensing nonlinearity, achieving color precision within tolerance for a large number of LEDs is often a difficult task. Measurement of LED turn-on voltage during the on-state of PWM periods has been proposed to stabilize the LED light color. The implementation technique is outlined and verified by some experimental data. The technique can control the color effectively, and can also dramatically reduce the complexity and eliminate the need for using expensive feedback systems involving light sensors. In the next chapter, electronic ballasts will be developed for independent control of brightness for LED light sources.

Chapter 4

Electronic Ballasts for Multiple LED Lamps with Independent Brightness Control

4.1 Introduction

Due to nonlinearity between the lumen output and the driving current, LEDs are normally driven by a constant current source controlled via pulse width modulation for the precise control of brightness and color. Therefore, in the RGB mixing color system, the red, green or blue LED lamps may be driven by three independent switching mode power converters respectively to achieve the instant color changing ability and keep the desired color stabilization compensating the effect of junction temperature as described in Chapter 3. Furthermore, for device variation, at most one current driver per LED may be needed to produce the desired color and brightness of light. Usually, a small number of LED lamps having thermal-electrical-optical properties within tolerance are selected and driven together for the reduction of cost and volume.

Driving several LED light engines independently from an offline power source poses technical challenge in many aspects of the power converter design. High power factor and low input current harmonics have become the mandatory design criteria for switching power supplies. A typical design using the "classical" two-stage PFC circuit is shown in Fig. 4.1 [115]. The specific challenges in using this circuit are described as follows. Firstly, LED lamps have a lifetime of about 100,000 hours while conventional PFC power converters employing high-voltage electrolytic capacitors have much shorter lifetimes of about 5,000 hours [96]. These high-voltage electrolytic capacitors are utilized in most single-stage PFC circuits [116, 117]. Secondly, to generate light with the desired color and brightness, three stages are effectively needed, which limit the overall efficiency. Thirdly, a high turns-ratio transformer is required to provide a low-voltage level at the secondary suitable for an LED controller. This, however, is accompanied by a significant leakage inductance on the primary side of the transformer, causing a dramatic increase in the power loss due to passive snubberings, thermal stress and device stress, and making the lifetime of the converter much shorter than that of LED lamps.

With consideration of these issues, an electronic ballast for multiple LED lamps is proposed in this thesis to overcome the above limitations. The LED ballast is essentially a dual non-cascading structure. The first-stage non-cascading structure is an isolated current-fed PFC pre-regulator. In the proposed design, the short-lifetime high-voltage storage capacitor at the primary is replaced by a long-lifetime low-voltage capacitor at the secondary, thus extending the overall system lifetime. Furthermore, the high-voltage stress on the main switch, which is typical in current-fed converters, is reduced substantially by appropriately exploiting the transformer leakage inductance. The design uses two secondary transformer windings and an LED current driver to form a second non-cascading structure to improve efficiency. Multiple non-cascading structures can be used for LED lamps for the instant independent brightness control. The analysis and design of the PFC pre-regulator will be focused in this chapter and the details of the

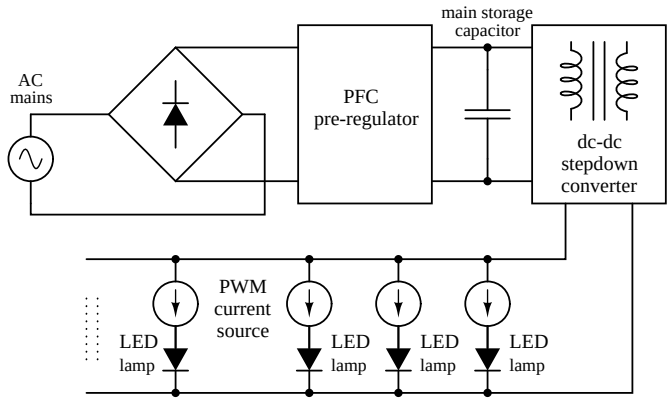

Figure 4.1: Classical design of LED power supply consisting of a two-stage PFC voltage regulator driving point-of-load current regulated LED lamps.

non-cascading structure will be described in the following chapter.

This chapter is organized as follows. Section 4.2 gives an overview of limitations of the conventional PFC power converter design when using power transformers with large parasitic leakage inductance. The new PFC current regulator is given in Section 4.3. Analysis and implementation of the pre-regulator are given in Section 4.4. The performance of the proposed regulator is evaluated in Section 4.5, and a summary is given in Section 4.6.

4.2 Limitations of Conventional PFC Regulator in Converting Energy Through High Leakage Inductance Transformer

Transformer isolation for a PFC regulator is mostly implemented using flyback or forward topologies, and occasionally designed with the resonant topology [118]. Resonant topology can easily make use of the transformer leakage inductance to form a resonant tank in transforming energy from the primary to the secondary [119]. Moreover, despite such an advantage, the practical implementation often uses a cascading structure as shown in Fig. 4.1, that requires an

expensive high-voltage storage capacitor on the primary [118, 120].

The conventional PWM-type transformer isolation design for PFC regulator rarely considers the transformer leakage inductance [115, 121–123]. The relatively large leakage inductance of a high turns-ratio transformer may render the passive snubber circuit inadequate in reducing either voltage or current stress, reducing the operational lifetime of the main switches.

In the following section, we will introduce a new PFC pre-regulator which allows the use of a non-cascading structure and does not require a high-voltage storage capacitor on the primary side of the PFC pre-regulator.

4.3 PFC Current Regulator for LED Lamps

We show in Fig. 4.2 a boost input stage operating in discontinuous conduction mode (DCM) for automatic power factor correction for low-power LED lamp applications. The input line filter including L_f and C_f is used to filter the high switching frequency current harmonics. The main switch S_1 is switching at a fixed frequency f_S with the duty cycle d, and controls the amount of input power to the regulator. We use a transformer model of L_p and L_m for the analysis of the new pre-regulator. An equivalent rectifying load consisting of a diode bridge and the output loading C_O and R_O reflected on the primary has been used for simplicity.

The output current i_D of the boost inductor in Fig. 4.2 is pulsating and cannot be connected directly to the legs of an isolation transformer with large leakage inductance L_p unless its current i_p has been equalized to that of i_D. An alternative current drive must be applied to the transformer to maintain zero volt-second within a period, or else the current of the mutual inductance L_m will keep increasing and be saturated easily. An easy solution is to connect i_D to a half-bridge circuit with small resonant bridging capacitors C_p absorbing the dif-

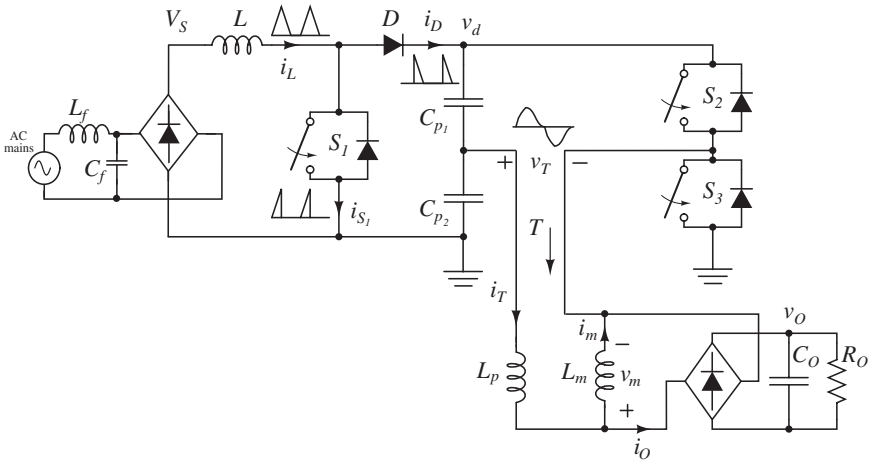

Figure 4.2: Simplified circuit of the proposed PFC pre-regulator with an equivalent transformer secondary load.

ference of currents of the two inductors, and clamp the voltages they connected to an acceptable level. The two half-bridge switches S_2 and S_3 split and distribute i_D alternately in reverse order to the two legs of the primary of transformer T which is shown as i_T in Fig. 4.2. The two switches of the half-bridge circuit is driven non-overlappingly and alternately at half the switching frequency $f_S/2$ of the boost converter for a fixed duty cycle. A sufficient dead-time of the two switches will allow current of the leakage and large mutual inductances of the transformer to turn on one of the two body diodes of the switches, and will assure later zero-voltage-switching (ZVS) of either S_2 or S_3. In this way, energy is transferred directly from the boost inductor to the transformer secondaries with little loss and storage. Although the large transformer mutual inductance helps soft switching of S_2 and S_3, it does not intervene much the power flow from the primary to the secondary. Its effect will be ignored in our estimation of power transfer function in the next section.

Two secondary output windings of the transformer per LED are used in the non-cascading output configuration shown in Fig. 4.3. One of the outputs is connected without processing in series with the other output which is current regulated by a PWM buck converter to drive an LED. Additional identical secondary circuits or buck converters can be built to drive more LEDs independently.

The energy from the output without processing can directly contribute to drive the LED with an unity power efficiency. The analysis and design of this non-cascading output configuration is presented in the next chapter.

In the next section, the steady-state waveforms will be studied for calculating suitable component values of the LED lamps PFC pre-regulator.

4.4 Analysis and Implementation of the New PFC Pre-Regulator

4.4.1 Steady-State Waveforms

Fig. 4.4 gives the typical waveforms of voltages and currents of the power converter. The corresponding current flow diagrams for various states are given in Figs. 4.5 and 4.6. The boost converter is driven by gate drive v_{g1} while the two half-bridge switches are driven by the two non-overlapping gate drives v_{g2} and v_{g3}. As the waveforms of the half-bridge circuit are half-wave symmetrical, we can simply limit our consideration to states 2 and 3. Similar analysis can easily be applied on states 4 and 1. The operation of the converter is explained as follows:

- At the beginning of state 2, S_1 turns on. Inductor current i_L starts to increase as shown in Fig. 4.5 (a). Diode D is reverse biased and isolated from the half-bridge converter.

- At the same time, S_2 turns off. Inductor current i_p starts to increase by a voltage difference of $v_{C_{p2}} - v_O$ as described by Fig. 4.6 (b), charging up the capacitor C_{p2} and delivering power in reverse direction to the output through the output diode rectifying bridge. As a result the voltage v_m acted on L_m reverses polarity with the same voltage amplitude of v_O, its current starts to ramp up at a constant rate.

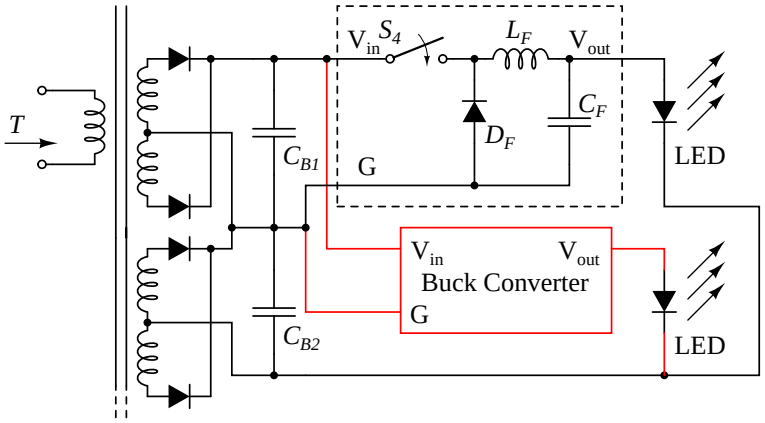

Figure 4.3: Transformer secondary side equivalent load of T in Fig. 4.2.

- After a short dead-time, S_3 turns on, continuing to charge up the capacitor C_{p2} and delivering power to the output.
- Inductor current i_p starts reversing its polarity and marks the end of state 2, as indicated in Fig. 4.6 (c).
- L_p resonates with C_{p2}, discharging C_{p2} and delivering power to the output.
- S_1 turns off. Inductor current i_L charges up both C_{p1} and C_{p2}, boosting up the resonant amplitudes of capacitor voltage C_{p2} and inductor current i_p.
- i_p resonates to its peak and decreases sinusoidally until its magnitude equals the ramping magnitude of i_m, i.e., $i_p \approx i_m$ and $i_o = i_p - i_m \approx 0$. Inductors L_p and L_m combine together as a single inductor until the end of state 3.
- During both states 2 and 3, the output current is given by $i_o = i_p - i_m \geq 0$.
- The above sequences repeat with S_2, C_{p2} replaced by S_3, C_{p1}, respectively.

These high-frequency switching waveforms vary with the much slower frequency varying the line voltage within a rectified line cycle. Both quantities at these two different time resolutions are important for calculating the converter dynamics. For consistency, for any state variable x, we will denote by $x(t)$ the detailed

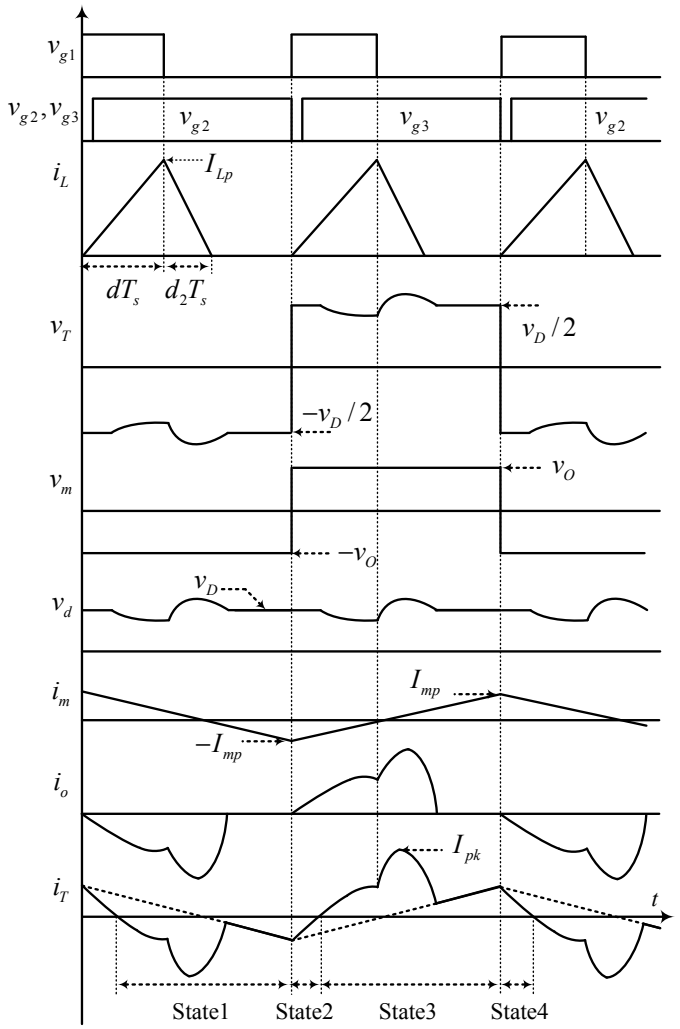

Figure 4.4: Simplified waveforms of i_L for the boost converter and i_T $(= i_p)$ for the half-bridge converter. i_m and v_m are current and voltage of the mutual inductor L_m respectively.

waveform, and by x the averaged values of $x(t)$ to accommodate any change at the line frequency.

The detailed waveforms of $v_{C_{p1}}(t)$, $v_{C_{p2}}(t)$ and $i_D(t)$, $i_p(t)$ determine the voltage and current stresses of power switches S_1, S_2, and S_3. We consider $t = 0$

and $t = T_S$ as the start of state 2 and by the end of state 3, respectively. We have

$$L_p \frac{\mathrm{d}i_p(t)}{\mathrm{d}t} = v_{C_{p2}}(t) - v_O, \tag{4.1}$$

$$C_p \frac{\mathrm{d}v_{C_{p2}}(t)}{\mathrm{d}t} = i_D(t) - i_p(t), \tag{4.2}$$

$$C_p \frac{\mathrm{d}v_{C_{p1}}(t)}{\mathrm{d}t} = i_D(t), \text{ and} \tag{4.3}$$

$$L_m \frac{\mathrm{d}i_m(t)}{\mathrm{d}t} = v_O, \tag{4.4}$$

which satisfy the boundary conditions $i_p(0) = 0$, $i_p(T_1) = i_m(T_1)$, $v_{C_{p1}}(0) = V_{C10}$, $v_{C_{p2}}(0) = V_{C20}$, $v_{C_{p1}}(dT_S) = V_{C1d}$, $v_{C_{p2}}(dT_S) = V_{C2d}$, $i_m(0) = -I_{mp}$ and $i_m(T_S) = I_{mp}$ within states 2 and 3 for a duration of T_S $(= 1/f_S)$. From Fig. 4.2 or 4.4, we have

$$i_D(t) = \begin{cases} 0 & 0 \le t < dT_S \\ \frac{v_S d}{L d_2}[(d+d_2)T_S - t] & dT_S \le t < (d+d_2)T_S \\ 0 & (d+d_2)T_S \le t < T_S \end{cases} \tag{4.5}$$

Integrating (4.1) to (4.4), we obtain

$$i_p(t) = \begin{cases} \frac{V_{C20}-v_O}{Z_r}\sin(\omega_r t) & 0 \le t < dT_S \\ \frac{V_{C20}-v_O}{Z_r}\sin(\omega_r t) & \\ +\frac{v_S dT_S}{L}\left[1-\cos\omega_r(t-dT_S)\right] & \\ +\frac{V_{C1d}+V_{C2d}-v_S}{L}\left[\frac{\sin\omega_r(t-dT_S)}{\omega_r}\right. & \\ \left.-(t-dT_S)\right] & dT_S \le t < T_1 \\ i_m(t) & T_1 \le t < T_S \end{cases} \tag{4.6}$$

$$v_{C_{p2}}(t) = \begin{cases} v_O + (V_{C20} - v_O)\cos(\omega_r t) & 0 \le t < dT_S \\ v_O + (V_{C20} - v_O)\cos(\omega_r t) & \\ + \frac{v_S dT_S Z_r}{L} \sin \omega_r (t - dT_S) & \\ + \frac{L_p (V_{C1d} + V_{C2d} - v_S)}{L} [& \\ \cos \omega_r (t - dT_S) - 1] & dT_S \le t < T_1 \\ v_{C_{p2}}(T_1) - \frac{v_O}{2 L_m C_p} & \\ (t - T_1)(t - T_s + T_1) & T_1 \le t < T_S \end{cases} \tag{4.7}$$

$$v_{C_{p1}}(t) = \begin{cases} V_{C10} & 0 \le t < dT_S \\ V_{C10} + \left[\frac{v_S dT_S (t - dT_S)}{C_p L} \right. & dT_S \le t < \\ \left. - \frac{(V_{C10} + V_{C20} - v_S)(t - dT_S)^2}{2 C_p L} \right] & (d + d_2) T_S \\ \frac{v_S^2 d^2 T_S^2}{2 C_p L (V_{C10} + V_{C20} - v_S)} & (d + d_2) T_S \\ & \le t < T_S \end{cases} \tag{4.8}$$

and

$$i_m(t) = \frac{v_O}{L_m} t - I_{mp}, \tag{4.9}$$

$$\tag{4.10}$$

where

$$I_{mp} = \frac{v_O T_S}{2L_m}, \tag{4.11}$$

$$\omega_r = \sqrt{\frac{1}{L_p C_p}}, \text{ and} \tag{4.12}$$

$$Z_r = \sqrt{\frac{L_p}{C_p}}. \tag{4.13}$$

The current stresses of S_1 and S_2 (or S_3) are given by $\max(i_D(t))$ and $\max(i_p(t))$, respectively. They all experience the same voltage stress $\max(v_D(t))$, and are calculated as follows.

$$\max(i_D(t)) = \frac{v_S}{L} d T_S, \tag{4.14}$$

$$\max(i_p(t)) = i_p(t_{m1}), \text{ and} \tag{4.15}$$

$$\begin{aligned} \max(v_D(t)) &= \max\left(v_{C_{p1}}(t) + v_{C_{p2}}(t)\right) \\ &\leq \max(v_{C_{p1}}(t)) + \max(v_{C_{p2}}(t)) \\ &\leq v_{C_{p1}}(t_{m2}) + v_{C_{p2}}\left((d+d_2)T_S\right), \end{aligned} \tag{4.16}$$

where

$$\begin{aligned} t_{m1} = {} & d T_S + \frac{\pi}{\omega_r} \\ & - \frac{1}{\omega_r} \sin^{-1}\left(\frac{2 V_S d T_S \omega_r (V_{C1d} + V_{C2d} - V_S)}{V_S^2 d^2 T_S^2 \omega_r^2 + (V_{C1d} + V_{C2d} - V_S)^2}\right) \end{aligned} \tag{4.17}$$

$$t_{m2} = d T_S + \frac{1}{\omega_r} \tan^{-1}\left(\frac{L_p (V_{C1d} + V_{C2d} - V_S)}{V_S d T_S Z_r}\right) \tag{4.18}$$

and $t_{m1}, t_{m2} \in [dT_S, T_1)$.

Basically, all the detailed waveforms depend on their corresponding initial boundary values which can be approximated using their averaged values. As a consequence, a full analysis of the steady-state solution using state-space method may be prohibitively complicated. We will use the following method of state-space averaging to estimate the system dynamics near the line frequency.

4.4.2 Basic Assumptions for State-space Averaging

We assume that

1. The switching frequency f_S is much higher than the line frequency f_l of the line input voltage v_S,
2. The switching-period-averaged capacitor voltages are used for calculating dynamics at a much lower line frequency,
3. The discontinuous conduction current i_L of the input inductor L provides power factor correction,
4. The converter is lossless,
5. The mutual inductance L_m is much larger than the leakage inductance L_p, and its effect on output current can be ignored, and
6. The secondary leakage inductance L_s is much smaller than L_p, and its effect can be ignored.

Such assumptions allow analyzing converter dynamics at the switching frequency and the line frequency separately. They also allow analyzing the boost stage and half-bridge stage separately. Figs. 4.5 and 4.6 show the operation states of the separated boost and half-bridge converters, respectively.

(a) State duration dT_S. Switch S_1 turns on. i_L starts to increase. Diode D is reverse biased and turned off.

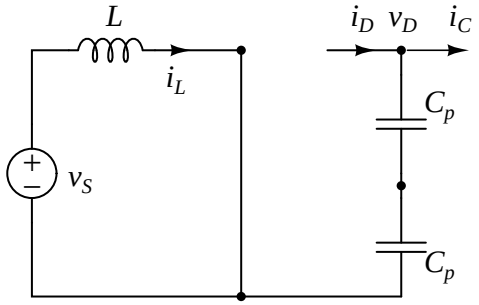

(b) State duration d_2T_S. Switch S_1 turns off. i_L forces diode D to turn on and starts to decrease.

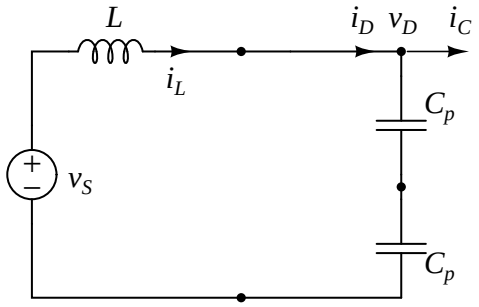

(c) State duration $(1 - d - d_2)T_S$. i_L just decrease to zero, turning diode D off.

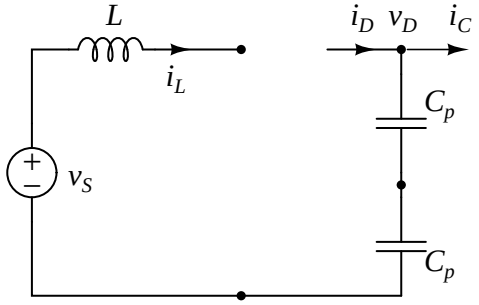

Figure 4.5: Three states of the discontinuous inductor current mode operation of the input boost converter, where i_C is the capacitor discharging current.

4.4.3 Averaging Over Converter Switching Frequency

Using state-space averaging, all instantaneous voltages and currents calculated in the last subsection have to be averaged and represented by the their averaged values within half of a period, i.e., one T_S. However, we are interested only in their averaged values and will ignore their detailed waveforms. Therefore, the instantaneous current $i_p(t)$ of L_p and the instantaneous voltage $v_{C_{p2}}(t)$ of C_{p2} in

State 1: Just after the current i_{T4} in (d) decrease to zero and reverse its current direction to enter this state.

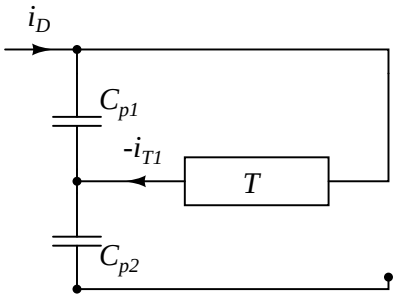

State 2: Just after S_2 turns off, the leakage inductance forces the body diode of S_3 to conduct. After a short dead time, S_3 is turned on at zero voltage.

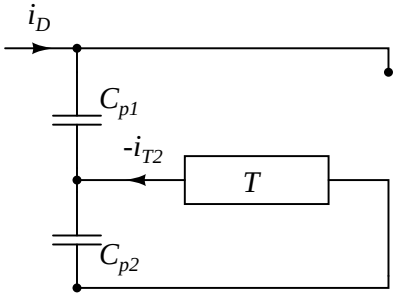

State 3: Just after the current i_{T2} in (b) decreases to zero and reverses its current direction.

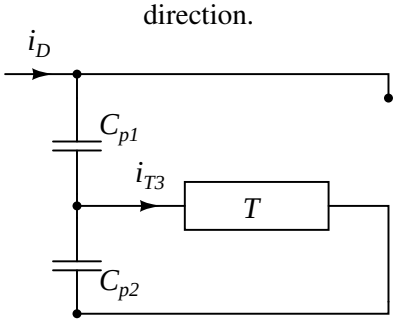

State 4: Just after S_3 turns off, the leakage inductance forces the body diode of S_2 to conduct. After a short dead time, S_2 is turned on at zero voltage.

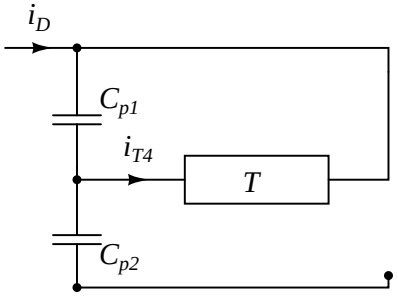

Figure 4.6: Four major states of the half-bridge converter for a period of $2T_S$. The arrows indicate actual current direction and $C_{p1} = C_{p2} = C_p$.

the resonant tank shown in Fig. 4.6 are approximated as

$$v_{C_{p2}}(t) - v_O = L_p \frac{di_p(t)}{dt}, \text{ and} \tag{4.19}$$

$$C_p \frac{d(v_{C_{p2}}(t))}{dt} = -i_p(t), \tag{4.20}$$

where $i_p(0) = 0$ and $v_{C_{p2}}(0) = v_D/2$ are the initial values at the beginning of half the resonant cycle. Integrating Eq. (4.19) and Eq. (4.20), and considering only the positive portion of $i_p(t)$, we have

$$i_p(t) = \frac{v_D/2 - v_O}{Z_r} \sin(\omega_r t), \text{ and} \tag{4.21}$$

$$v_{C_{p2}}(t) = v_O + (v_D/2 - v_O)\cos(\omega_r t), \tag{4.22}$$

for $0 < t < \frac{\pi}{\omega_r}$ and

$$i_p(t) = 0, \text{ and} \tag{4.23}$$

$$v_{C_{p2}}(t) = v_O, \tag{4.24}$$

for $\frac{\pi}{\omega_r} \leq t < T_S$.

It can be observed from Eq. (4.21) to Eq. (4.24) that

$$\frac{1}{T_S}\int_0^{T_S} i_p(t)dt = \frac{2}{\pi}\frac{v_D/2 - v_O}{Z_r} \tag{4.25}$$

It is expected that $v_{C_{p2}}(t)$ will be charged up back to $v_D/2$ by the end of the other half period. The averaged output current and capacitor discharging current over half a switching period is therefore given as

$$i_O = \frac{2}{\pi}\frac{v_D/2 - v_O}{Z_r}, \text{ and} \tag{4.26}$$

$$i_C = \frac{v_O}{v_D} i_O. \tag{4.27}$$

Similarly, from Figs. 4.4 and 4.5, the peak current of L is obtained as

$$I_{Lp} = \frac{v_S}{L} dT_S, \text{ and} \tag{4.28}$$

$$I_{Lp} = \frac{v_D - v_S}{L} d_2 T_S. \tag{4.29}$$

Referring to Fig. 4.4 and using Eq. (4.28) and Eq. (4.29), the duty cycles and averaged currents i_S and i_D of a switching period are calculated as

$$d + d_2 = \frac{v_D}{v_D - v_S} d, \tag{4.30}$$

$$i_S = \frac{d^2 T_S}{2L} \frac{v_D v_S}{v_D - v_S}, \text{ and} \tag{4.31}$$

$$i_D = \frac{d^2 T_S}{2L} \frac{v_S^2}{v_D - v_S}. \tag{4.32}$$

4.4.4 Small-Signal Response of the Converter

The control-to-output response will be important for the design of the closed loop system. Eliminating v_D from (4.26) and (4.31) and using the lossless approximation of $v_S i_S = v_O i_O = v_O^2 / Z_O$, we arrive at

$$\frac{v_O^2 \left(2v_O - v_S + \frac{\pi v_O Z_r}{Z_O}\right)}{Z_O} - \frac{d^2 T_S v_S^2 \left(2v_O + \frac{\pi v_O Z_r}{Z_O}\right)}{2L} = 0. \tag{4.33}$$

Perturbing (4.33) using $d \rightarrow D + \hat{d}$ and $v_O \rightarrow V_O + \hat{v}$ and linearizing, the control-to-output small signal response is given as

$$\frac{\hat{v}}{\hat{d}} = \frac{2DT_S V_O V_S^2 Z_O Z}{2LV_O(3V_O Z - 2V_S Z_O) - D^2 T_S V_S Z_O Z}, \tag{4.34}$$

where

$$Z = 2Z_O + \pi Z_r \tag{4.35}$$

Equation (4.34) is approximately a single-pole system which simplifies the design of the closed loop system. Other small-signal responses can be readily derived using the state-space averaging method and are omitted here.

4.4.5 Dynamics Near Line Frequency

The averaged state variables have been calculated in the last subsection. In this subsection, the dynamics of the averaged state variables varying near the line frequency will be determined. The input voltage is rectified as a positive half-sine, i.e.,

$$v_S = V_S \left|\sin 2\pi f_l t\right| . \tag{4.36}$$

From (4.31), we have

$$i_S = \frac{d^2 T_S}{2L} \frac{V_S \left|\sin 2\pi f_l t\right|}{1 - v_S/v_D}, \tag{4.37}$$

which is approximated as

$$i_S = I_S \left|\sin 2\pi f_l t\right| , \tag{4.38}$$

where the effective I_S will be determined after v_D is obtained later in this subsection. Based on assumption 4 and the fact that the two capacitors C_p have relatively small intermediate storage compared to the output capacitor C_O, the instantaneous power balance at the line frequency gives

$$v_O i_O = v_S i_S = \frac{V_S I_S}{2} \left(1 - \cos 4\pi f_l t\right) . \tag{4.39}$$

The output voltage can be calculated using

$$\frac{\mathrm{d}v_O}{\mathrm{d}t} = \frac{i_O}{C_O} - \frac{v_O}{R_O C_O}. \tag{4.40}$$

Multiplying both side of (4.40) by v_O, using (4.39), and rearranging, we have

$$\begin{aligned} \frac{1}{2}\frac{\mathrm{d}v_O^2}{\mathrm{d}t} + \frac{v_O^2}{R_O C_O} &= \frac{i_O v_O}{C_O} \\ &= \frac{V_S I_S}{2C_O}\left(1 - \cos 4\pi f_l t\right). \end{aligned} \tag{4.41}$$

Integrating (4.41), the steady-state output voltage is given by

$$\begin{aligned} v_O^2 &= \frac{V_S I_S R_O}{2}\left(1 - \frac{\cos 4\pi f_l t + 2\pi f_l R_O C_O \sin 4\pi f_l t}{1 + (2\pi f_l R_O C_O)^2}\right) \\ &\approx \frac{V_S I_S R_O}{2}\left(1 - \frac{\sin 4\pi f_l t}{2\pi f_l R_O C_O}\right) \quad \text{if } 2\pi f_l R_O C_O \gg 1. \end{aligned} \tag{4.42}$$

Basically, the converter will operate at a fundamental frequency of $2f_l$ according to (4.39). We will approximate every variable up to the fundamental frequency component of the form

$$x_A \approx X_{A0} + X_{A1}\sin(4\pi f_l t + \theta_A), \tag{4.43}$$

where X_{A0}, X_{A1}, and θ_A are the DC value, the magnitude and phase of the fundamental frequency component of x_A, respectively. Using approximation (4.43), (4.42) becomes

$$v_O = V_{O0} - V_{O1}\sin(4\pi f_l t), \tag{4.44}$$

where

$$V_{O0} = \sqrt{\frac{V_S I_S R_O}{2}}, \text{ and} \tag{4.45}$$

$$V_{O1} = \frac{V_{O0}}{4\pi f_l R_O C_O}. \tag{4.46}$$

From (4.39) and (4.44), the output current is determined as

$$i_O = I_{O0} + I_{O1} \sin\left(4\pi f_l t - \frac{\pi}{2}\right), \tag{4.47}$$

where

$$I_{O0} = \frac{V_{O0}}{R_O}, \text{ and} \tag{4.48}$$

$$I_{O1} = I_{O0}. \tag{4.49}$$

The output voltage and current shown in (4.44) and (4.47) can be determined if the input power is known. However, the input power also depends on the output voltage v_D of the boost stage governed by (4.26). Equation (4.26) can be rewritten as

$$g \equiv i_O - \left(\frac{2}{\pi}\frac{v_D/2 - v_O}{Z_r}\right) = 0. \tag{4.50}$$

Substituting $v_D = V_{D0} + V_{D1}\sin(4\pi f_l t + \theta_D)$ into (4.50), the following equalities from harmonic balance hold:

$$\begin{cases} \int_0^{\frac{1}{2f_l}} g(t)\,\mathrm{d}t = 0 \\ \int_0^{\frac{1}{2f_l}} \sin(4\pi f_l t) g(t)\,\mathrm{d}t = 0 \\ \int_0^{\frac{1}{2f_l}} \cos(4\pi f_l t) g(t)\,\mathrm{d}t = 0 \end{cases} \tag{4.51}$$

Solving (4.51) for $v_D \approx V_{D0} + V_{D1}\sin(4\pi f_l t - \theta_D)$ gives four possible solutions, of which only one satisfies $V_{D0} > V_{O0}$, i.e.,

$$V_{D0} = V_{O0}(2 + \frac{K_3\pi}{R_O}) \tag{4.52}$$

$$V_{D1} = V_{O0}\sqrt{K_4^2 + K_5^2} \tag{4.53}$$

$$\theta_D = \pi + \tan^{-1}\frac{K_4}{K_5} \tag{4.54}$$

where

$$K_1 = \frac{T_S R_O}{2L} \tag{4.55}$$

$$K_2 = \frac{1}{4\pi f_l R_O C_O} \tag{4.56}$$

$$K_3 = \sqrt{\frac{L_p}{C_p}} \tag{4.57}$$

$$K_4 = 2K_2 \tag{4.58}$$

$$K_5 = -\frac{K_3 \pi}{R_O} \tag{4.59}$$

Now, we can estimate the effective value I_S of (4.38) from (4.37). The input power is calculated by multiplying (4.36) by (4.37) as

$$v_S i_S = \frac{d^2 T_S}{2L} V_S^2 \frac{1}{1 - v_S/v_D} \sin^2 2\pi f_l t, \tag{4.60}$$

where the term $\frac{1}{1-v_S/v_D}$ is highly nonlinear and the harmonic components are difficult to obtain in analytical forms. We will adopt an empirical approximation as follows:

$$\frac{1}{1 - v_S/v_D} \approx 1 + \frac{\sin 4\pi f_l t}{V_{D0}/V_S + V_{D1}/V_S - 1}, \tag{4.61}$$

which approximates the waveform using the DC and fundamental components. Substituting (4.61) into (4.60) and averaging over $T_l = \frac{1}{2f_l}$, the averaged input power is

$$\begin{aligned} \frac{V_S I_S}{2} &= \frac{1}{T_l} \int_0^{T_l} v_S i_S \, \mathrm{d}t \\ &= \frac{d^2 T_S V_S^2}{2L} \left(\frac{1}{2} + \frac{4}{3\pi} \frac{1}{(V_{D0} + V_{D1})/V_S - 1} \right). \end{aligned} \tag{4.62}$$

Hence, the equivalent current magnitude is given as

$$I_S = \frac{d^2 T_S V_S}{L} \left(\frac{1}{2} + \frac{4}{3\pi} \frac{1}{(V_{D0} + V_{D1})/V_S - 1} \right). \tag{4.63}$$

The averaged output power is approximated using (4.42) and (4.46) as

$$\frac{V_{O0}^2 + \frac{V_{O1}^2}{2}}{R_O} = V_{O0}^2 \frac{1 + \frac{K_2^2}{2}}{R_O}. \tag{4.64}$$

Equalizing (4.62) and (4.64), we get

$$V_{O0}^2 - K_6 V_S^2 \left(\frac{1}{2} + \frac{4}{3\pi} \frac{V_S}{K_7 V_{O0} - 1} \right) = 0, \tag{4.65}$$

where

$$K_6 = d^2 \frac{2K_1}{2 + K_2^2}, \text{ and} \tag{4.66}$$

$$K_7 = 2 + \frac{2K_3}{R_O} + \sqrt{K_4^2 + K_5^2}. \tag{4.67}$$

A real root of (4.65) is calculated as

$$V_{O0} = V_S \left(\frac{1}{3K_7} + (4\pi)^{\frac{1}{3}} \frac{3K_7^2 K_6 + 2}{6K_7 K_8} + \left(\frac{2}{\pi} \right)^{\frac{1}{3}} \frac{K_8}{6K_7} \right), \tag{4.68}$$

where K_8 is given in (4.69).

$$\begin{aligned} K_8 = (&18(4-\pi)K_7^2 K_6 + 4\pi \\ &+ 3\sqrt{2}\sqrt{K_7^2 K_6 \left[4(8-3\pi)\pi + 12K_7^2 K_6(24 - 12\pi + \pi^2) - 3K_7^4 K_6^2 \pi^2\right]})^{\frac{1}{3}}, \end{aligned} \tag{4.69}$$

The calculation of the steady-state solutions is summarized as follows. Given circuit parameters K_1 in (4.55), K_2 in (4.56), d and K_3 in (4.57), V_{O0} can be calculated using (4.68), V_{O1} using (4.46), V_{D0} using (4.52), and V_{D1} using (4.53).

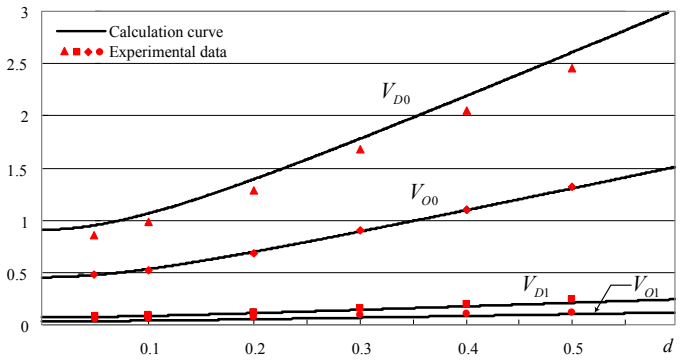

Figure 4.7: Comparison of the calculated and experimental values of $\frac{V_{O0}}{V_S}$, $\frac{V_{O1}}{V_S}$, $\frac{V_{D0}}{V_S}$ and $\frac{V_{D1}}{V_S}$.

4.5 Experimental Evaluation

A prototype of the proposed PFC pre-regulator has been built for driving LED lamps having a total power up to 100 W. Using the result of the last section, we arrive at the components and parameter values shown in Table 4.1.

The details are as follows. With the maximum line input voltage being $240\sqrt{2}$ = 340 V, take V_{D0} = 400 V to ensure the proper operation of the boost input stage. The transformer turns ratio is estimated from (4.52) as $V_{D0} \approx 2V_{O0}$, which gives n = 16.5 for a secondary output voltage of 12 V. The average power for a line cycle is given as $P = \frac{V_S I_S}{2}$. Rearranging gives $I_S = \frac{2P}{V_S}$. Substituting $2I_S = I_{Lp}$ into (4.28) gives $L = \frac{V_S^2 d}{4 f_S P}$. To ensure DCM operation, $d_{max}(v_S) \leq d_{crit}(v_S) = 1 - \frac{v_S}{v_D}$ from (4.30). Hence, $d_{crit}(100\sqrt{2})$ = 0.646. Choose d_{max} $(100\sqrt{2})$ = 0.5. Consequently, $L = \frac{V_S^2 d_{max}(100\sqrt{2})}{4 f_S P}$ = 250 μH. This inductor value can maintain DCM operation and provides the required output power at $d_{max}(240\sqrt{2})$ = 0.087 $\leq$ $d_{crit}(240\sqrt{2})$ = 0.151. A step-down transformer with turns ratio given in Table 4.1 is constructed. The leakage inductance at the primary is measured as L_p = 35 μH. C_p is chosen such that it resonates with L_p with a half period shorter than $(1 - d_{max})T_S$, minimizing the energy stored in L_p before the start of next state, thus minimizing the circulating cur-

Table 4.1: Components and parameter values used in experiments.

Components/parameters	Values
L	253 μH
C_p	69 nF
L_p	35 μH
L_m	1.85 mH
turn ratio n:1:1	33:2:2
C_{B1}, C_{B2}	5.8 mF/50 V, 5.8 mF/50 V
f_s	100 kHz
f_l	50–60 Hz
v_{in}	100-240 Vrms AC
S_1	NTP6N60
S_2, S_3	IRF840
D	CSD6060
Secondary Rectifier Diode	MBR2545

Table 4.2: Calculated (cal) and measured (mea) voltage stress $v_{D(\max)}$ and current stress $i_{p(\max)}$ at different duty cycles.

Duty cycle of S_1	$v_{D(\text{cal})}$(V)	$v_{D(\text{mea})}$(V)	$i_{p(\text{cal})}$(A)	$i_{p(\text{mea})}$(A)
0.1	213	180	0.98	1.05
0.2	250	240	1.30	1.3
0.3	316	305	1.59	1.45
0.4	388	380	1.90	1.59
0.5	465	460	2.28	1.75

rent, i.e. $\omega_r(1 - d_{max})T_S > \pi$. Therefore $L_pC_p \leq \left(\frac{(1-d_{max})T_S}{\pi}\right)^2$, and $C_p \leq$ 72.3 nF. Choose C_p = 69 nF. The output capacitors C_{B1} and C_{B2} should be large enough to serve as voltage hold-up capacitor at $2f_l$ for maximum loading conditions. For the existing values of C_{B1} and C_{B2}, we have $\frac{v_{O1}}{v_{O0}} < 0.1$. The lifetimes of C_{B1} and C_{B2} can follow the equation: $L_{\text{cap}} = L_B M_v 2^{\frac{\Delta T}{10}}$ [96], where L_B is the base lifetime at the maximum core temperature and M_v is a voltage multiplier which is designated as the ratio of capacitor rated voltage to applied voltage. ΔT is the temperature rise in the capacitor. Here, we use 5.8 mF/ 50 V Vishay aluminum electrolytic capacitors with L_B of 12,000 hours [124]. Using M_v = 50/12, the lifetimes of C_{B1} and C_{B2} can achieve 50,000 hours matching with that of LED lamps. In practice, the voltage fluctuation can be as high as $\frac{v_{O1}}{v_{O0}}$ = 0.5,

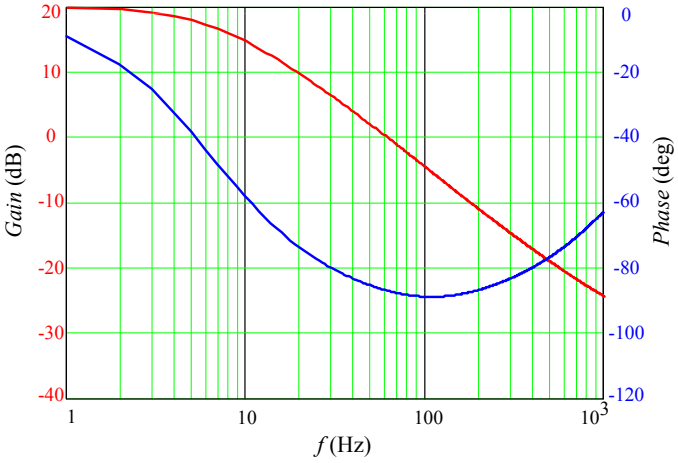

(a)

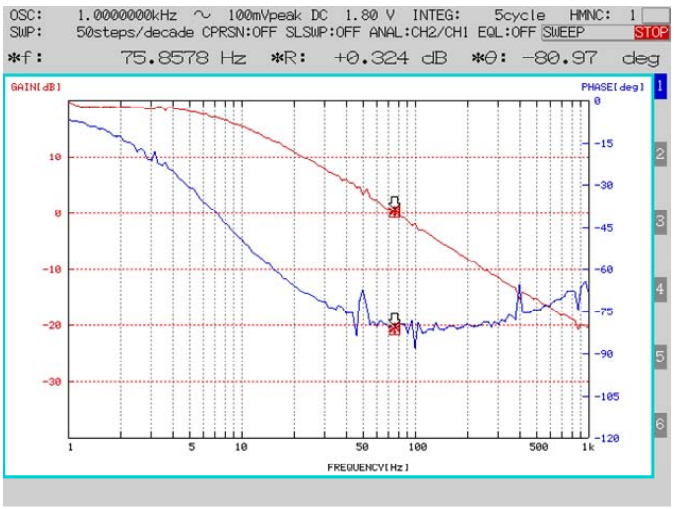

(b)

Figure 4.8: Magnitude and phase of output-to-control transfer function Eq. (4.34) at $d = 0.4$. (a) Theoretical calculation. (b) Experimental results.

taking into consideration the regulation provided by the LED current driver. In this case, C_{B1} and C_{B2} can take the value of 1.1 mF. With all these component values found, constants K_1 to K_8 as well as voltage and current stresses can be determined according to the procedure described in Section 4.4.

Fig. 4.7 shows a comparison of the normalized voltages of the experimental and calculated results of the PFC pre-regulator for different values of duty cycle

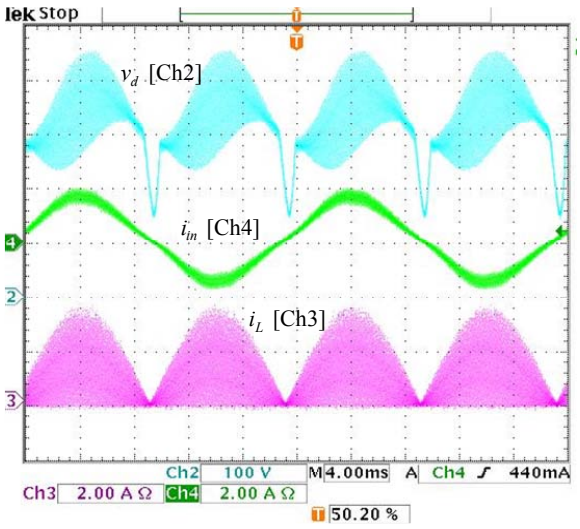

Figure 4.9: Experimental waveforms of v_D, i_{in} and i_L at full load and 100 Vrms AC input.

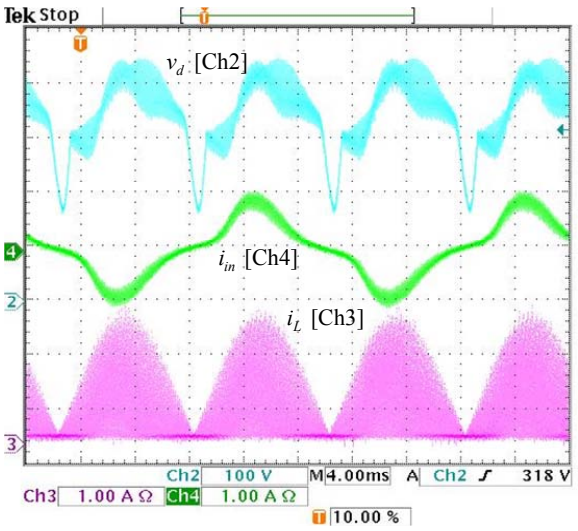

Figure 4.10: Experimental waveforms of v_D, i_{in} and i_L at full load and 240 Vrms AC input.

d. We use a loading resistance for the transformer secondary windings of 1.73 Ω which corresponds to R_O = 1.73 Ω × n^2 = 471 Ω in the primary. Table 4.2 compares the calculated values of voltage and current stress using (4.15) and (4.16) with the measured values.

The theoretical calculation of the small-signal transfer function using d =

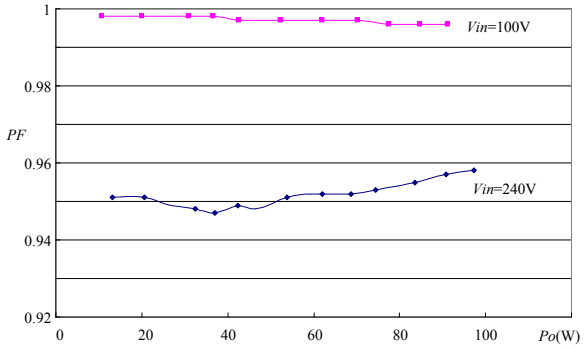

Figure 4.11: Power factor versus output power at two different line input voltages.

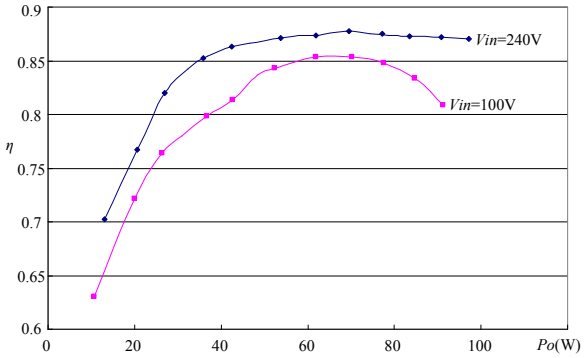

Figure 4.12: Efficiency versus output power at two different line input voltages.

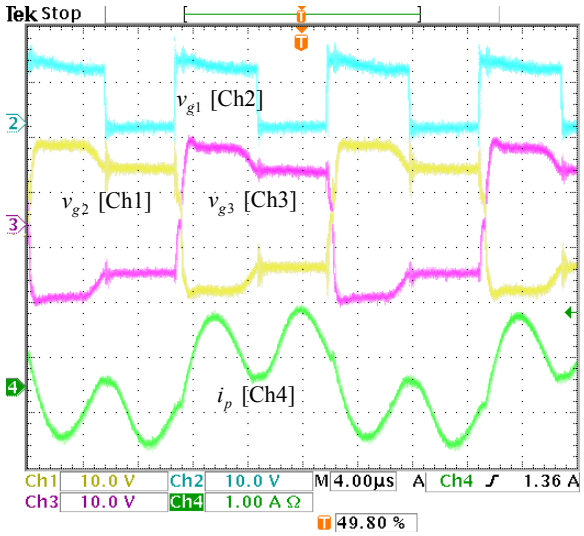

Figure 4.13: Gate drive voltages of S_1, S_2, and S_3 and the corresponding current waveform i_p.

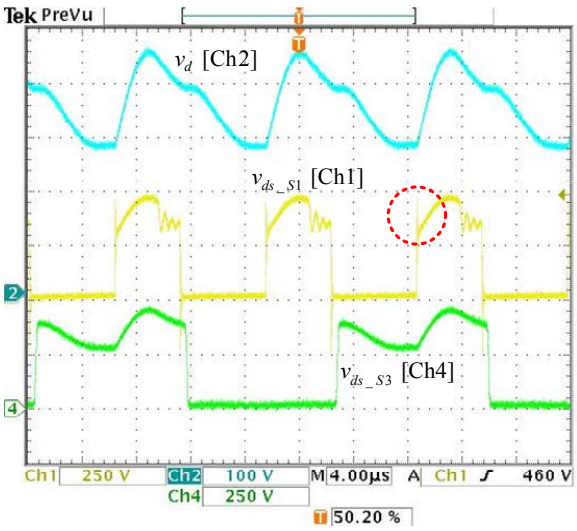

Figure 4.14: Voltage waveforms of v_d (see Fig. 4.4) and v_{ds} of S_1 and S_3.

0.4 in Eq. (4.34) is given in Fig. 4.8 (a), and Fig. 4.8 (b) is the related experimental graph consistent to the theoretical results. Figs. 4.9 and 4.10 show the experimental waveforms of v_D, i_L and i_{in} at full load conditions for 100 Vrms and 240 Vrms AC input, respectively, where i_{in} is the line input current observed using a line filter. The power factors and efficiencies measured at 100 Vrms and 240 Vrms AC input are shown in Figs. 4.11 and 4.12, respectively, for different power loadings. The lower power factor measured at 240 Vrms AC input is due to a larger d_2 which makes the boost inductor input less resistive. The results are consistent with that reported in [125]. The efficiency figures are typical for low output voltage design where a relatively high ratio of rectifying diode drop to output voltage has been observed. Fig. 4.14 shows the voltage stress of the switching MOSFETs. Even without the use of snubber circuits [123], the voltage ringings across the power switches are relatively small.

4.6 Summary

One challenge of the design of power converters for LED lighting applications is to extend the lifetime of the converters such that the durability of LEDs can be put to the practical advantage. The main problem with conventional power converters is the use of high-voltage storage capacitors which limits the lifetime of LED lighting systems. This chapter presents a new isolated PFC pre-regulator for LED lighting applications. The pre-regulator does not require a high-voltage charge storage capacitor on the transformer primary. Instead, low-voltage hold-up capacitors can be used on the transformer secondary to reduce cost and extend the lifetime of capacitors. Voltage and current stress for power devices have been estimated and experimentally verified. In the next chapter the concept of non-cascading structure for the design of the LED ballast will be discussed. Demonstration of operating the converter in continuous conduction mode will also be given for power higher than 100 W.

Chapter 5

Non-cascading Structure for Electronic Ballasts

5.1 Introduction

A technique for eliminating the high-cost short-lifetime high-voltage capacitor using an isolated DCM current-fed PFC circuit has been described in Chapter 4. In this chapter, we operate the circuit in continuous conduction mode (CCM), as shown in Fig. 5.1, to permit the high power factor to be achieved easily with the conventional average-current-mode (ACM) control method [126]. The circuit structure and analysis are the same as that in Chapter 4 except the control scheme.

Two secondary output windings of the transformer are used in the non-cascading output configuration [120]. One of the outputs is connected directly (without being processed) in series with the other output which is then current regulated by a PWM buck converter to drive an LED lamp. Additional buck converters and identical secondary connections can be included to drive more LEDs independently. Since the energy from one output winding can directly be used to

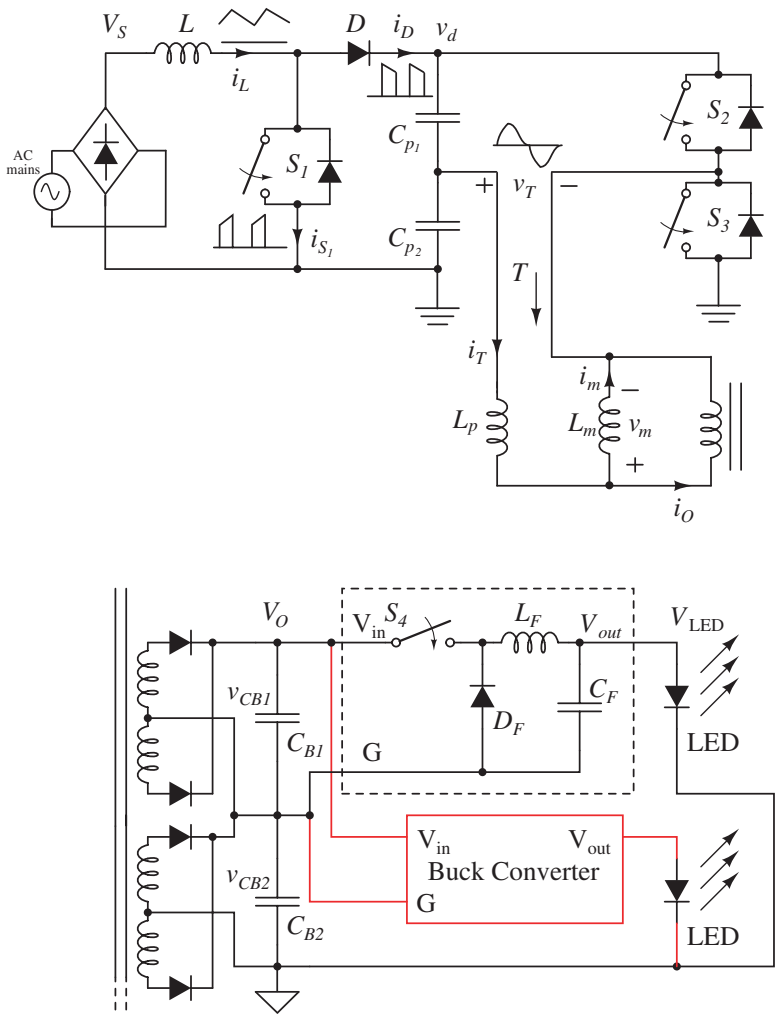

Figure 5.1: Circuit schematic of the proposed LED ballast with a front-end PFC pre-regulator on the transformer primary and post-end LED current regulators on the secondary connected in the non-cascading configuration. The PFC pre-regulator is chosen to operate at CCM.

drive the LED without going through the other power stage, a higher efficiency can be guaranteed.

In the following sections, we will focus on how to optimize the design of the non-cascading structure to achieve high efficiency based on the CCM PFC pre-regulator.

5.2 PFC Pre-Regulator Operating in CCM

The upper circuit in Fig. 5.1 is a boost input stage operating in CCM for high-power LED lamp applications. The main switch S_1 is programmed at a fixed frequency f_S using ACM control to shape the input current and control the amount of power supplied to the current regulators. Thus, the input line filter can be removed, which is different from that in DCM operation described in Chapter 4. We continue to use the transformer model consisting of L_p and L_m, as shown in Chapter 4, for the analysis of the CCM pre-regulator. For simplicity of the PFC pre-regulator, an equivalent rectifying load consisting of a diode bridge and the output load (C_O and R_O) reflected on the primary is used for analysis.

Fig. 5.2 shows typical waveforms of voltages and currents of the power converter. As shown previously in a similar analysis for the DCM operation in Chapter 4, the derivation of the exact waveforms of $v_{C_{p1}}(t)$, $v_{C_{p2}}(t)$, $i_D(t)$, and $i_p(t)$ (which are used to determine the voltage and current stress of the power switches S_1, S_2, and S_3) can be very complex. Here, we will adopt the following approximate method. The boost input stage and the half-bridge converter are considered as separate stages. They are connected using the averaged state variables. The inductor L is sufficiently large that $i_D(t)$, $i_p(t)$ and $v_D(t)$ reach their maximum during the time when S_1 conducts. The voltage and current stress are approximated as

$$\max(i_D(t)) = i_S + \frac{v_S}{2L} dT_S, \tag{5.1}$$

$$\max(i_p(t)) = \frac{v_{C_p} - v_O}{Z_r}, \text{ and} \tag{5.2}$$

$$\max(v_D(t)) = 2v_{C_p}, \tag{5.3}$$

where i_S, v_{C_p} are averaged values within a switching cycle and $Z_r = \sqrt{L_p/C_p}$. Here, for brevity, we denote x as the averaged value of $x(t)$. Therefore, once the averaged state variables are known, the peak of the instantaneous quantities

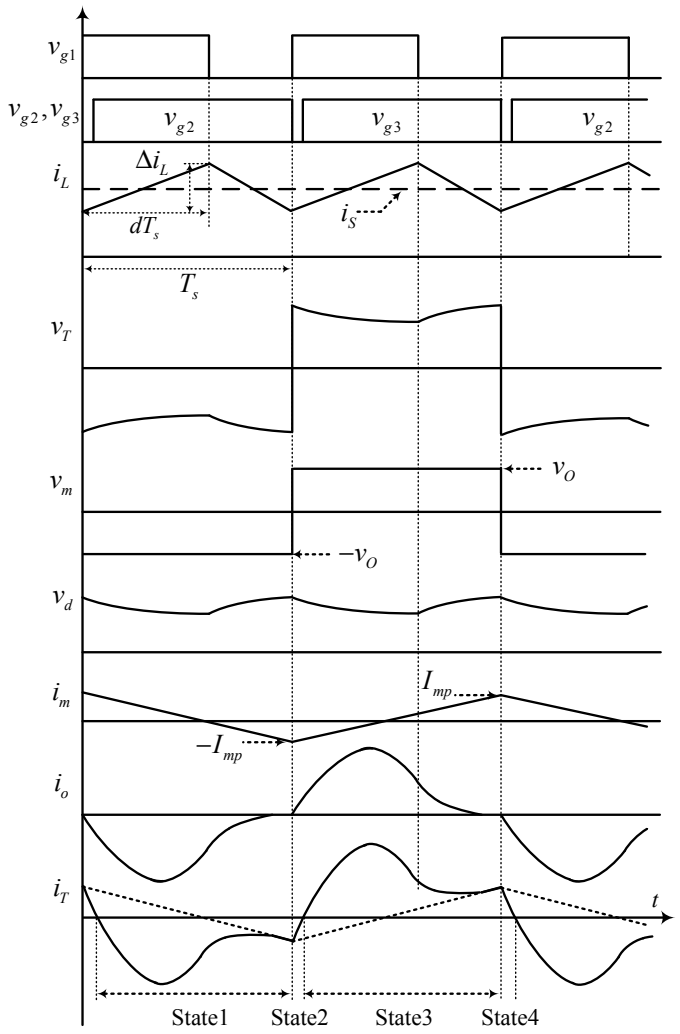

Figure 5.2: Simplified waveforms of i_L for the boost converter and i_T $(= i_p)$ for the half-bridge converter. i_m and v_m are current and voltage of the mutual inductor L_m, respectively. The resonance of L_p and C_p ends when $i_p(t)$ meets $i_m(t)$, thus the period T_r in (4.26) satisfies $\frac{T_r}{2} \leq T_S$.

within a switching cycle can be readily estimated. It is assumed that C_p and L_p start to resonate due to the voltage difference $v_{C_p} - v_O$ when S_2 (or S_3) conducts. It is also assumed that $v_{C_p}(0) = \overline{v_{C_p}(t)} = v_{C_p}$. The leakage inductor current is calculated as

$$i_p(t) = \frac{v_{C_p} - v_O}{Z_r} \sin \omega_r t, \tag{5.4}$$

where $\omega_r = \frac{1}{\sqrt{L_p C_p}}$, $t = 0$ at the time S_2 turns on, and the resonance ends at $t = \frac{\pi}{\omega_r} = \frac{T_r}{2}$. Hence, the averaged output current is calculated using

$$i_O = \frac{1}{T_S}\int_0^{\frac{T_r}{2}} i_p(t)dt \approx \frac{2}{\pi}\frac{v_{C_p} - v_O}{Z_r} \tag{5.5}$$

The input voltage is rectified as a positive half sinusoid, i.e.,

$$v_S = V_S \left|\sin 2\pi f_l t\right|. \tag{5.6}$$

As a result of ACM control,

$$i_S = I_S \left|\sin 2\pi f_l t\right|. \tag{5.7}$$

Using approximation of the instantaneous power balance at the line frequency, we obtain

$$v_O = V_{O0} - V_{O1}\sin(4\pi f_l t), \tag{5.8}$$

where V_{O0} is the dc component and V_{O1} is the fundamental at $2f_l$, i.e.,

$$V_{O0} = \sqrt{\frac{V_S I_S R_O}{2}} \tag{5.9}$$

$$V_{O1} = \frac{V_{O0}}{4\pi f_l R_O C_O} \tag{5.10}$$

The output current is determined as

$$i_O = I_{O0} + I_{O1}\sin\left(4\pi f_l t - \frac{\pi}{2}\right), \tag{5.11}$$

where

$$I_{O0} = \frac{V_{O0}}{R_O} \text{ and } I_{O1} = I_{O0}. \tag{5.12}$$

The output voltage and current shown in (5.8) and (5.11) can be determined if the input power is known. However, the input power also depends on the output voltage v_D of the boost stage governed by (5.5). Equation (5.5) can be rewritten as

$$g \equiv i_O - \left(\frac{2}{\pi}\frac{v_D/2 - v_O}{Z_r}\right) = 0. \tag{5.13}$$

Substituting $v_D = V_{D0} + V_{D1}\sin(4\pi f_l t + \theta_D)$ into (5.13), the following equalities from harmonic balance hold:

$$\begin{cases} \int_0^{\frac{1}{2f_l}} g(t)\,\mathrm{d}t = 0 \\ \int_0^{\frac{1}{2f_l}} \sin(4\pi f_l t) g(t)\,\mathrm{d}t = 0 \\ \int_0^{\frac{1}{2f_l}} \cos(4\pi f_l t) g(t)\,\mathrm{d}t = 0 \end{cases} \tag{5.14}$$

Solving (4.51) with $v_D \approx V_{D0} + V_{D1}\sin(4\pi f_l t - \theta_D)$ gives four possible solutions, of which only one satisfies $V_{D0} > V_{O0}$, i.e.,

$$V_{D0} = V_{O0}(2 + \frac{K_3\pi}{R_O}) \tag{5.15}$$

$$V_{D1} = V_{O0}\sqrt{K_4^2 + K_5^2} \tag{5.16}$$

$$\theta_D = \pi + \tan^{-1}\frac{K_4}{K_5} \tag{5.17}$$

where

$$K_1 = \frac{T_S R_O}{2L}, \quad K_2 = \frac{1}{4\pi f_l R_O C_O}, \tag{5.18}$$

$$K_3 = \sqrt{\frac{L_p}{C_p}}, \quad K_4 = 2K_2, \quad \text{and} \quad K_5 = -\frac{K_3 \pi}{R_O}. \tag{5.19}$$

The calculation of the steady-state solutions is summarized as follows. Given circuit parameters K_1 to K_5 in (5.18) to (5.19), and V_{O0} being regulated by the outer voltage loop, V_{O1} can be calculated using (5.10), V_{D0} using (5.15), and V_{D1} using (5.16).

5.3 Analysis and Implementation of Non-Cascading Output Configuration

5.3.1 Theoretical Analysis for Efficiency Improvement

We denote η_1 and η_2 as the efficiency of the isolated PFC converter and the buck converter, respectively, and define k as the percentage of the output power from the pre-regulator that goes directly to the LED load. For our non-cascading structure, the overall efficiency η is given as

$$\eta = k\eta_1 + (1-k)\eta_1\eta_2, \tag{5.20}$$

where $k < 1$, $\eta_1 < 1$, and $\eta_2 < 1$.

Rearranging (5.20) gives

$$\eta = \eta_1 \left(\eta_2 + k(1-\eta_2)\right) = \eta_1 \eta_2'. \tag{5.21}$$

Obviously, η_2' is the equivalent efficiency of the "improved" buck converter. Re-

ferring to Fig. 4.3, the LED is connected in series with two voltage sources consisting of V_{out} and $v_{C_{B2}}$. The power provided by the output of the buck converter and $v_{C_{B2}}$ can be calculated as $I_{\rm LED}V_{out}$ and $I_{\rm LED}v_{C_{B2}}$, respectively, where $I_{\rm LED}$ is the LED driving current. The corresponding input power of the buck converter is therefore given as $I_{\rm LED}V_{out}/\eta_2 = I_{\rm LED}(V_{\rm LED} - v_{C_{B2}})/\eta_2$, where $V_{\rm LED}$ is the voltage across an LED. Hence, further simplification gives

$$\eta_2' = \frac{V_{\rm LED}}{v_{C_{B2}} + (V_{\rm LED} - v_{C_{B2}})/\eta_2}, \tag{5.22}$$

$$k = \frac{v_{C_{B2}}}{v_{C_{B2}} + (V_{\rm LED} - v_{C_{B2}})/\eta_2}. \tag{5.23}$$

Typical forward diode voltages of red, green, blue and white LEDs are 2.4 V, 3.55 V, 3.75 V and 3.75 V, respectively. Different packages of LED lamps may integrate identical LEDs in series or parallel producing forward voltages and currents in multiple of that from a single LED.

From the voltage transfer property of the buck converter, $0 < d_{\rm buck} = \frac{V_{\rm LED} - v_{C_{B2}}}{v_{C_{B1}}} < 1$, we have the following inequality

$$0 \leq v_{C_{B2}} < V_{\rm LED} < v_{C_{B1}} + v_{C_{B2}} = V_o \tag{5.24}$$

Specifically, if $v_{C_{B2}}$ is equal to 0, the circuit reduces to the conventional cascading structure. For practical applications, $V_{\rm LED}$ is fixed and η_2 in (5.22) can be estimated by calculating the power dissipation of the buck converter. Hence, it is available to determine $v_{C_{B2}}$ and V_o for the maximum of η_2'.

5.3.2 Optimization with Independent Brightness Control

Now we illustrate, using an example, the technique of optimizing efficiency for the non-cascading configuration. Suppose that the LED lamps are series-connected, composing of four blue LEDs with $V_{\rm LED} = 14.45$ V. Three such

series-connected LEDs are connected in parallel to draw a driving current of 1020 mA. A current source based on a buck topology using LT1510 operating at a switching frequency of 200 kHz is used for illustration. Fig. 5.3 gives the schematic of the buck switching converter behaving essentially as a current source whose magnitude is controlled by a PWM signal. PWM gate pulses, $V_{\rm PWM}$ and $\overline{V_{\rm PWM}}$, which are applied at a frequency of 200 Hz to the MOS transistors Q_1 and Q_2 respectively, can change the intensity of the lamp instantaneously at a fixed color point. For lighting applications where 100 % dimming is normally not necessary, Q_2 in Fig. 5.3 can be removed. Here, without loss of generality, $V_{\rm PWM}$ is kept low and Q_2 is replace by a short circuit. We have calculated the power dissipation in the IC circuit [112], including loss dissipated in the bias and driver, switch resistance, switch transition, current sensing resistor, conduction loss of the buck inductor and the freewheeling diode, where the buck inductor parasitic resistance of 0.45 Ω and the Schottky freewheeling diode voltage drop during on-stage of 0.5 V are used in the calculation. Fig. 5.4 plots the efficiency η_2 of the buck converter versus $v_{C_{B1}}$ for different values of V_o ($= v_{C_{B1}} + v_{C_{B2}}$). From Fig. 5.4, when V_o is constant, η_2 increase with $v_{C_{B1}}$ because of larger duty cycle and smaller conduction current flowing into D_F.

From (5.22) and Fig. 5.4, we can plot the efficiency η_2' versus $v_{C_{B2}}$ and V_o to form a surface, as shown in Fig. 5.5, where the surface with projection inside the red triangle on the $v_{C_{B2}}$-V_o plane is non-operational for the IC as it needs a supply voltage $v_{C_{B1}}$ higher than 7.8 V. To help visualize how η_2' changes with $v_{C_{B2}}$ and V_o, a family of curves are given in Fig. 5.6. These curves illustrate that η_2' is much higher at $v_{C_{B2}} \approx$ 12 V for the whole range of V_o. Therefore, the maximum η_2' must be on the line of interception between the efficiency plane and the vertical plane at $v_{C_{B2}}$ =12 V. The line is redrawn in Fig. 5.7, where the maximum of η_2' occurs at ($v_{C_{B2}}$, V_o) = (12 V, 19.8 V), as shown in Fig. 5.5.

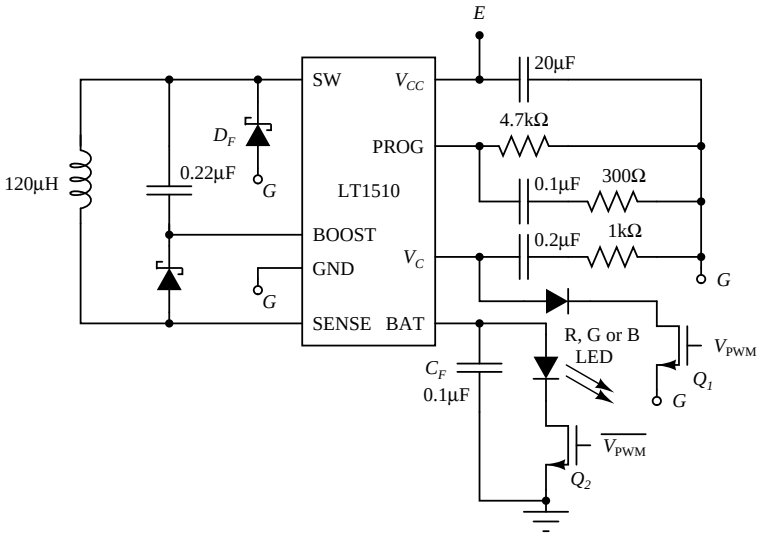

Figure 5.3: Switching converter with PWM control as a constant current driver. The connection point G is shown in Fig. 5.1.

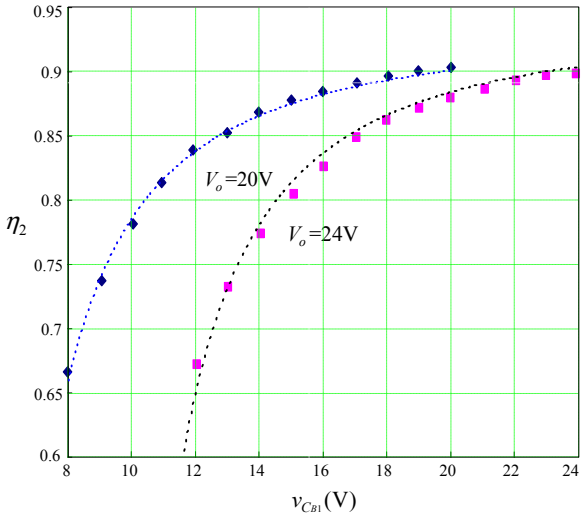

Figure 5.4: Efficiency η_2 of the buck converter in the non-cascading structure at different values of V_o. Dotted lines are theoretical calculations and diamonds are experimental data points.

According to (5.8), the capacitor voltages at $2f_l$ can be expressed as follows:

$$v_{C_{B1}}(t) = v_{C_{B1_0}} - v_{C_{B1_1}} \sin(4\pi f_l t), \tag{5.25}$$

$$v_{C_{B2}}(t) = v_{C_{B2_0}} - v_{C_{B2_1}} \sin(4\pi f_l t), \tag{5.26}$$

$$V_o(t) = v_{C_{B1}}(t) + v_{C_{B2}}(t) \tag{5.27}$$

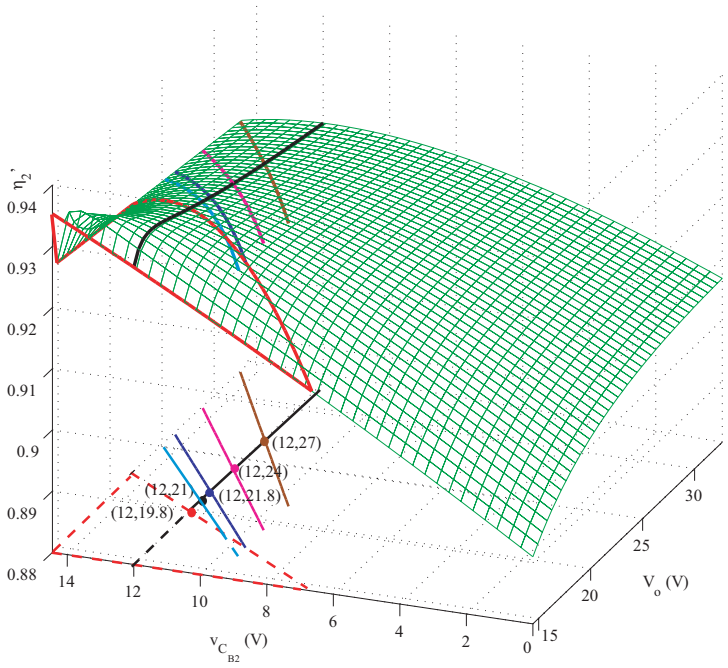

Figure 5.5: Efficiency surface η_2' as a function of V_o and $v_{C_{B2}}$. For a given V_o, the efficiency η_2' is minimum and maximum when $v_{C_{B2}}$ = 0 V and $v_{C_{B2}}$ = 12 V respectively.

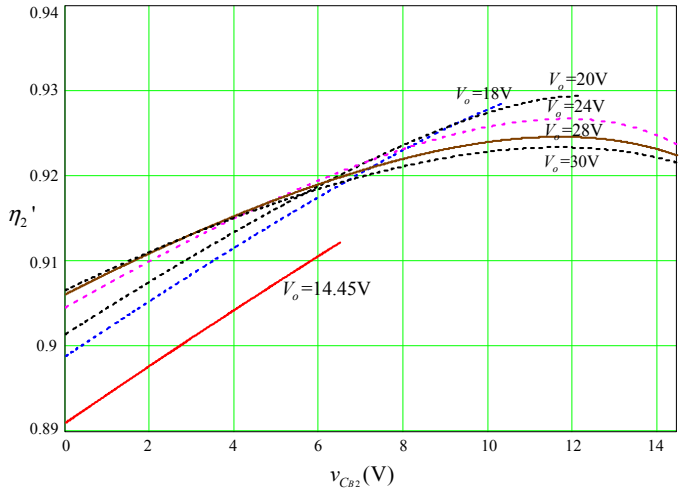

Figure 5.6: Efficiency η_2' versus $v_{C_{B2}}$ at different values of V_o from Fig. 5.5.

where $v_{C_{B1_1}}$ and $v_{C_{B2_1}}$ satisfy (5.10), depending on the values of the filtering capacitors C_{B1} and C_{B2} and the transformer coupling coefficient. Rewrite (5.10)

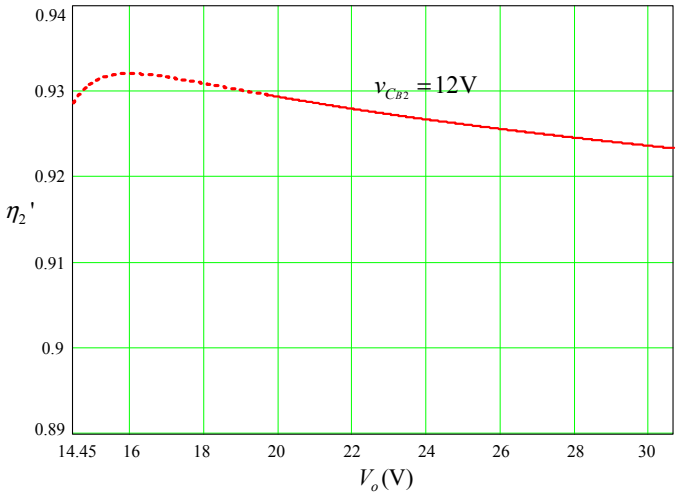

Figure 5.7: Efficiency η_2' versus V_o at $v_{C_{B2}}$ = 12 V from Fig. 5.5

by considering their respective reactive powers:

$$C_{B1} = \frac{(1-k)P_o}{4\pi f_l v_{C_{B1_0}} v_{C_{B1_1}}} \tag{5.28}$$

$$C_{B2} = \frac{kP_o}{4\pi f_l v_{C_{B2_0}} v_{C_{B2_1}}} \tag{5.29}$$

It should be noted that $\frac{v_{C_{B1_0}}}{v_{C_{B2_0}}} \equiv \frac{v_{C_{B1_1}}}{v_{C_{B2_1}}} = \frac{m_1}{m_2}$ for unity coupling of the transformer of turns ratio of $n : m_1 : m_2$.

Equations (5.25) to (5.29) indicate that the non-cascading converter is not operating at a single efficiency point of η_2', but rather operating along the line segments centered at the chosen point of $(V_{C_{B2_0}}, V_{o_0})$, as shown in Fig. 5.5. The line segments centered at $V_{C_{B2}}$ = 12 V and V_o = 19.8, 21, 21.8, 24 and 27 V are illustrated in Fig. 5.5. To minimize the cost of filtering capacitors, the maximum allowable $v_{C_{B2_1}}$ is calculated from (5.24), i.e.,

$$\max(v_{C_{B2_1}}) = V_{\text{LED}} - v_{C_{B2_0}} = 14.45 - 12 = 2.45 \text{ V}. \tag{5.30}$$

Shown in Fig. 5.5 are line segments in the $v_{C_{B2}}$ projection limited to $2\max(v_{C_{B2_1}}) =$ 4.9 V, where the operating points at (12 V, 19.8 V) and (12 V, 21 V) would not

lead to the use of minimum filtering capacitors.

Clearly, the efficiency η_2' varies periodically in half-line-period along one of the efficiency curves, as illustrated in Fig. 5.5. The average efficiency $\overline{\eta_2'}$ for the non-cascading converter is calculated by substituting (5.22), (5.25), (5.26) and (5.27) into the following expression:

$$\overline{\eta_2'}(v_{C_{B2_0}}, V_{o_0}, v_{C_{B2_1}}) = \frac{2}{T_l}\int_0^{T_l/2} \eta_2'(v_{C_{B2}}(t), V_o(t))dt \tag{5.31}$$

Using (5.28), (5.29) and (5.31), we get Fig. 5.8, which shows the relationship between C_{B1} (or C_{B2}) and $\overline{\eta_2'}$. Three curves are calculated at different values of $(v_{C_{B2_0}}, V_{o0})$ with $v_{C_{B2_1}}$ varying from 2.45 V to 1.225 V by increasing the values of C_{B1} and C_{B2}.

5.3.3 Extension to More Structures

To give an idea of how the efficiency of the non-cascading converter changes with different numbers of LED lamps in parallel and in series, Fig. 5.9 gives the maximum η_2' for three parallel connections of different number of series connected LEDs at a total current of 1020 mA. Also shown in Fig. 5.9 are efficiencies for the same buck converter using synchronous rectifiers [127], Schottky diode and ultra-fast diode with a forward voltage of 0.05 V, 0.5 V and 1.0 V, respectively. Fig. 5.10 shows the maximum η_2' for different number of parallel connection of LEDs at $V_{\rm LED}$ = 14.45 V.

In practice, RGB or white LEDs may have different values of $V_{\rm LED}$ and thus the maximum η_2' may vary. We also note that separate PFC transformer turns ratios should be used for red, green and blue LEDs to achieve the corresponding maximum efficiency.

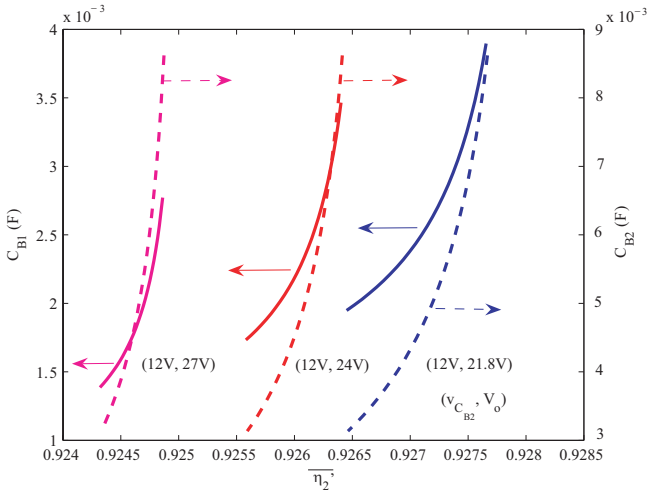

Figure 5.8: Average efficiency $\overline{\eta_2'}$ as a function of C_{B1} or C_{B2}. For a given $\overline{\eta_2'}$, the values of C_{B1} and C_{B2} are in one-to-one correspondence.

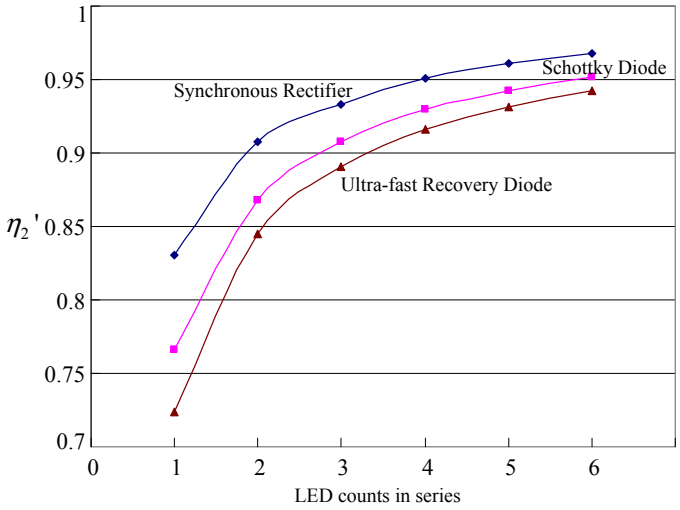

Figure 5.9: η_2' as a function of LED counts in series. V_{LED} is calculated using an integer multiple of 3.6 V. Three curves are plotted for the buck converter using synchronous rectifier, Schottky diode and ultra-fast recovery diode with forward voltage of 0.05 V, 0.5 V and 1.0 V, respectively.

5.4 Experimental Evaluation

A prototype of the proposed LED electronic ballast has been built for driving LED lamps having a total power up to 100 W. The PFC pre-regulator is regulated using the conventional ACM control. Using the results of the last two

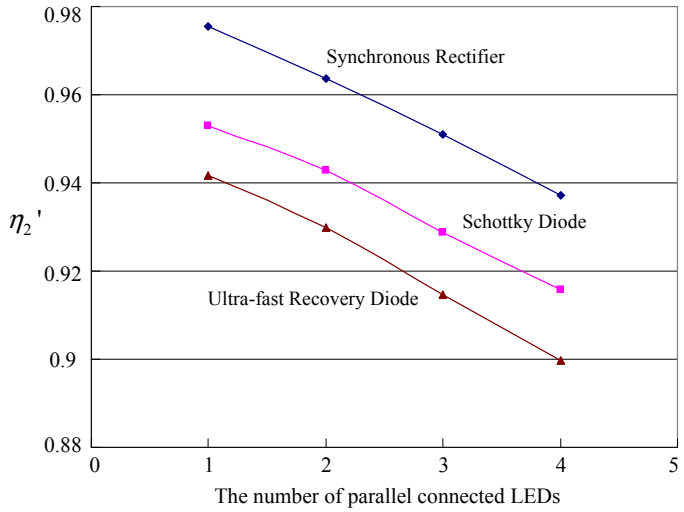

Figure 5.10: η_2' as a function of the number of parallel connected LEDs. Driving current of integer multiple of 350 mA are used for the calculations.

sections, we arrive at the components and parameter values shown in Table 5.1. In particular, C_p is chosen according to $\omega_r = \sqrt{1/L_pC_p}$ such that $\omega_r T_S > \pi$. This allows the energy stored in L_p to be completely discharged before the start of the next switching state, thus minimizing circulating current. The output voltage $v_{C_{B2}}$ is designed at 12 V to give the optimum efficiency. The transformer turns ratio in Table 4.1 gives V_o = 24 V. Thus, the efficiency of the buck converter in the non-cascading structure can be obtained from Fig. 5.4 as 66.8 %. Also, k is obtained using (5.23) as 76.6 %. The output capacitors C_{B1} and C_{B2} should be large enough to serve as voltage hold-up capacitor at $2f_l$ for the maximum loading condition. Considering the minimum operation voltage requirement of the the LED current driver, the voltage fluctuation can be as high as $\frac{v_{O1}}{v_{O0}} < 0.2$. In the experimental setup, we use $\frac{v_{C_{B2_1}}}{v_{C_{B2_0}}} = \frac{13.5\text{-}12}{12}$ = 0.125 to achieve a much larger range of voltage safety operation region. The output capacitors are calculated using (5.25) and (5.26) as C_{B1} = 2.12 mF and C_{B2} = 6.72 mF. We use capacitors of 2.2 mF / 50 V and 6.9 mF / 50 V for C_{B1} and C_{B2}, respectively.

Fig. 5.11 shows a comparison of the normalized voltages of the experimentally measured and calculated results of the PFC pre-regulator for the different values of the output power P_O. Table 5.2 compares the calculated values of volt-

Table 5.1: Components and parameter values used in experiments.

Components/parameters	Values
L	2.92 mH
C_p	242 nF
L_p	35 μH
L_m	1.85 mH
turns ratio n:m_1:m_2	33:2:2
C_{B1}, C_{B2}	2.2 mF/50 V, 6.9 mF/50 V
f_s	100 kHz
f_l	50–60 Hz
v_{in}	100–240 Vrms AC
S_1	NTP6N60
S_2, S_3	IRF840
D	CSD6060
secondary rectifier diode	MBR2545
Q_2	70N06L

Table 5.2: Calculated (cal) and measured (mea) voltage stress $v_{D(\max)}$ and current stress $i_{p(\max)}$ at different output powers.

Power(W)	$v_{D(\text{cal})}$(V)	$v_{D(\text{mea})}$(V)	$i_{p(\text{cal})}$(A)	$i_{p(\text{mea})}$(A)
20	405	420	0.382	0.385
40	414	434	0.765	0.77
60	423	446	1.151	1.18
80	432	458	1.539	1.65
100	441	470	1.926	2.03

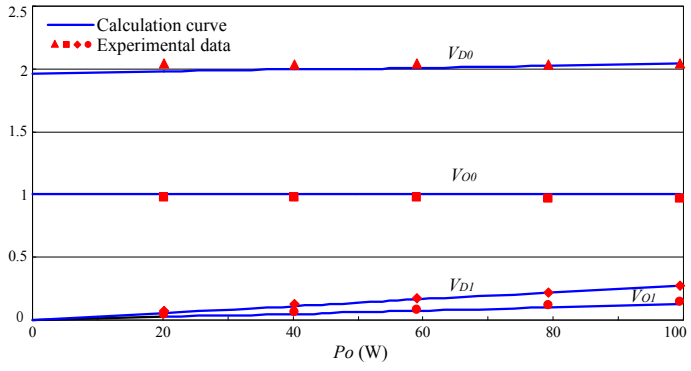

Figure 5.11: Comparison of the calculated and experimental values of V_{O0}, V_{O1}, V_{D0} and V_{D1} normalized to V_{O0}.

age and current stress using (5.2) and (5.3) with the measured values.

Figs. 5.12 and 5.13 show the experimentally measured waveforms of v_d, v_{in}

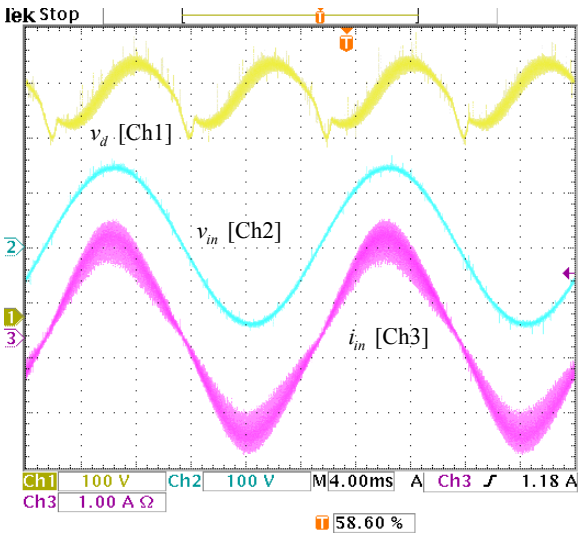

Figure 5.12: Experimental waveforms of v_D, i_{in} and i_L at full load and 100 Vrms AC input.

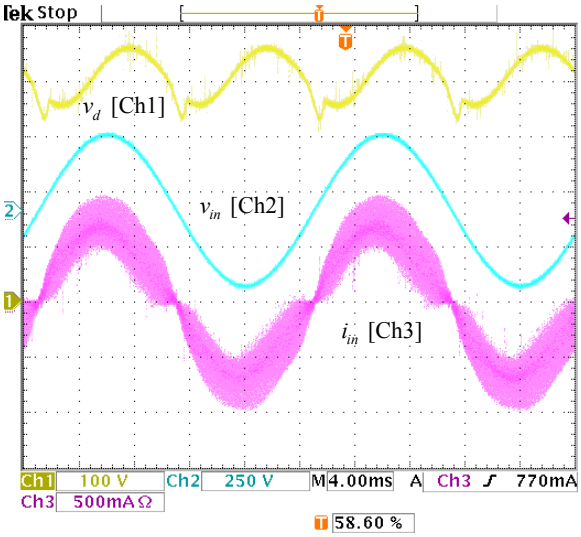

Figure 5.13: Experimental waveforms of v_D, i_{in} and i_L at full load and 240 Vrms AC input.

and i_{in} at full load conditions for 100 Vrms and 240 Vrms AC input, respectively. We see that i_{in} is regulated as a nearly perfect sinusoidal waveform at 110 Vrms AC input. The power factors and efficiencies measured at 100 Vrms and 240 Vrms AC inputs are shown in Figs. 5.14 and 5.15, respectively, for different loadings. The low power factor measured at 240 Vrms AC input is due to the converter operating into DCM at the low power level, making the boost

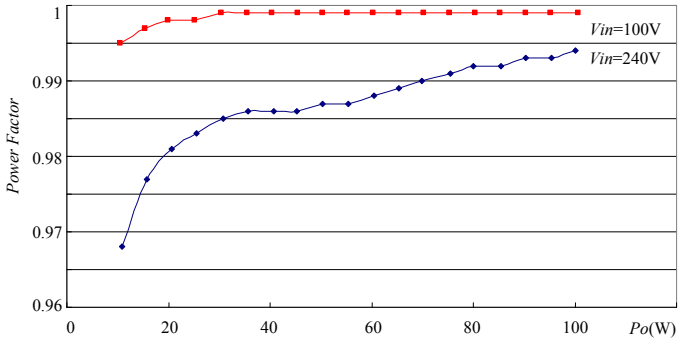

Figure 5.14: Power factor versus output power at two different line input voltages.

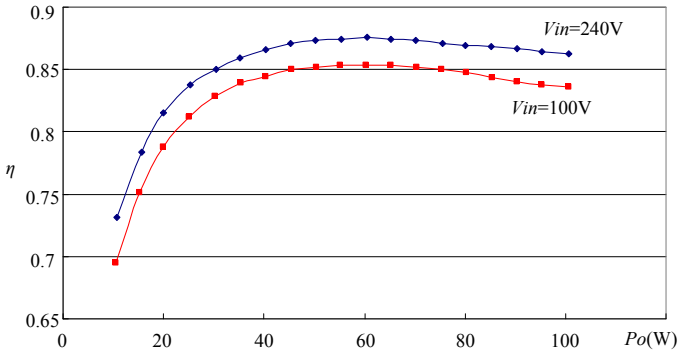

Figure 5.15: Efficiency versus output power at two different line input voltages.

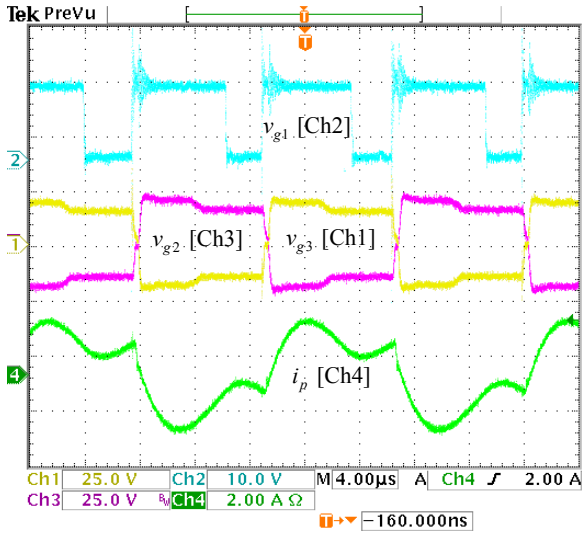

Figure 5.16: Gate drive voltages of S_1, S_2, and S_3 and the corresponding current waveform i_p.

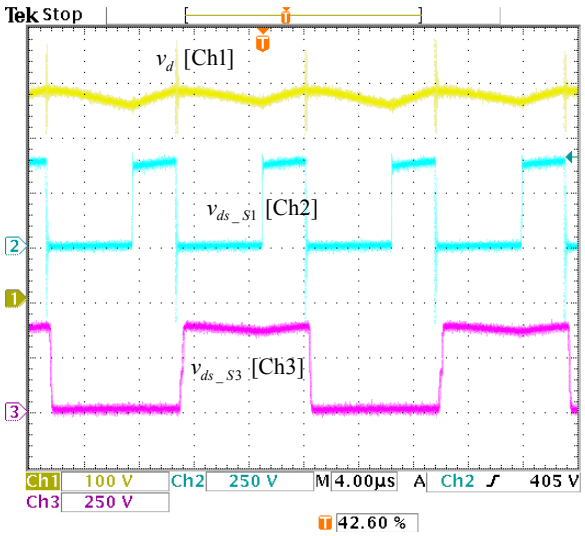

Figure 5.17: Voltage waveforms of v_d (see Fig. 5.2) and v_{ds} of S_1 and S_3.

inductor current difficult to track the sinusoidal reference current. The efficiency figures are typical for low output voltage design where a relatively high ratio of rectifying diode drop to output voltage has been observed. Fig. 5.16 gives the gate signal sequences of three MOSFETs S_1, S_2 and S_3 and the resonant current i_p flowing into the transformer primary. Fig. 5.17 shows the voltage stress of the switching MOSFETs. Even without the use of snubber circuits [123], the voltage ringings across the power switches are relatively small.

The measured efficiency η_2 of the buck converter is plotted as diamonds in Fig. 5.4. An evaluation of the effectiveness in the brightness control of the circuit in Fig. 5.3 is shown in Fig. 5.18. The corresponding waveforms of PWM current generated by the converter with and without the incorporation of Q_2 in Fig. 5.3 are shown in Figs. 5.19 and 5.20 respectively. Fig. 5.21 gives the voltage ripple across storage capacitors C_{B1} and C_{B2} and the LED lamps can operate effectively. The measured $\overline{\eta_2'}$ are 92.07 % and 92.14 % for the circuit in Fig. 5.3 with and without Q_2 respectively, and η_2 is 89.26 %. An improvement of as high as nearly 3 % in efficiency has been achieved with very little additional cost.

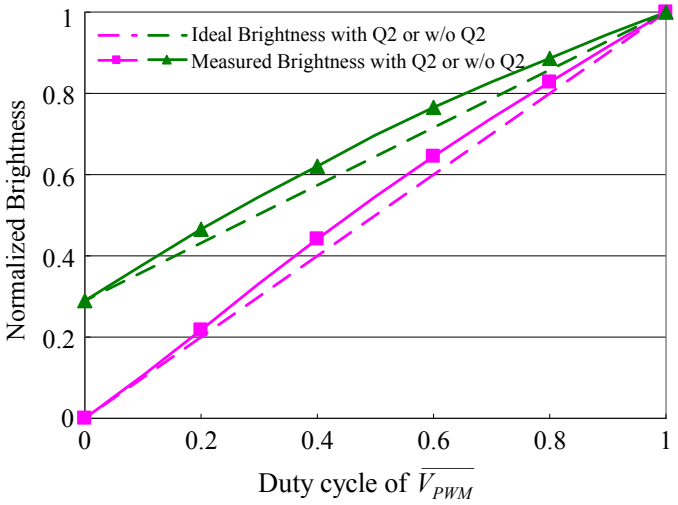

Figure 5.18: Evaluation of brightness control of the circuit in Fig. 5.3 with Q_2 and without Q_2 (which is replaced by a short circuit). The two control techniques give identical brightness at duty cycle being 1. Squares and triangles are measured data points with and without Q_2 respectively. Solid lines are fitted lines of the measured data sets. Dotted lines are ideal linear responses of brightness control. The differences in ideal and measured brightness are due to the lower LED luminous efficacy at higher junction temperature when the LED is operating at higher output power.

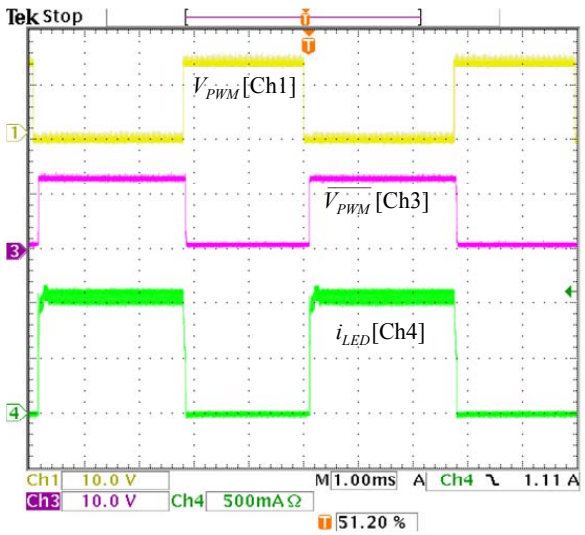

Figure 5.19: Waveforms of LED driving current generated by the converter shown in Fig. 5.3.

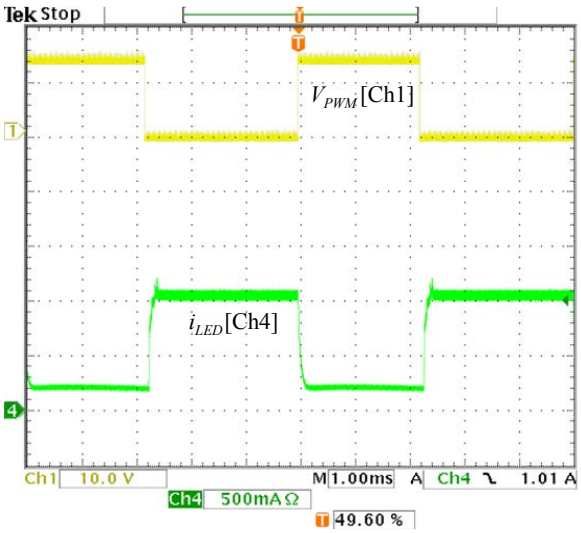

Figure 5.20: Waveforms of LED driving current generated by the converter shown in Fig. 5.3 with Q_2 being replaced by a short circuit. It is observed that i_{LED} is not zero when V_{PWM} = 1.

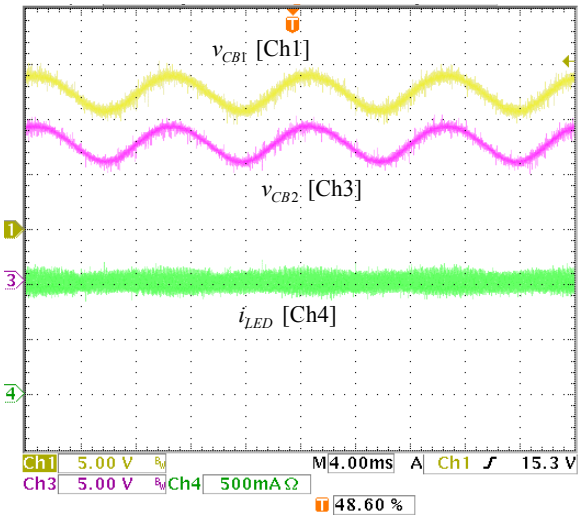

Figure 5.21: Voltage ripples of v_{CB1}, v_{CB2} and the LED driving current i_{LED}.

5.5 Summary

The efficiency and lifetime of LED lamps are approaching and expected to exceed those of fluorescent lamps. Driving the LED lamps independently from an offline power supply poses a number of design challenges, e.g., maintaining low harmonics of input current, ensuring long lifetime of power converters, and achieving precise light control and high running efficiency. Chapter 4 and this chapter present an effective LED ballast for driving multiple LED lamps independently. The first stage is an isolated PFC converter which uses low-voltage capacitors at the secondary sides to reduce cost and extend the converter lifetimes. The non-cascading structures improve the overall efficiency at nearly no cost. Analysis and design methods have been given. Experimental verifications have shown excellent agreement with theoretical predictions. In the next chapter, a low-cost transformerless converter will be developed for the retrofit of incandescent lamps.

Chapter 6

Resonant Assisted Buck Converter for Low-power Lighting Applications

6.1 Introduction

To promote energy saving, many governments in the world, such as United States, European Union and Australia, have implemented measures to phase out energy inefficient incandescent light bulbs. Energy efficient LED lamps in a PAR30 style housing can be direct replacements of the incandescent light bulbs.

In Chapters 4 and 5, LED ballasts of various power levels for the independent brightness control are illustrated. The ballasts use high-frequency step-down transformers and associated soft-switching techniques to achieve the required step-down ratio. The designs allow low-voltage capacitors having long lifetime to be used in the secondaries of the transformer, matching the life expectancy of LEDs. The designs also utilize two non-cascaded structures for efficiency improving. In this chapter, the same objectives of long lifetime and efficiency optimization will be used to design the LED replacement lamp.

LED lamps are prospective successors of incandescent lamps with much higher efficacy of about 90 lm/W and 75 lm/W for cool and warm white LEDs respectively as listed in Table 1.1 in Chapter 1. Compared with incandescent lamps, LED replacement lamps in a PAR30 style housing are expected to have more than 80 % energy saving and much longer lifetime. Earlier energy-saving lamps for home applications do not work properly with the existing dimmer switches. To gain the public acceptance, the LED replacement lamp should be designed to work with dimmer switches, such as conventional leading-edge dimmers or trailing-edge MOSFET dimmers.

To produce 1000 lm (typical luminance flux from a 60 W incandescent lamp), approximately 12 LEDs of 1 W each are needed to be integrated into a PAR30 style housing. Here, we use high flux white LED, XREWHT-L1-0000-00C02 from Cree, Inc. The LED has luminous efficacy of 100 lm/W driven by a current of 350 mA at a junction temperature T_j of 25 °C [128]. The 12 LEDs are configured in parallel with two branches of 6 LEDs each in series. Therefore, the LED ballast should provide an output current of 700 mA at a typical loading voltage of approximately (3.3×6 =) 19.8 V at T_j of 25 °C from a universal line voltage of 100 to 240 Vrms. For such a high-voltage step-down ratio, a transformer is usually used. However, such a transformer has large leakage inductance whose energy needs to be re-cycled or dissipated properly. Otherwise the energy will appear as voltage or current stress to the devices connected, complicating the ballast design or reducing the converter efficiency. Consequently, transformerless design can be more attractive, especially in the low power and cost effective applications.

The traditional PWM single-switch buck converter is among the most efficient transformerless step-down converters. However, to provide power factor correction, the buck converter operating in CCM normally requires an averaged current controller with considerable cost. Such averaged current programmed power converters are mostly not compatible with existing dimmer switches, re-

ducing the popularity of the replacement lamps built. The CCM buck converter may also suffer from loss caused by the high reverse recovery current of the high-voltage freewheel diode. On the contrary, the buck converter operating in DCM is input resistive with the simple duty cycle control, providing the natural power factor correction. As the freewheeling diode turns off naturally, the diode recovery current does not exist ensuring high efficiency.

A small LC line filter in front of the buck converter can provide enough filtration of the high frequency switching current ripples operating in either CCM or DCM, meeting the requirements of current harmonics limitation as specified in EN 61000-3-2 Class C in Table 2.1 in Chapter 2 for ballasts below 25 W. However, the output switching ripple current of DCM operated buck converter flowing into the charge storage capacitor is several times that in CCM. It will reduce the lifetime of the capacitor, as well as the lifetime of the replacement lamp.

In this chapter, a high-step-down-ratio and high-efficiency resonant assisted buck converter for low-power and cost effective LED replacement lamps is proposed to achieve the design objectives of long lifetime and efficiency optimization mentioned above. Section 6.2 introduces the characteristics of the converter. The detailed analysis and implementation of the converter are given in Section 6.3. The performance of the proposed LED driver system is evaluated in Section 6.4. Section 6.5 concludes this chapter.

6.2 Overview of the Resonant Assisted Buck Converter

The buck converter operating in discontinuous conduction mode is input resistive with the simple duty cycle control, providing the natural power factor correction. The buck converter operating in continuous conduction mode can

provide a continuous driving current that reduces the current stress on the charge storage capacitor and thereby extends its lifetime. Using two buck converters connected in cascade as shown in Fig. 6.1 can provide power factor correction and reduce switching current ripple to the charge storage capacitor. However a two-stage design is less efficient.

Figure 6.2 (a) shows the high-step-down-ratio resonant assisted buck converter. The idea is to eliminate switch S_2 in Fig. 6.1, thus we can reclaim the switching and conduction loss due to S_2. To synthesize the functionality of S_2, L_1 and C_1 are designed near resonant with the resonant frequency several times higher than the switching frequency. The switch S_1 is turned on for a duration of dT. Typical waveforms of the converter are illustrated in Fig. 6.3. The diode D_1 clamps the current i_{L_1} of L_1 at a single direction, forcing it to operate at discontinuous current mode. Likewise, the voltage v_1 is clamped by D_2 to form a sequence of half-sine waveforms. The second stage is an ordinary buck converter consisting of D_2, L_2, C_2 and the LED lamp. Consequently, the resonant frequency $\frac{1}{2\pi\sqrt{L_2C_2}}$ is designed to be much lower than the frequency of v_1, i.e. the switching frequency $f_S = \frac{1}{T}$ of S_1. Essentially, the current i_{L_2} can be approximated as a current source loading to the first stage circuit, as shown in Fig. 6.2 (b). The volt-second of v_1 in Fig. 6.2 (c) can be used to calculate the steady-state current i_{L_2} and I_{LED}.

6.3 Analysis and Implementation

The proposed circuit in Fig. 6.2 (a) will drive LEDs directly from universal mains with an input line filter consisting of L_f and C_f. Both the dynamics at the switching frequency and the line frequency are important for designing the converter. We will formulate the states of operation at switching frequency in the next subsection. The information obtained will be used subsequently to design converters for offline applications.

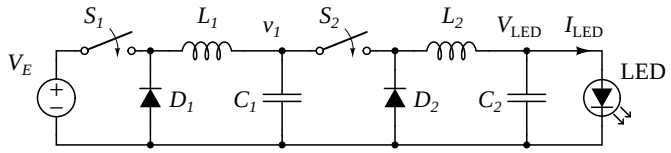

Figure 6.1: Two buck converters cascade together to drive an LED lamp.

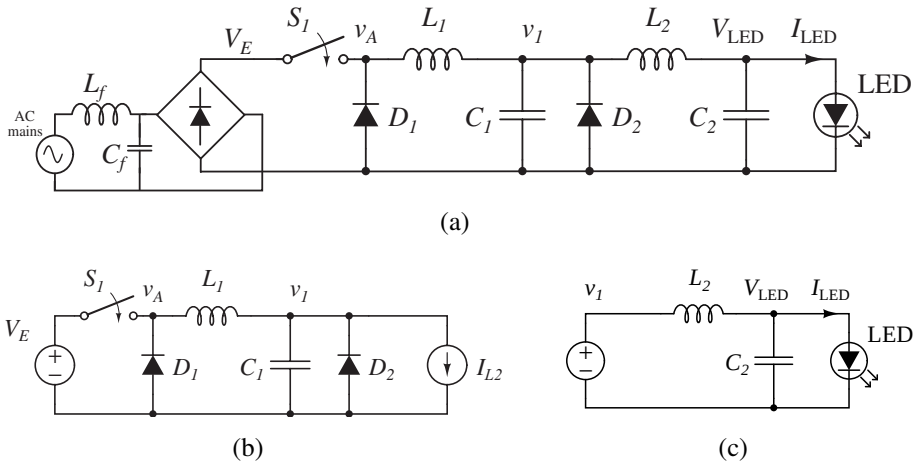

Figure 6.2: High-step-down-ratio resonant assisted buck converter. (a) The converter circuit. (b) Circuit model for the input stage. (c) Circuit model for the output stage.

6.3.1 Operation Near Switching Frequency

The operation of the proposed converter has been highlighted in the last section. In this section, the detailed operation of the converter will be described. As shown in Fig. 6.3, there are four main states of operation within a switching cycle. State 1 is the duration when S_1 turns on. The inductor current i_{L_1} reaching zero marks the end of state 2. The capacitor voltage v_1 reaching zero marks the end of state 3. The remaining time of the switching cycle is defined as state 4. For simplicity, we assume S_1, D_1 and D_2 being ideal switches. The system of equations is formulated as follows.

1) **State 1** At the beginning of a switching cycle, because of discontinuous operations of L_1 and C_1, we have $i_{L_1} = 0$ and $v_{C_1} = 0$. The continuous operation

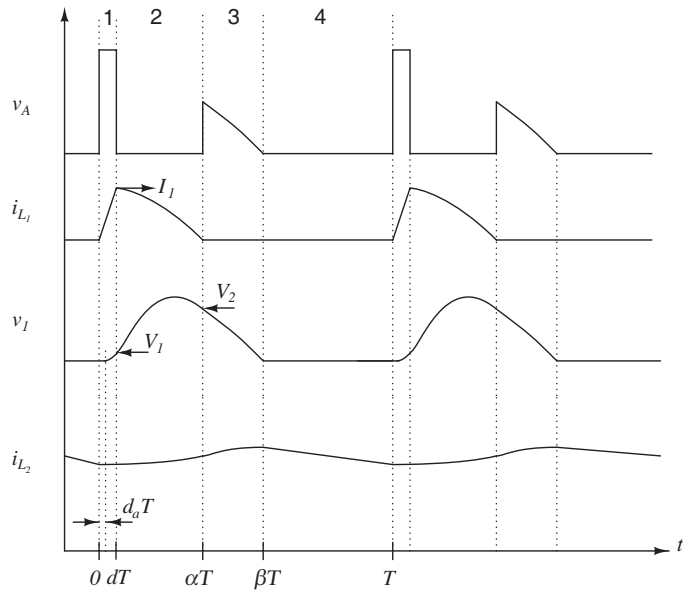

Figure 6.3: Illustrative waveforms of the high-step-down-ratio resonant assisted buck converter shown in 6.2 (a).

of L_2 forces D_2 to conduct. After S_1 turns on, the inductor current i_{L_1} starts to rise linearly until it reaches i_{L_2}, or S_1 turns off. If S_1 stays on, L_1 starts to resonate with C_1, making its current less linear. State 1 is therefore subdivided into state 1a and state 1b, formulated as (6.1) and (6.2) respectively.

$$\begin{cases} \textbf{state 1a: } 0 < t \leq d_aT \\ \quad i_{L_1}(0) = 0 \\ \quad v_1(0) = 0 \\ i_{L_1}(d_aT) = \begin{cases} I_a < i_{L_2}(d_aT) & \text{if } d_a = d \\ i_{L_2}(d_aT) & \text{if } d_a < d \end{cases} \\ \quad v_1(t) = 0 \\ \dfrac{\mathsf{d}i_{L_1}(t)}{\mathsf{d}t} = \dfrac{V_E}{L_1} \end{cases} \tag{6.1}$$

$$\begin{cases} \textbf{state 1b: } d_aT < t \leq dT \\ i_{L_1}(d_aT) = i_{L_2}(d_aT) \\ v_1(d_aT) = 0 \\ i_{L_1}(dT) = I_1 \\ v_1(dT) = V_1 \\ \dfrac{\mathsf{d}i_{L_1}(t)}{\mathsf{d}t} = \dfrac{V_E - v_1(t)}{L_1} \\ \dfrac{\mathsf{d}v_1(t)}{\mathsf{d}t} = \dfrac{i_{L_1}(t) - i_{L_2}(t)}{C_1} \end{cases} \tag{6.2}$$

2) **State 2** After S_1 turns off, L_1 and C_1 resonate until $i_{L_1} = 0$. When $i_{L_1} = 0$, diode D_1 turns off, preventing i_{L_1} from flowing in reverse direction. The voltage v_A is equal to v_1, as indicated in Fig. 6.3. The system of equations of state 2 is formulated as follows.

$$\begin{cases} \textbf{state 2: } dT < t \leq \alpha T \\ i_{L_1}(dT) = I_1 \\ v_1(dT) = V_1 \\ i_{L_1}(\alpha T) = 0 \\ v_1(\alpha T) = V_2 \\ \dfrac{\mathsf{d}i_{L_1}(t)}{\mathsf{d}t} = \dfrac{-v_1(t)}{L_1} \\ \dfrac{\mathsf{d}v_1(t)}{\mathsf{d}t} = \dfrac{i_{L_1}(t) - i_{L_2}(t)}{C_1} \end{cases} \tag{6.3}$$

3) **State 3** After $i_{L_1} = 0$, capacitor voltage v_1 is continuously discharged by i_{L_2} until it reaches zero. The voltage v_1 is kept at zero because i_{L_2} turns on D_2

just after $v_1 = 0$. The system of equations of state 3 is formulated as follows.

$$\begin{cases} \textbf{state 3: } \alpha T < t \leq \beta T \\ \quad i_{L_1}(t) = 0 \\ v_1(\alpha T) = V_2 \\ v_1(\beta T) = 0 \\ \quad \dfrac{\mathsf{d}v_1(t)}{\mathsf{d}t} = \dfrac{-I_{L_2}}{C_1} \end{cases} \tag{6.4}$$

4) **State 4** The voltage v_1 is kept at zero because i_{L_2} turns on D_2 just after $v_1 = 0$. The system of equations of state 4 is formulated as follows.

$$\begin{cases} \textbf{state 4: } \beta T < t \leq T \\ \quad i_{L_1}(t) = 0 \\ \quad v_1(t) = 0 \end{cases} \tag{6.5}$$

The inductance L_2 is designed to be relatively large for the small current ripple in driving the LED strings. Due to the small current ripple of i_{L_2}, we may assume that $i_{L_2}(t) \approx \overline{i_{L_2}(t)} = I_{L_2}$. I_{L_2} varies slowly relative to the time scale of the switching frequency. Therefore, it can be assumed constant at the time scale of T. Solving (6.1) and (6.2), we obtain $I_1(d)$ and $V_1(d)$ in (6.6) and (6.7) respectively.

$$I_1(d) = \begin{cases} \dfrac{V_E dT}{L_1} & \text{if } d_a \geq d \\ I_{L_2} + \dfrac{V_E}{Z_r} \sin \omega_r (d - d_a) T & \text{if } d_a < d \end{cases} \tag{6.6}$$

$$V_1(d) = \begin{cases} 0 & \text{if } d_a \geq d \\ V_E \big[1 - \cos \omega_r (d - d_a) T \big] & \text{if } d_a < d \end{cases} \tag{6.7}$$

where

$$d_a = \frac{I_{L_2} L_1}{V_E T}, \tag{6.8}$$

$$\omega_r = \sqrt{\frac{1}{L_1 C_1}}, \text{ and} \tag{6.9}$$

$$Z_r = \sqrt{\frac{L_1}{C_1}}. \tag{6.10}$$

For high-voltage-step-down applications, $\omega_r(d - d_a)T$ is small. Using the approximation of $\lim_{x\to 0} \sin x \approx x$, (6.6) can be simplified to

$$I_1(d) \approx \frac{V_E dT}{L_1}. \tag{6.11}$$

The input power to the power converter can therefore be calculated as

$$P_{\text{IN}} = \frac{1}{T}\int_0^{dT} V_E i_{L_1} \mathrm{d}t \approx \frac{T}{2L_1}(dV_E)^2 \tag{6.12}$$

Solving (6.3), we obtain the following equations for state 2

$$i_{L_1}(t + dT) = (I_1 - I_{L_2})\cos\omega_r t + I_{L_2} - \frac{V_1}{Z_r}\sin\omega_r t, \text{ and} \tag{6.13}$$

$$v_1(t + dT) = V_1 \cos\omega_r t + (I_1 - I_{L_2}) Z_r \sin\omega_r t. \tag{6.14}$$

In (6.13) and (6.14), the dependency of I_1 and V_1 on d are not indicated for clarity. Rearranging, we get

$$i_{L_1}(t + dT) = A\cos(\omega_r t + \sigma) + I_{L_2}, \text{ and} \tag{6.15}$$

$$v_1(t + dT) = AZ_r \sin(\omega_r t + \sigma), \tag{6.16}$$

where

$$A = \sqrt{(I_1 - I_{L_2})^2 + (V_1/Z_r)^2}, \text{ and} \tag{6.17}$$

$$\sigma = \tan^{-1} \frac{V_1/Z_r}{I_1 - I_{L_2}}. \tag{6.18}$$

Putting the right hand side of (6.13) to zero, the boundaries of state 2 are obtained as

$$\alpha = d + \frac{\theta - \sigma}{\omega_r T}, \text{ and} \tag{6.19}$$

$$V_2 = \sqrt{I_1(I_1 - 2I_{L_2})Z_r^2 + V_1^2}, \tag{6.20}$$

where

$$\theta = \cos^{-1} \frac{-I_{L_2}}{A}. \tag{6.21}$$

In order that (6.20) has a solution, the following design constraint can be imposed

$$I_1 - 2I_{L_2} \geq 0. \tag{6.22}$$

To reduce the conduction time of D_1, α can be made small by using a higher ω_r. Solving (6.4), we have

$$\beta = \frac{V_2 C_1}{I_{L_2} T} + \alpha. \tag{6.23}$$

If $V_2 = 0$, we have $\beta = \alpha$, where i_{L_1} and v_1 reach zero at the same time.

6.3.2 Converter Design for Line Frequency Operation

The converter is controlled by the duty cycle d for the automatic power factor correction. The input line voltage can be described as

$$v_{\text{in}}(t) = V_m \sin \omega_l t \tag{6.24}$$

Thus, the instantaneous input power over a line cycle of angular frequency ω_l is given from (6.12) as

$$P_{\text{IN}}(t) = \frac{T}{2L_1}(dV_m)^2 \sin^2 \omega_l t \tag{6.25}$$

The output voltage V_{LED} is being held up by the charge storage capacitor C_2. We may therefore assume V_{LED} being constant. From power balance and (6.25), we have

$$\begin{aligned} I_{L_2}(t) &= \frac{P_{\text{OUT}}}{V_{\text{LED}}} = \frac{P_{\text{IN}}}{V_{\text{LED}}} \\ &= \frac{T}{2L_1 V_{\text{LED}}}(dV_m)^2 \sin^2 \omega_l t \\ &= \frac{T}{4L_1 V_{\text{LED}}}(dV_m)^2 (1 - \cos 2\omega_l t) \end{aligned} \tag{6.26}$$

The average of I_{L_2} over a line cycle gives I_{LED}. Hence,

$$I_{\text{LED}} = \overline{I_{L_2}(t)} = \frac{I_{L_2,\max}}{2} = \frac{T}{4L_1 V_{\text{LED}}}(dV_m)^2 \tag{6.27}$$

6.3.3 Design Procedures and Implementation of the Converter

Based on the line and switching frequency analysis in Sections 6.3.1 and 6.3.2, the design procedures of the converter are given as follows.

1. Denote I_{LED} as the rated DC current of the LEDs.

2. $I_{L_2,\max}$ is determined as $2I_{\mathrm{LED}}$ from (6.27).

3. To make sure that L_1 operates in DCM, $d \leq \frac{V_{\mathrm{LED}}}{v_{\mathrm{in,max}}}$. The maximum duty cycle $d_{\max}$ is given as $d_{\max} = \frac{V_{\mathrm{LED}}}{V_{m,\min}}$.

4. L_1 is determined using $L_1 = \frac{T}{4V_{\mathrm{LED}}I_{\mathrm{LED}}}(d_{\max}V_{m,\min})^2$ from (6.27). To ensure DCM, L_1 should be smaller than this value.

5. C_1 is determined from $f_r \leq f_s$, where f_r is given by (6.9). So $C_1 \geq (\frac{T}{2\pi})^2\frac{1}{L_1}$.

6. The maximum of v_1 should occur during state 2 in a switching period. From (6.16), $v_1 = \sqrt{V_1^2 + (I_1 - I_{L_2})^2 Z_r^2}$ and assuming relatively small V_1, we get

$$v_{1,\max} \approx (I_1 - I_{L_2})Z_r \tag{6.28}$$

   where I_1 is given in (6.6). $v_{1,\max}$ occurs at maximum v_{in} such that I_{L_2} equals $2I_{\mathrm{LED}}$.

7. L_2 can be determined using its allowable peak-to-peak current ripples Δi_{L2}. From Fig. 6.2(c), we have

$$L_2\frac{di_{L2}}{dt} = \begin{cases} v_{1,\max}\sin\omega_r t - V_{\mathrm{LED}} & dT < t \leq \alpha T \\ V_2 - \frac{I_{L2}}{C_1}t - V_{\mathrm{LED}} & \alpha T < t \leq \beta T \end{cases} \tag{6.29}$$

   where α, β and V_2 are calculated using (6.19), (6.23) and (6.20) respectively.

   Integrating (6.29) gives

$$\begin{aligned} L_2 = {} & \frac{1}{\Delta i_{L2}}\left[\frac{v_{1,\max}}{\omega_r}\left(\cos\omega_r T_0 - \cos\omega_r(\alpha - d)T\right) - V_{\mathrm{LED}}\left((\alpha - d)T - T_0\right)\right] \\ & + \frac{1}{\Delta i_{L2}}\left(V_2 T_1 - \frac{I_{L2}T_1^2}{2C_1} - V_{\mathrm{LED}}T_1\right) \end{aligned} \tag{6.30}$$

where $T_0 = \frac{1}{\omega_r} \sin^{-1} \frac{V_{\rm LED}}{v_{1,\max}}$ and $T_1 = \frac{V_2 - V_{\rm LED}}{V_2}(\beta - \alpha)T$.

8. C_2 is obtained using its allowable peak-to-peak voltage ripple ΔV_{C2} from power balance between the input and the output for half of a line period. From (6.26) and (6.27), $I_{C_2}(t) = I_{L_2}(t) - I_{\rm LED}$. Integrating $I_{C_2}(t)$ for half a line period, we have

$$C_2 = \frac{P_{\rm OUT}}{4\pi f_l V_{\rm LED} \Delta V_{C2}} \tag{6.31}$$

6.4 Experimental Evaluation

A prototype converter shown in Fig. 6.2 (a) has been constructed for performance evaluations. For the rated power output of 19.8 V$\times$ 0.7 A = 13.72 W, L_1 is chosen as 70 μH using design procedures 1 to 4 described in the last section. The corresponding maximum duty cycle is 0.105 at 100 Vrms AC line input. The switching frequency is designed at 56 kHz to reduce the switching loss at part load [129]. Most PWM IC chips do not provide PWM signals of adequate accuracy near a duty cycle of 0.1. To generate the required PWM signals efficiently, the switching frequency is quartered from a 230 kHz PWM generator using D flip-flops, effectively generating duty cycle from 0 to 0.25 at 56 kHz. Using the design procedure 5, C_1 should be larger than 115 nF. From (6.28), $v_{1,\max}$ = 58.6 V. To have $\frac{\Delta i_{L_2}}{I_{L_2}} = 20$ %, L_2 is detemined as 649 μH using (6.30). Fig. 6.4 gives the value of L_2 varying with C_1 at a current ripple level of $\frac{\Delta i_{L_2}}{I_{L_2}} = 20$ %. With the same ripple current, larger C_1, corresponding with smaller L_2, will make D_1 conduct more and D_2 conduct less as indicated in (6.19) and (6.23) respectively. In practice, the voltage rating of D_2 should be above $v_{1,\max}$, Schottky diodes with a low forward voltage smaller than 0.5 V can be used. While the voltage rating of D_1 is the maximum amplitude of the input AC voltage, an ordinary silicon diode for D_1 having the forward voltage of about 1 V is used. Fig. 6.5 illustrates the

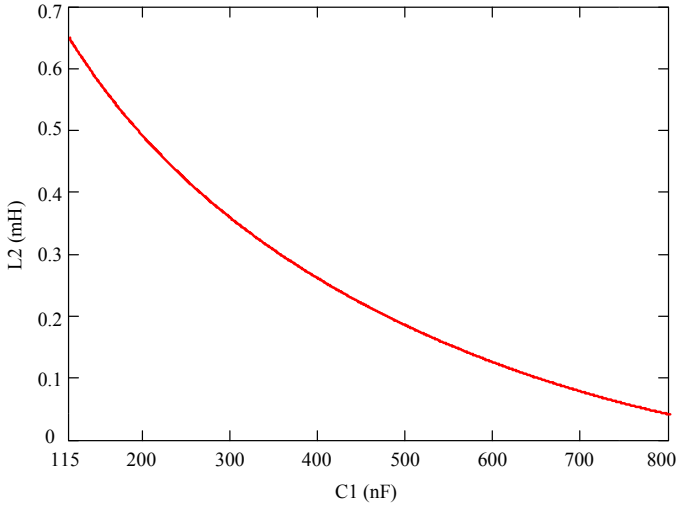

Figure 6.4: L_2 as a function of C_1, giving current ripple level of $\frac{\Delta i_{L_2}}{I_{L_2}} = 20$ %.

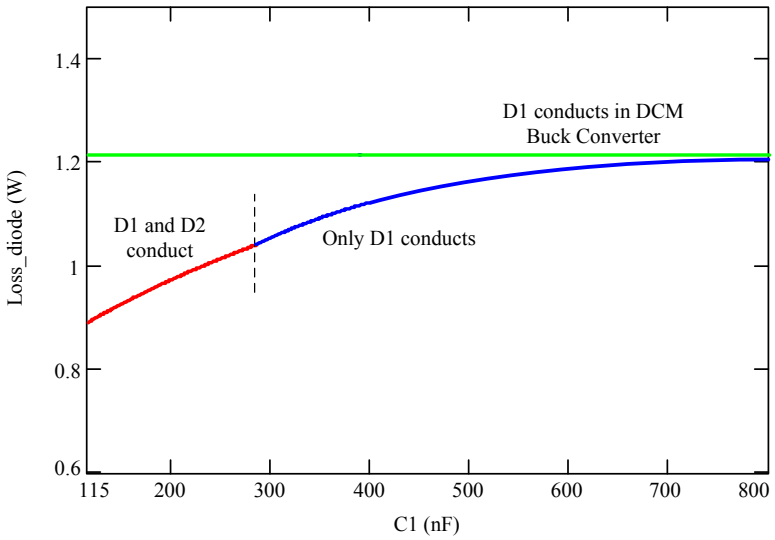

Figure 6.5: Power loss in diodes at output current ripple level of $\frac{\Delta i_{L_2}}{I_{L_2}} = 20$ %.

calculated power loss distributed on diodes at the peak voltage of 141 V of the AC main. When C_1 is smaller than 291 nF, D_1 and D_2 conduct together. Due to the lower conduction voltage of the Schottky diode D_2, the loss in the diodes is smaller with smaller C_1. Fig. 6.6 gives the experimentally measured efficiency versus the capacitance of C_1 with L_2 given by Fig. 6.4. Hence, to improve the efficiency, large L_2 and small C_1 are selected. Here, we use C_1 of 220 nF and L_2 of 457 μH. C_2 is 1500 μF to ensure less than 10 % voltage ripple feeding on

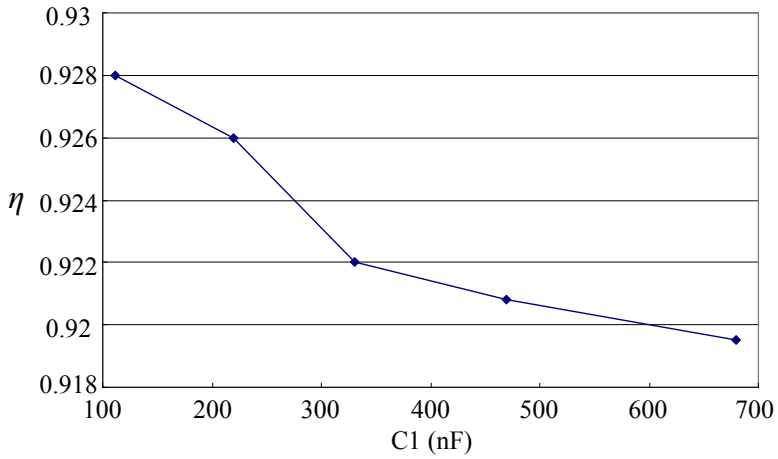

Figure 6.6: Efficiency of converter with different values of C_1 at 100 Vrms AC input with output current ripple level of $\frac{\Delta i_{L_2}}{I_{L_2}} = 20\ \%$.

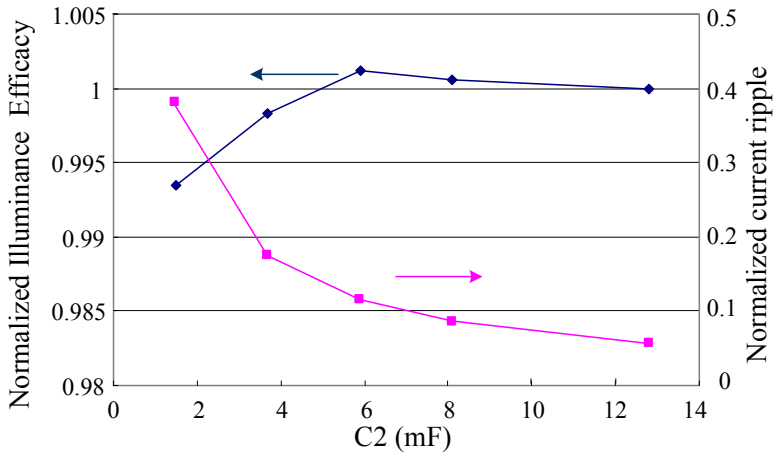

Figure 6.7: Normalized illuminance efficacy and corresponding current ripple versus different values of C_2.

the LED load. As analyzed in Section 6.2, a 63 V rated Vishay capacitor of C_2 is used. Long-lifetime polyester film or ceramic capacitors can be used for C_1. D_1 is Fairchild ultra-fast diode MUR860. D_2 is IR Schottky diode MBR20100CT.

Fig. 6.8 shows the experimental waveforms of v_{in}, i_{in}, V_{LED} and I_{LED} for 100 V and 240 Vrms AC input, respectively, where i_{in} is the line current observed in front of a line filter consisting of $L_f = 300\ \mu$H and $C_f = 220$ nF. LED load is two parallel branches of 6 cool white Cree LEDs connected in series. Power

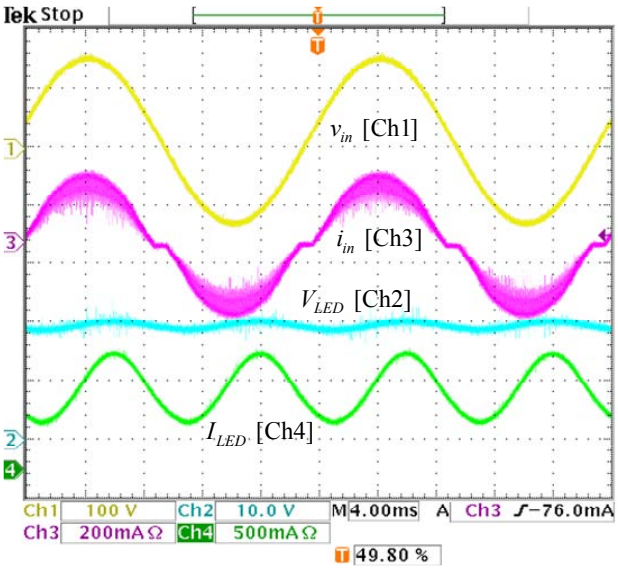

(a)

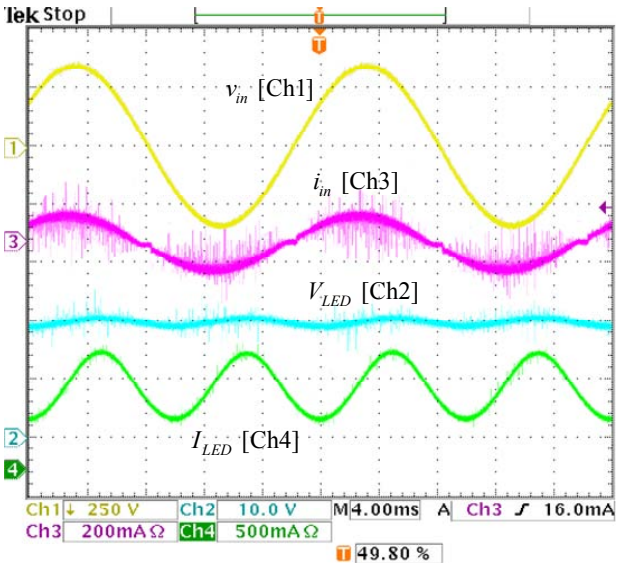

(b)

Figure 6.8: Experimental waveforms of $v_{\rm in}$, $i_{\rm in}$, $V_{\rm LED}$ and $I_{\rm LED}$ at two line input voltages. (a) 100 Vrms AC input. (b) 240 Vrms AC input.

factor is measured to be 0.996 and 0.988 for the two line voltages respectively. Note that the voltage ripple is about 10 % of $V_{\rm LED}$. The current ripple is measured to be as high as 270 mA for $I_{\rm LED} = 700$ mA. Fig. 6.7 illustrates the normalized illuminance efficacy (Lux/W) versus C_2, showing very little impact of current ripples on illuminance efficacy. Fig. 6.9 gives the waveforms of v_A, v_1, i_{L_1} and

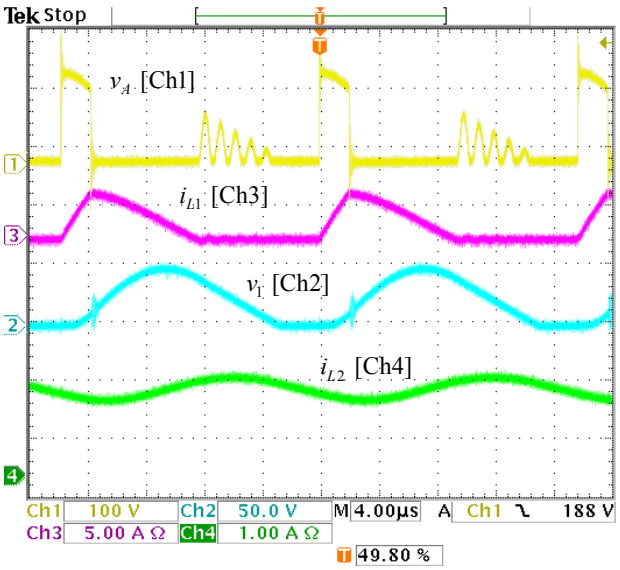

(a)

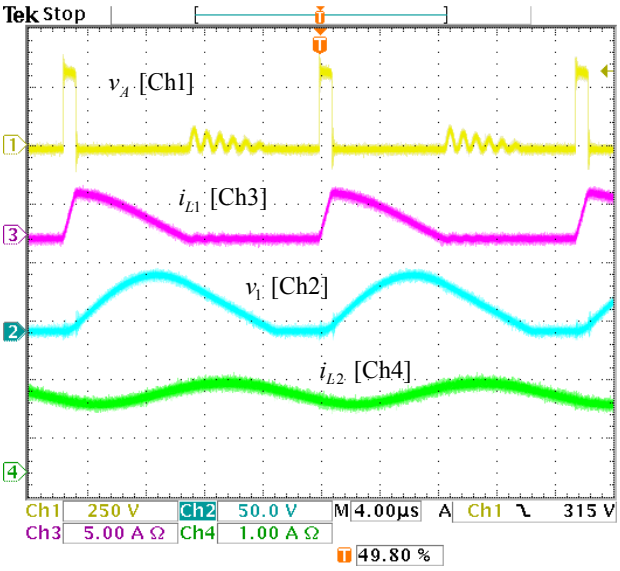

(b)

Figure 6.9: Experimental waveforms of v_A, v_1, i_{L_1} and i_{L_2} at two peaks of input voltage. (a) 141 V (peak of 100 Vrms line input). (b) 339 V (peak of 240 Vrms line input).

i_{L_2} at the peak of 100 and 240 Vrms inputs. The small i_{L_2} switching ripples guarantee the longer lifetime of the output capacitor C_2. The efficiency shown in Fig. 6.10 is typical for low-current applications where switching loss becomes relatively high with the higher input voltage.

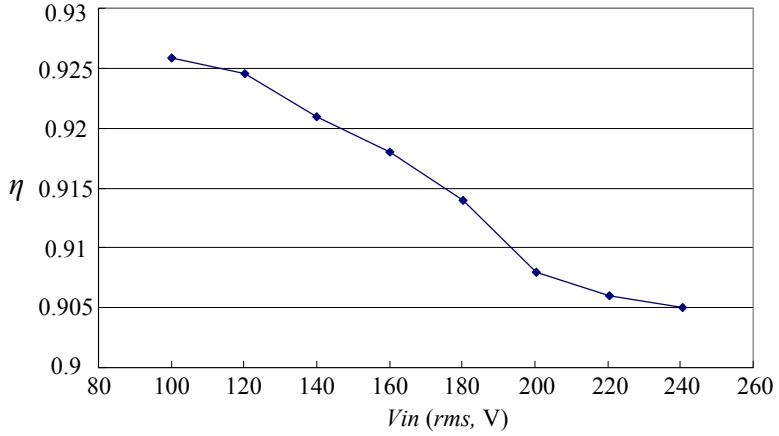

Figure 6.10: Converter efficiency versus line input voltage at rated power.

Fig. 6.11 gives two sets of experimental waveforms of the rectified voltage $v_{\rm rec}$ after the bridge rectifier, v_1, i_{L_2} and $I_{\rm LED}$ when the LEDs are dimmed at 100 V rms AC input using trailing edge control. Fig. 6.11(a) uses $C_1 = 220$ nF and $L_2 = 457$ μH. Fig. 6.11(b) uses $C_1 = 470$ nF and $L_2 = 204$ μH. The values of C_1 and L_2 follow Fig. 6.4. Obviously, Fig. 6.11(b) shows more ringings in L_2 just after turning off of $v_{\rm rec}$ by the dimmer. The measured efficiencies are 90.56 $\%$ and 89.69 $\%$ for Figs. 6.11(a) and (b) respectively, showing better efficiency of using smaller C_1.

6.5 Summary

A high-step-down-ratio high-efficiency transformerless resonant assisted buck converter for LED lamps is proposed for applications of incandescent lamp retrofits. The discontinuous-conduction-mode operation of the inductor current allows the simple duty cycle control to achieve both power factor correction and dimmer device compatibility. Optimization with a resonant assisted filter eliminates the switching frequency current ripples to the output charge hold-up capacitor, extending its lifetime. Thus low-cost high-density electrolytic capacitor can be used in LEDs lighting applications with lifetimes comparable with those of LEDs. The

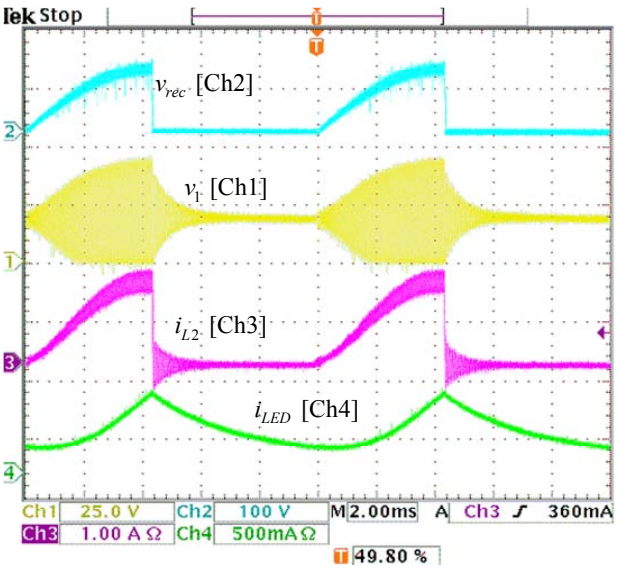

(a)

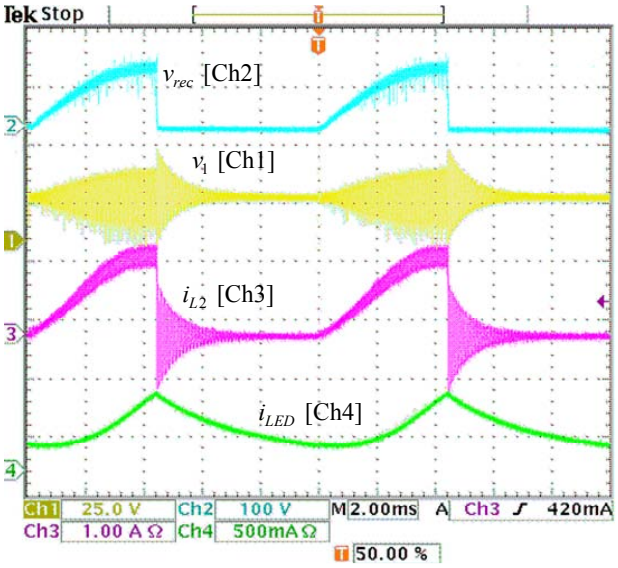

(b)

Figure 6.11: Converter waveforms v_1, i_{L_2} and i_{LED} dimmed by v_{rec} using trailing edge control at the same output ripple current of 20 %. (a) $C_1 = 220$ nF and $L_2 = 457$ μH. (b) $C_1 = 470$ nF and $L_2 = 204$ μH.

resonant assisted filter also allows using the low-forward-voltage Schottky diode to improve the converter efficiency. Theoretical calculation and design procedures have been presented for the converter. Experimental verifications have shown excellent agreement with theoretical predictions.

Chapter 7

Conclusion

In this concluding chapter, we summarize the findings that have been accomplished in this project. Some possible future work and potential areas for further development are also presented.

7.1 Contributions of the Thesis

LED lamps are praised as green lamps in the light of their green properties, such as energy saving, mercury free, long durability, UV and IR radiation free. These merits are attracting more attention to LED lighting applications in the industry. In this thesis, through the studies of color maintenance and LED ballasts, comprehensive guidelines are provided for designing appropriate LED systems. Specifically, the contributions of the thesis are stated as follows.

1. Chapter 3 investigates color control methods and analyzes the nonlinear effects of junction temperature to color precision. A temperature compensation technique using the LED turn-on voltage during the on-state of a PWM period has been proposed. The technique can control the color ef-

fectively, dramatically reduce the complexity, and eliminate the need for using expensive feedback systems involving lighting sensors. The system has been ported to a fully automatic computerized system for industrial implementation.

2. Chapter 4 proposes a transformer isolated boost PFC pre-regulator operating in discontinuous conduction mode for LED ballasts in order to satisfy the current harmonic limits and achieve high voltage step-down. The pre-regulator uses the resonant technique to take advantage of the leakage inductance commonly found in high voltage step-down transformers. The resonant circuit allows the output charge storage capacitor to be placed at the secondary of the transformer. In this way, the short-lifetime high-voltage charge storage capacitor is no longer required. Instead, a low-voltage long-lifetime capacitor can be used to extend the overall system lifetime. The resonance structure also takes full advantage of the leakage inductance of the high turns-ratio transformer to alleviate the voltage and current stresses, improving the lifetime of main switching components.

3. Chapter 5 derives the conditions for the converter in Chapter 4 to be operated in continuous conduction mode for high power applications. This chapter also presents a non-cascading configuration at the secondary of the PFC pre-regulator to improve the overall efficiency via two output windings of the transformer. One of the outputs is connected directly (without being processed) in series with the other output which is then current regulated by a PWM buck converter to drive an LED lamp. Since the energy from one output winding can directly be used to drive the LED without going through another power stage, a higher efficiency can be guaranteed. A detailed design and optimization procedures are given and the results are verified by experiments.

4. Finally, in applications with power lower than 25 W, the current harmonic requirements are less stringent as stated in some international standards. A

high-step-down-ratio and high-efficiency resonant assisted buck converter for LED lamps is proposed in Chapter 6 for the application of incandescent replacement lamps. The transformerless design boosts the converter efficiency. The discontinuous conduction mode operation allows simple duty cycle control and is compatible with dimmer devices.

7.2 Suggestions for Future Work

The unique features of LEDs arouse great concern and interest of academia and industry in lighting applications. Based on the previous work and experience gathered in the recent decade, and the work done in this project, suggestions for extensions and potential areas for further studies are proposed here.

PWM of the LED driving current and measurement of the LED diode forward voltage have been used for light color maintenance in Chapter 3. Investigation of other current modulation methods is an interesting topic to study. The use of PWM current driving provides predictable relationship between duty cycle and light intensity with minimum alteration of other light properties. However, the PWM dimming technique may have poor efficacy when the LED is driven at some high current levels where the optical light output becomes saturated. In such applications where the LEDs are driven near saturation for optimization of the total achievable output lumen, dimming by AM will be a better alternative to achieve a higher luminous efficacy. However, it is predicted that the AM dimming for color maintenance can be complicated. The kinds of relationships that exist among the electrical-thermal-optical behavior remain unknown. With the boost in digital-signal-processor (DSP) programming powers, the compensation may be achievable even if complex computations are involved.

For a LED having 75 lm/W, about 90 % of its electrical energy will be converted to heat. Almost 90 % of the heat generated is not radiative and needs to be

removed conductively. Thermal management of the LED light source becomes an important issue for LED lighting applications in order to keep the LED below its operating temperature. Otherwise its light output may be reduced and chip degradation accelerated. Thermal management components such as heat sinks, piezo fans, thermoelectric coolers, metal core PCBs and heat pipes are actively researched for LED applications. Optimization of these thermal management components specifically for LED applications can improve light output and prolong LED lifetime.

In the research of LED ballasts, we have proposed several driving circuits for different power-level applications, targeting at improving lifetime and efficiency. Other areas such as integrated magnetics and soft switching can be investigated to improve the power density and cost of LED ballasts.

For ease of thermal management, a single LED can provide about 100 lm light output. In many applications, such as those used in stadiums, high lumen flux of more than 1000 lm per lamp is needed. Several LED lamps are connected in series or parallel to provide enough brightness driven by a single ballast for cost saving. LED binning is used to overcome device variation in electrical and optical properties, but this increases the cost. Therefore, circuits for automatic current sharing or voltage sharing can be an important topic for investigation.

Bibliography

[1] BL-4000 Series datasheet, "RGB + LED light engine," *Lamina Lighting Inc.*, 2005.

[2] Atlas Series datasheet, "Atlas LED light engines datasheet," *Lamina Lighting Inc.*, 2006.

[3] X42180 datasheet, "X42180 technical data sheet," *Seoul Semiconductor Inc.*, 2009.

[4] Philips Technology white paper, "Understanding power LED lifetime analysis," *Philips Lumileds Lighting Int.*, 2007.

[5] R. Friedel and P. Israel, *Edison's Electric Light: Biography of an Invention*. New Jersey, NJ: Rutgers University Press, 1986.

[6] T. Hughes, *American Genesis: A Century of Invention and Technological Enthusiasm*. Chicago, IL: The University of Chicago Press, 1990.

[7] L. J. Davis, *Fleet Fire: Thomas Edison and the Pioneers of the Electric Revolution*. New York, NY: Arcade Publishing, 2003.

[8] J. Waymouth, *Electric Discharge Lamps*. Cambridge, MA: The MIT Press, 1971.

[9] D. O. Wharmby, "Electrodeless lamps for lighting: a review," *Proceedings of IEE Science, Measurement and Technology*, vol. 140, pp. 465–473, Nov. 1993.

[10] W. Elenbaas, *Fluorescent Lamps*. London, U.K.: Macmillan, 1971.

[11] J. A. Sigler, J. F. Crutchfield, and H. C. Wilins, *The Fluorescent Lamp*. New York, NY: McGraw-hill Book Company, 1975.

[12] K. H. Butler, *Fluorescent Lamp Phosphors: Technology and Theory*. New Jersey, NJ: Pennsylvania State University Press, 1980.

[13] W. Elenbaas, *The High Pressure Mercury Vapor Discharge*. London, U.K.: Interscience Publishers, 1951.

[14] ——, *High-Pressure Mercury Vapor Lamps and Their Applications*. Eindhoven, Netherlands: Philips Technical Library, 1965.

[15] P. Flesch, *Light and Light Sources: High-Intensity Discharge Lamps*. Berlin, Germany: Springer, 2006.

[16] A. Žukauskas, M. S. Shur, and R. Gaska, *Introduction to Solid-State Lighting*. New York, NY: Wiley, 2002.

[17] E. F. Schubert, *Light-Emitting Diodes*. London, U.K.: Cambridge University Press; 2nd edition, 2006.

[18] M. S. Shur and A. Žukauskas, *UV Solid-State Light Emitters and Detectors*. Netherlands: Kluwer, 2004.

[19] F. Richard, *Light-emitting Diodes: A Guide to the Technology and its Applications*. Bracknell, UK: BSRIA, 2005.

[20] G. Held, *Introduction to Light Emitting Diode Technology and Applications*. London, U.K.: Taylor and Francis; 1st edition, 2008.

[21] P. Mottier, *LED for Lighting Applications*. New York, NY: Wiley-ISTE, 2009.

[22] Department of Energy, U.S. [Online]. Available: http://www.energy.gov/

[23] C. DiLouie, *Advanced Lighting Controls: Energy Savings, Productivity, Technology and Applications*. Lilburn, GA: The Fairmont Press; 1st edition, 2005.

[24] D. Derbyshire, "Revolt! robbed of their right to buy traditional light bulbs, millions are clearing shelves of last supplies," *The Daily Mail*, 2009.

[25] (2008) Grosses lichterlöschen für die glühbirnen. [Online]. Available: http://www.tagesanzeiger.ch/leben/rat-und-tipps/Grosses-Lichterlschen-fr-die-Glhbirnen/story/25999013

[26] (2009) Desde 2011, no podrán venderse más lámparas incandescentes. [Online]. Available: http://www.lanacion.com.ar/nota.asp?nota$_$id=1091978

[27] L. Cockcroft, "Traditional light bulbs to be phased out in favour of low-energy alternative," *The Daily Telegraph*, 2009.

[28] B. Tenille, "Critics blast environment plan as out of sync with science," *The Globe and Mail*, 2007.

[29] (2007) Oida market forecast for solid stage lighting. [Online]. Available: http://wrtassoc.com/

[30] S. Nakamura and G. Fasol, *The Blue Laser Diode:* G*a*N *Based Light Emitters and Lasers*. Berlin, Germany: Springer-Verlag, 1997.

[31] S. Nakamura and S. F. Chichibu, *Introduction to Nitride Semiconductor Blue Lasers and Light Emitting Diodes*. London, U.K.: Taylor and Francis, 2000.

[32] J. Kalinowski, *Organic Light-Emitting Diodes: Principles, Characteristics and Processes*, New York, NY, 2004.

[33] J. Edmond, A. Abare, M. Bergman, J. Bharathan, and *et al.*, "High efficiency GaN-based LEDs and lasers on SiC," *Journal of Crystal Growth*, vol. 272, pp. 242–250, Nov. 2004.

[34] B. Johnstone, *Brilliant*!*: Shuji Nakamura and the Revolution in Lighting Technology*. New York, NY: Prometheus Books, 2007.

[35] N. Holonyak, Jr., "Is the light emitting diode (LED) an ultimate lamp?," *American Journal of Physics*, vol. 68, no. 9, pp. 864–866, Sep. 2000.

[36] J. Tsao, "Solid-state lighting: lamps, chips and materials for tomorrow," in *Proceedings of Conference on Lasers and Electro-Optics (CLEO)*, May 2005, pp. 143–143.

[37] Y. Narukawa, J. Narita, T. Sakamoto, K. Deguchi, T. Yamada, and T. Mukai, "Ultra-high efficiency white light-emitting diodes," *Japanese Journal of Applied Physics*, vol. 45, pp. L1084–L1086, Oct. 2006.

[38] M. R. Krames, O. B. Shchekin, R. Mueller-Mach, G. O. Mueller, L. Zhou, G. Harbers, and M. G. Craford, "Status and future of high-power light-emitting diodes for solid-state lighting," *IEEE/OSA Journal of Display Technology*, vol. 3, no. 2, pp. 160–175, Jun. 2007.

[39] (2009) Renewables global states report 2009 update. [Online]. Available: http://www.ren21.net/pdf/RE$_$GSR$_$2009$_$Update.pdf

[40] M. S. Shur and A. Žukauskas, "Solid-state lighting: toward superior illumination," *Proceedings of IEEE*, vol. 93, no. 10, pp. 1691–1703, Oct. 2005.

[41] C. C. Chen, C. Y. Wu, and T. F. Wu, "LED back-light driving system for LCD panels," in *Proceedings of IEEE Applied Power Electronics Conference and Exposition (APEC)*, Mar. 2006, pp. 381–385.

[42] C. C. Chen, C. Y. Wu, Y. M. Chen, and T. F. Wu, "Sequential color LED backlight driving system for LCD panels," *IEEE Transactions on Power Electronics*, vol. 22, no. 3, pp. 919–925, May 2007.

[43] H. J. Chiu, Y. K. Lo, T. P. Lee, S. C. Mou, and H. M. Huang, "Design of an RGB LED backlight circuit for liquid crystal display panels," *IEEE Transactions on Industrial Electronics*, vol. 58, no. 7, pp. 2793–2795, Jul. 2009.

[44] K. Saucke, G. Pausch, J. Stein, H. G. Ortlepp, and P. Schotanus, "Stabilizing scintillation detector systems with pulsed LEDs: a method to derive the led temperature from pulse height spectra," *IEEE Transactions on Nuclear Science*, vol. 52, no. 6, pp. 3160–3165, Dec. 2005.

[45] A. E. Moe, N. Banani, L. A. Lee, B. Marquardt, and D. M. Wilson, "Enhanced fluorescence emission using a programmable, reconfigurable LED-array based light source," vol. 3, Sep. 2004, pp. 2090–2093.

[46] D. A. Steigerwald, J. C. Bhat, D. Collins, R. M. Fletcher, M. O. Holcomb, and M. J. Ludowise, "Illumination with solid state lighting technology," *IEEE Journal of Selected Topics in Quantum Electronics*, vol. 8, no. 2, pp. 310–320, Mar./Apr. 2002.

[47] E. F. Schubert and H. W. Yao, *Light-emitting diodes: research, manufacturing and applications*. SPIE-Int. Society for Optical Engine, 2006.

[48] S. Muthu, F. J. Schuurmans, and M. D. Pashley, "Red, green, and blue LEDs for white light illumination," *IEEE Journal of Selected Topics in Quantum Electronics*, vol. 8, no. 2, pp. 333–338, Mar./Apr. 2002.

[49] ——, "Red, green, and blue LED based white light generation: issues and control," in *Proceedings of IEEE Industry Application Society Conference (IAS)*, Oct. 2002, pp. 327–333.

[50] S. Muthu and J. Gaines, "Red, green, and blue LED based white light generation: implementation challenges and control design," in *Proceedings of IEEE Industry Application Society Conference (IAS)*, Oct. 2003, pp. 515–522.

[51] B. Ackermann, V. Schulz, C. Martiny, A. Hilgers, and X. Zhu, "Control of LEDs," in *Proceedings of IEEE Industry Application Society Conference (IAS)*, Oct. 2006, pp. 2608–2615.

[52] M. Dyble, N. Narendran, A. Bierman, and T. Klein, "Impacts of dimming white LEDs: Chromaticity shifts due to different dimming methods," *Proceedings of International Society for Optical Engineering (SPIE)*, pp. 280–288, Jul./Aug. 2005.

[53] G. Farkas, A. Poppe, J. Schanda, and K. Muray. (2004) Complex characterization of power LEDs: simultaneous measurement of photometric/radiometric and thermal properties. [Online]. Available: http://www.knt.vein.hu/staff/schandaj/SJCV-Publ-2005/503.pdf

[54] N. Narendran and Y. Gu, "Life of LED-based white light sources," *IEEE/OSA Journal of Display Technology*, vol. 1, no. 1, pp. 167–171, Sep. 2005.

[55] S. Winder, *Power Supplies for LED Driving*. Burlington, MA: Newnes, 2008.

[56] L. R. Nerone, "Design of a 2.5-Mhz, soft-switching, class-D converter for electrodeless lighting," *IEEE Transactions on Power Electronics*, vol. 12, no. 3, pp. 507–516, May 1997.

[57] B. Y. Shmuel, M. Shvartsas, and S. Glozman, "Statics and dynamics of fluorescent lamps operating at high frequency: modeling and simulation," *IEEE Transactions on Industry Applications*, vol. 38, no. 6, pp. 1486–1492, Nov/Dec. 2002.

[58] T. E. Jang, H. J. Kim, and H. Kim, "Dimming control characteristics of electrodeless fluorescent lamps," *IEEE Transactions on Industrial Electronics*, vol. 56, no. 1, pp. 93–100, Jan. 2009.

[59] J. H. Campbell, "Initial characteristics of high intensity discharge lamps on high frequency power," *Journal of Illumimating Engineering Society*, vol. 64, no. 12, pp. 713–722, Dec. 1969.

[60] R. Fiorello, "Powering a 35W DC metal halide HID lamp using the UCC3305 HID lamp controller," *Unitrode Application Note U-161*, 1999.

[61] ——, "Low-cost high power-density electronic ballast for automotive HID lamp," *IEEE Transactions on Power Electronics*, vol. 15, no. 2, pp. 361–368, Mar. 2000.

[62] W. S. Kim, B. H. Cho, and K. C. Lee, "Design and analysis of high-voltage transformer for HID lamp igniter," in *Proceedings of IEEE Applied Power Electronics Conference and Exposition (APEC)*, vol. 2, Mar. 2005, pp. 1043–1047.

[63] H. J. Chiu, T. H. Song, S. J. Cheng, C. H. Li, and Y. K. Lo, "Design and implementation of a single-stage high-frequency HID lamp electronic ballast," *IEEE Transactions on Industrial Electronics*, vol. 55, no. 2, pp. 674–683, Feb. 2008.

[64] G. Sauerländer, D. Hente, H. Radermacher, E. Waffenschmidt, and J. Jacobs, "Driver electronics for LEDs," in *Proceedings of IEEE Industry Application Society Conference (IAS)*, vol. 5, Oct. 2006, pp. 2621–2626.

[65] R. Mueller-Mach, G. O. Mueller, M. R. Krames, and T. Trottier, "High-power phosphor-converted light-emitting diodes based on III-nitrides," *IEEE Journal of Selected Topics in Quantum Electronics*, vol. 8, no. 2, pp. 339–345, Mar./Apr. 2002.

[66] G. Wyszecki and W. S. Stiles, *Color Science*. New York, NY: Wiley, 1982.

[67] D. L. MacAdam, *Color Measurements: Theme and Variations*. New York, NY: Springer-Verlag, 1985.

[68] S. Nakamura, T. Mukai, and M. Senoh, "Candela-class high-brightness GaInN/AlGaN double-heterostructure blue-light-emitting diodes," *Applied Physics Letters*, vol. 64, no. 13, pp. 1687–1689, Mar. 1994.

[69] G. B. Stringfellow and M. G. Craford, *High Brightness Light Emitting Diodes*. San Diego, CA: Academic Press, 1997.

[70] T. Tamura, T. Setomoto, and T. Taguchi, "Illumination characteristics of lighting array using 10 candela-class white LED under AC 100V operation," *Journal of Luminescence*, vol. 87-89, pp. 1180–1182, Apr. 2000.

[71] E. Hong, "A non-contact method to determine junction temperature of hihg-brightness(AlGaInP) light emitting diodes," Master thesis, Rensselaer Polytechnic Institute, Troy, NY, 2003.

[72] W. S. Oh, D. Cho, K. M. Cho, G. W. Moon, B. Yang, and T. Jang, "A novel two-dimensional adaptive dimming technique of X-Y channel drivers for LED backlight system in LCD TVs," *IEEE/OSA Journal of Display Technology*, vol. 5, no. 1, pp. 20–26, Jan. 2009.

[73] X. Xu and X. Wu, "High dimming ratio LED driver with fast transient boost converter," in *Record of IEEE Power Electronics Specialists Conference (PESC)*, Jun. 2008, pp. 4192–4195.

[74] H. M. Huang, S. H. Twu, S. J. Cheng, and H. J. Chiu, "A single-stage SEPIC PFC converter for multiple lighting LED lamps," in *Proceedings of IEEE International Sympomium on Electronic Design, Test and Application*, Jan. 2008, pp. 15–19.

[75] M. Doshi and R. Zane, "Reconfigurable and fault tolerant digital phase shifted modulator for luminance control of LED light sources," in *Record of IEEE Power Electronics Specialists Conference (PESC)*, Jun. 2008, pp. 4185–4191.

[76] Y. Gu and N. Narendran, "A non-contact method for determining junction temperature of phosphor-converted white LEDs," in *Proceedings of International Society for Optical Engineering (SPIE)*, vol. 5187, Jan. 2004, pp. 107–114.

[77] N. Narendran, Y. Gu, and R. Hosseinzadeh, "Estimating junction temperature of high-flux white LEDs," in *Proceedings of International Society for Optical Engineering (SPIE)*, vol. 5366, Jan. 2004, pp. 158–160.

[78] P. Pinho, E. Tetri, and L. Halonen, "Synergies of controller-based LED drivers and quality solid-stage lighting," in *Proceeding of IEEE Research in Microelectronics and Electronics*, Jun. 2006, pp. 405–408.

[79] E. Mineiro Sá Jr., F. L. M. Antunes, and A. J. Perin, "Junction temperature estimation for high power light-emitting diodes," in *Proceedings of IEEE International Symposium on Industrial Electronics (ISIE)*, Jun. 2007, pp. 3030–3035.

[80] A. Perduijn, S. de Krijger, J. Claessens, and et al. (2003) Light output feedback solution for RGB LED backlight applications. [Online]. Available: http://www.philipslumileds.com/pdfs/LOPFeedback4backlight.PDF

[81] A. Žukauskas, R. Vaicekauskas, and F. I. et al, "Quadrichromatic white solid state lamp with digital feedback," in *Proceedings of International Society for Optical Engineering (SPIE)*, vol. 5187, Jan. 2004, pp. 185–198.

[82] I. E. Ashdown, "Neural networks for LED color control," in *Proceedings of International Society for Optical Engineering (SPIE)*, vol. 5187, Jan. 2004, pp. 215–226.

[83] P. Deurenberg, C. Hoelen, J. van Meurs, and J. Ansems, "Achieving color point stability in RGB multi-chip LED modules using various color control loops," in *Proceedings of International Society for Optical Engineering (SPIE)*, vol. 5941, Jul./Aug. 2005, pp. 63–74.

[84] K. Lim, J. C. Lee, G. Panotopoulos, and R. Helbing, "Illumination and color management in solid state lighting," in *Proceedings of IEEE Industry Application Society Conference (IAS)*, Oct. 2006, pp. 2616–2620.

[85] J. Garcia, M. A. Dalla-Costa, J. Cardesin, J. M. Alonso, and M. Rico-Secades, "Dimming of high-brightness LEDs by means of luminous flux thermal estimation," *IEEE Transactions on Power Electronics*, vol. 30, no. 2, pp. 1107–1114, Apr. 2009.

[86] EN 61000-3-2, "Electromagnetic compatibility (EMC) – Part 3-2: Limits–limits for harmonic current emissions (equipment input current $\leq$ 16 A per phase)," 2006.

[87] M. Rico-Secades, A. J. Calleja, J. Ribas, E. L. Corominas, J. M. Alonso, and J. Garcia, "Driver for high efficiency LED based on flyback stage with current mode control for emergency lighting system," in *Proceedings of IEEE Industry Application Society Conference (IAS)*, Oct. 2004, pp. 1655–1659.

[88] G. Spiazzi, S. Buso, and G. Meneghesso, "Analysis of a high-power-factor electronic ballast for high brightness light emitting diodes," in *Record of IEEE Power Electronics Specialists Conference (PESC)*, Jun. 2005, pp. 1494–1499.

[89] M. Rico-Secades, A. J. Calleja, J. Ribas, E. L. Corominas, J. M. Alonso, J. Cardesín, and J. Carcía-García, "Evaluation of a low-cost permanent emergency lighting system based on high-efficiency LEDs," *IEEE Transactions on Industry Applications*, vol. 41, no. 5, pp. 1386–1390, Sep./Oct. 2005.

[90] H.-J. Chiu and S.-J. Cheng, "LED backlight driving system for large-scale LCD panels," *IEEE Transactions on Power Electronics*, vol. 54, no. 5, pp. 2751–2760, Oct. 2007.

[91] G. Carraro, "Solving high-voltage off-line HB-LED constant current control-circuit issues," in *Proceedings of IEEE Applied Power Electronics Conference and Exposition (APEC)*, Feb. 2007, pp. 1316–1318.

[92] J. Sebastián, D. G. Lamar, M. Arias, M. Rodriguez, and M. M. Hernando, "A very simple control strategy for power factor correctors driving high-brightness light-emitting diodes," in *Proceedings of IEEE Applied Power Electronics Conference and Exposition (APEC)*, Feb. 2008, pp. 537–543.

[93] Y. Hu and M. M. Jovanović, "LED driver with self-adaptive drive voltage," *IEEE Transactions on Power Electronics*, vol. 23, no. 6, pp. 3116–3125, Nov. 2008.

[94] Z. Ye, F. Greenfield, and Z. Liang, "A topology study of single-phase offline AC/DC converters for high brightness white LED lighting with power factor pre-regulation and brightness dimmable," in *Proceedings of IEEE Conference on Industrial Electronics, Control and Instrumentations (IECON)*, Nov. 2008, pp. 1961–1967.

[95] ——, "Offline SEPIC converter to drive the high brightness white LED for lighting applications," in *Proceedings of IEEE Conference on Industrial Electronics, Control and Instrumentations (IECON)*, Nov. 2008, pp. 1994–2000.

[96] S. K. Maddula and J. C. Balda, "Lifetime of electrolytic capacitors in regenerative induction motor drives," in *Record of IEEE Power Electronics Specialists Conference (PESC)*, Jun. 2005, pp. 153–159.

[97] H. van der Broeckl, G. Sauerlander, and M. Wendt, "Power driver topologies and control schemes for LEDs," in *Proceedings of IEEE Applied Power Electronics Conference and Exposition (APEC)*, Feb. 2007, pp. 1319–1325.

[98] Y. Qin, S. H. Chung, D. Y. Lin, and S. Y. R. Hui, "Current source ballast for high power lighting emitting diodes without electrolytic capacitor," in *Proceedings of IEEE Conference on Industrial Electronics, Control and Instrumentations (IECON)*, Nov. 2008, pp. 1968–1973.

[99] L. Gu, X. Ruan, M. Xu, and K. Yao, "Means of eliminating electrolytic capacitor in AC/DC power supplies for LED lightings," *IEEE Transactions on Power Electronics*, vol. 24, no. 5, pp. 1399–1408, May 2009.

[100] H. Chung, S. Y. R. Hui, and W. H. Wang, "An isolated ZVS/ZCS flyback converter using the leakage inductance of the coupled inductor," *IEEE Transactions on Industrial Electronics*, vol. 45, no. 4, pp. 679–682, Aug. 1998.

[101] K. Gillessen and W. Schairer, *Light Emitting Diodes: An Introduction*. New Jersey, NJ: Prentice Hall, 1987.

[102] Department of Energy, U.S., "ENERGY STAR program requirements for solid state lighting luminaires," Dec. 2008.

[103] International Electrotechnical Commission (IEC). [Online]. Available: http://www.iec.ch/

[104] EN 60598-1, "luminaires – Part1: General requirements and tests," 2008.

[105] EN 62031, "LED modules for general lighting – safety specifications," 2008.

[106] EN 61347-2-13, "Lamp controlgear – Part 2-13: Particular requirements for d.c. or a.c. supplied electronic controlgear for LED modules," 2006.

[107] EN 55015, "Limits and methods of measurement of radio disturbance characteristics of electrical lighting and similar equipment," 2009.

[108] A. I. Pressman, *Switching power supply design*. New York, NY: McGraw Hill, 1998.

[109] R. W. Erickson and D. Maksimovic, *Fundamentals of power electronics*. Norwell, MA: Kluwer Academic Publishers, 2001.

[110] G. D. Youle, "Light source control system," U.S. Patent 7 067 993, Jun., 2006.

[111] L. De Oto and T. E. Clary, "LED brightness compensation system and methods," European Patent EP1 901 587A2, Mar., 2008.

[112] Linear Technology. (1995) Constant-voltage / constant-current battery charger. [Online]. Available: http://www.datasheetcatalog.com/datasheets_pdf/L/T/1/5/LT1510.shtml

[113] V. Misra, W. Gong, and D. Towsley, "Fluid-based analysis of a network of AQM routers supporting TCP flows with application to RED," *ACM SIGCOMM Computer Communication Review*, vol. 30, no. 4, pp. 151–160, Oct. 2000.

[114] Oceanoptic Inc. (2008, Nov.) LED brightness compensation system and methods. [Online]. Available: http://www.oceanoptics.com/

[115] O. García, J. A. Cobos, R. Prieto, P. Alou, and J. Cueda, "Single phase power factor correction: a survey," *IEEE Transactions on Power Electronics*, vol. 18, no. 3, pp. 749–755, May 2003.

[116] H. Wei, I. Batarseh, G. Zhu, and P. Kornetzky, "A single-switch AC-DC converter with power factor correction," *IEEE Transactions on Power Electronics*, vol. 15, no. 3, pp. 421–430, May 2000.

[117] Q. Zhao, M. Xu, F. C. Lee, and J. Qian, "Single-switch parallel power factor correction AC-DC converters with inherent load current feedback," *IEEE Transactions on Power Electronics*, vol. 19, no. 4, pp. 928–936, Jul. 2004.

[118] T. F. Wu, J. C. Hung, S. Y. Tseng, and Y. M. Chen, "A single-stage fast regulator with PFC based on an asymmetrical half-bridge topology," *IEEE Transactions on Industrial Electronics*, vol. 52, no. 1, pp. 139–150, Feb. 2005.

[119] D. Fu, F. C. Lee, Q. Yang, and F. Wang, "A novel high-power-density three-level LLC resonant converters with constant-power-factor-control for charging appilcations," *IEEE Transactions on Power Electronics*, vol. 23, no. 5, pp. 2411–2420, Sep. 2008.

[120] C. K. Tse, "Circuit theory of power factor correction in switching converters," *International Journal of Circuit Theory and Applications*, vol. 31, no. 2, pp. 157–198, Feb. 2003.

[121] S. Luo, W. Qiu, W. Wu, and I. Batarseh, "Flyboost power factor correction cell and a new family of single-stage AC/DC converters," *IEEE Transactions on Power Electronics*, vol. 20, no. 1, pp. 25–34, Jan. 2005.

[122] A. Lázaro, A. Barrado, M. Sanz, V. Salas, and E. Olías, "New power factor correction AC-DC converter with reduced storage capacitor voltage," *IEEE Transactions on Industrial Electronics*, vol. 54, no. 1, pp. 384–397, Feb. 2007.

[123] M. K. H. Cheung, M. H. L. Chow, and C. K. Tse, "Practical design and evaluation of a 1 kW PFC power supply based on reduced redundant

power processing principle," *IEEE Transactions on Industrial Electronics*, vol. 55, no. 2, pp. 665–673, Feb. 2008.

[124] Vishay BC components. (2008) Aluminum capacitors power standard miniature snap-in 056/057 psm-si. [Online]. Available: http://www.farnell.com/datasheets/415179.pdf

[125] D. D. C. Lu, H. H. C. Iu, and V. Pjevalica, "A single-stage AC/DC converter with high power factor, regulated bus voltage, and output voltage," *IEEE Transactions on Power Electronics*, vol. 23, no. 1, pp. 218–228, Jan. 2008.

[126] P. C. Todd, "UC3854 controlled power factor correction circuit design," *Unitrode application note U-134*, 1997.

[127] D. Fu, F. C. Lee, and M. Xu, "A novel driving scheme for synchronous rectifiers in LLC resonant converters," *IEEE Transactions on Power Electronics*, vol. 24, no. 5, pp. 1321–1329, May 2009.

[128] XR-E Series datasheet, "Cree Xlamp XR-E LED data sheet," *Cree Inc.*, 2009.

[129] J. Sun, M. Xu, Y. Ren, and F. C. Lee, "Light-load efficiency improvement for buck voltage regulators," *IEEE Transactions on Power Electronics*, vol. 24, no. 3, pp. 742–751, Mar. 2009.